

# INTERNATIONAL JOURNAL OF MODERN ENGINEERING

Spring/Summer 2016  
Volume 16, No. 2

The Leading Journal of Engineering, Applied Science and Technology

Industrial

Electronics

Biomedical

Civil

Aerospace

Computer

Electrical

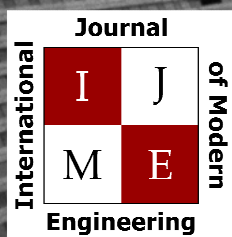
Chemical

Mechanical



# ENGINEERING





[www.ijme.us](http://www.ijme.us)

Print ISSN: 2157-8052  
Online ISSN: 1930-6628



[www.iajc.org](http://www.iajc.org)

## INTERNATIONAL JOURNAL OF MODERN ENGINEERING

### ABOUT IJME:

- IJME was established in 2000 and is the first and official flagship journal of the International Association of Journal and Conferences (IAJC).
- IJME is a high-quality, independent journal steered by a distinguished board of directors and supported by an international review board representing many well-known universities, colleges and corporations in the U.S. and abroad.
- IJME has an impact factor of **3.00**, placing it among the top 100 engineering journals worldwide, and is the #1 visited engineering journal website (according to the National Science Digital Library).

### OTHER IAJC JOURNALS:

- The International Journal of Engineering Research and Innovation (IJERI)  
For more information visit [www.ijeri.org](http://www.ijeri.org)
- The Technology Interface International Journal (TIIJ).  
For more information visit [www.tiij.org](http://www.tiij.org)

### IJME SUBMISSIONS:

- Manuscripts should be sent electronically to the manuscript editor, Dr. Philip Weinsier, at [philipw@bgsu.edu](mailto:philipw@bgsu.edu).

For submission guidelines visit  
[www.ijme.us/submissions](http://www.ijme.us/submissions)

### TO JOIN THE REVIEW BOARD:

- Contact the chair of the International Review Board, Dr. Philip Weinsier, at [philipw@bgsu.edu](mailto:philipw@bgsu.edu).

For more information visit  
[www.ijme.us/ijme\\_editorial.htm](http://www.ijme.us/ijme_editorial.htm)

### INDEXING ORGANIZATIONS:

- IJME is currently indexed by 22 agencies.  
For a complete listing, please visit us at [www.ijme.us](http://www.ijme.us).

### Contact us:

**Mark Rajai, Ph.D.**

Editor-in-Chief  
California State University-Northridge  
College of Engineering and Computer Science  
Room: JD 4510  
Northridge, CA 91330  
Office: (818) 677-5003  
Email: [mrajai@csun.edu](mailto:mrajai@csun.edu)



[www.tiij.org](http://www.tiij.org)



[www.ijeri.org](http://www.ijeri.org)

---

# INTERNATIONAL JOURNAL OF MODERN ENGINEERING

The INTERNATIONAL JOURNAL OF MODERN ENGINEERING (IJME) is an independent, not-for-profit publication, which aims to provide the engineering community with a resource and forum for scholarly expression and reflection.

IJME is published twice annually (fall and spring issues) and includes peer-reviewed articles, book and software reviews, editorials, and commentary that contribute to our understanding of the issues, problems, and research associated with engineering and related fields. The journal encourages the submission of manuscripts from private, public, and academic sectors. The views expressed are those of the authors and do not necessarily reflect the opinions of the IJME editors.

## EDITORIAL OFFICE:

Mark Rajai, Ph.D.  
Editor-in-Chief  
Office: (818) 677-2167  
Email: [ijmeeditor@iajc.org](mailto:ijmeeditor@iajc.org)  
Dept. of Manufacturing Systems  
Engineering & Management  
California State University-  
Northridge  
18111 Nordhoff Street  
Northridge, CA 91330-8332

## THE INTERNATIONAL JOURNAL OF MODERN ENGINEERING EDITORS

### *Editor-in-Chief:*

**Mark Rajai**  
California State University-Northridge

### *Associate Editors:*

**Alok Verma**  
Old Dominion University

**Li Tan**  
Purdue University North Central

### *Production Editor:*

**Philip Weinsier**  
Bowling Green State University-Firelands

### *Subscription Editor:*

**Morteza Sadat-Hossieny**  
Northern Kentucky University

### *Web Administrator:*

**Saeed Namyar**  
Advanced Information Systems

### *Executive Editor:*

**Paul Wilder**  
Vincennes University

### *Manuscript Editor:*

**Philip Weinsier**  
Bowling Green State University-Firelands

### *Copy Editor:*

**Li Tan**  
Purdue University North Central

### *Technical Editors:*

**Michelle Brodke**  
Bowling Green State University-Firelands

**Marilyn Dyrud**  
Oregon Institute of Technology

### *Publisher:*

**Bowling Green State University Firelands**

---

# TABLE OF CONTENTS

<i>Editor's Note: Special Conference Issue</i> .....	3
Philip Weinsier, IJME Manuscript Editor	
<i>Design and Comparison of Single Inverted Pendulum System Controllers</i> .....	5
Cheng Cheng, University of Tennessee; Yuqiu You, Ohio University	
<i>Short-Term Wind Speed Prediction Using Supervised Machine Learning Techniques</i> .....	13
Frank E. Yeboah, North Carolina A&T State University; Andrea N. Ofori-Boadu, North Carolina A&T State University; Peter A. Sam, U.S. Environmental Protection Agency; Musibau A. Shofoluwe, North Carolina A&T State University	
<i>A Software Tool to Predict the Risk of Hereditary Breast Cancer</i> .....	23
Rajeev Agrawal, North Carolina A&T State University; Sherin John, North Carolina A&T State University	
<i>Energy Efficiency Performance of Controllers on Air-Operated Double-Diaphragm Pumps</i> .....	36
David W. Goodman, Indiana University-Purdue University Indianapolis; Robert J. Durkin, Indiana University-Purdue University Indianapolis	
<i>A Study of Flash Atomization in a Pressure Swirl Nozzle</i> .....	44
Mebougna L. Drabo, Alabama A&M University; Narinder K. Tutu, Brookhaven National Laboratory; Thomas Butcher, Brookhaven National Laboratory; Rebecca Trojanowski, Brookhaven National Laboratory	
<i>Theoretical Prediction and Experimental Validation of Young's Modulus for Engineering Materials</i> .....	49
Yaomin Dong, Kettering University	
<i>Parameter Estimation in Ratio-Dependent Predator-Prey Ecological Systems with Bias Disturbance</i> .....	58
Dale B. McDonald, Midwestern State University	
<i>A Heuristic Strategy for the Control of Vibration Developed in Automatic Bar Feeders for Turning Operations Using Magnetorheological Fluid</i> .....	65
Kevin M. Hubbard, Missouri State University; Martin P. Jones, Missouri State University; Richard N. Callahan, Missouri State University	
<i>Instructions for Authors: Manuscript Submission Guidelines and Requirements</i> .....	73



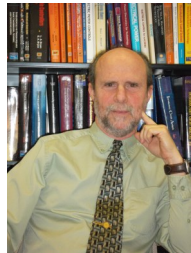


# 5th IAJC/ISAM Joint International Conference

November 6 – 8, 2016, Orlando, Florida



The leading indexed high impact factor conference on engineering and related technologies.



## EDITOR'S NOTE

Philip Weinsier, IJME Manuscript Editor

The editors and staff at IAJC would like to thank you, our readers, for your continued support, and we look forward to seeing you at the upcoming IAJC conference. For this fifth IAJC conference, we will again be partnering with the International Society of Agile Manufacturing (ISAM). This event will be held at the new Embassy Suites hotel in Orlando, FL, November 6-8, 2016. The IAJC/ISAM Executive Board is pleased to invite faculty, students, researchers, engineers, and practitioners to present their latest accomplishments and innovations in all areas of engineering, engineering technology, math, science, and related technologies.

In addition to our strong institutional sponsorship, we are excited this year to announce that nine (9) high impact factor (IF) ISI journals asked to sponsor our conference as well, and wish to publish some of your best papers. But I would be remiss if I didn't take this opportunity to remind you of the excellent impact factors (Google Scholar method) for our own three journals. The International Journal of Modern Engineering (IJME) has a remarkable IF = 3.00. The International Journal of Engineering Research and Innovation (IJERI) has an IF = 1.58, which is noteworthy, as it is a relatively young journal, only in publication since 2009. And the Technology Interface International Journal (TIIJ) with an IF = 1.025. Any IF above 1.0 is considered high, based on the requirements of many top universities, and places the journals among an elite group.

Selected papers from the conference will be published in the three IAJC-owned journals and possibly the nine ISI journals. Oftentimes, these papers, along with manuscripts submitted at-large, are reviewed and published in less than half the time of other journals. Publishing guidelines are available at [www.iajc.org](http://www.iajc.org), where you can read any of our previously published journal issues, as well as obtain information on chapters, membership, and benefits.

THOMSON REUTERS

Google scholar

issuu

WorldCat

docstoc

YUDUfree

Scribd

ULRICHSWEB GLOBAL SERIALS DIRECTORY

i seek

PDFCAST.ORG Broadcast PDF Documents

EBSCO Research Databases

ResearchGate Scientific Network

refseek\*

Main Sponsors

CSUN

IEEE Advancing Technology for Humanity

AMERICAN SOCIETY FOR MANUFACTURING EDUCATION

LEANinstitute

Journal of Modern Engineering

International Journal of Engineering Research & Innovation

TIIJ

Suzhou Zhenhua Technical University

## Editorial Review Board Members

Mohammed Abdallah	State University of New York (NY)	Shiyoung Lee	Penn State University Berks (PA)
Nasser Alaraje	Michigan Tech (MI)	Soo-Yen Lee	Central Michigan University (MI)
Aly Mousaad Aly	Louisiana State University (LA)	Chao Li	Florida A&M University (FL)
Jahangir Ansari	Virginia State University (VA)	Jimmy Linn	Eastern Carolina University (NC)
Kevin Berisso	Ohio University (OH)	Dale Litwhiler	Penn State University (PA)
Salah Badjou	Wentworth Institute of Technology (MA)	Guoxiang Liu	University of North Dakota (ND)
Pankaj Bhambri	Guru Nanak Dev Engineering (INDIA)	Louis Liu	University of New Orleans (LA)
Water Buchanan	Texas A&M University (TX)	Mani Manivannan	ARUP Corporation
Jessica Buck Murphy	Cal Poly State University (MS)	G.H. Massiha	University of Louisiana (LA)
John Burningham	Clayton State University (GA)	Thomas McDonald	University of Southern Indiana (IN)
Shaobiao Cai	Penn State University (PA)	David Melton	Eastern Illinois University (IL)
Vigyan Chandra	Eastern Kentucky University (KY)	Shokoufeh Mirzaei	Cal State Poly Pomona (CA)
Isaac Chang	Cal Poly State University SLO (CA)	Bashir Morshed	University of Memphis (TN)
Bin Chen	Purdue University Calumet (IN)	Sam Mryyan	Excelsior College (NY)
Wei-Yin Chen	University of Mississippi (MS)	Wilson Naik	University of Hyderabad (INDIA)
Hans Chapman	Morehead State University (KY)	Arun Nambiar	California State University Fresno (CA)
Rigoberto Chinchilla	Eastern Illinois University (IL)	Ramesh Narang	Indiana University-Purdue University (IN)
Phil Cochrane	Indiana State University (IN)	Anand Nayyar	Institute Management and Tech (INDIA)
Michael Coffman	Southern Illinois University-Carbondale (IL)	Stephanie Nelson	Cal State LA (CA)
Emily Crawford	Southern Wesleyan University (SC)	Hamed Niroumand	Universiti Teknologi (MALAYSIA)
Brad Deken	Southeast Missouri State University (MO)	Aurenice Oliveira	Michigan Tech (MI)
Z.T. Deng	Alabama A&M University (AL)	Troy Ollison	University of Central Missouri (MO)
Sagar Deshpande	Ferris State University (MI)	Reynaldo Pablo	Indiana University-Purdue University (IN)
David Domermuth	Appalachian State University (NC)	Basile Panoutsopoulos	Community College of Rhode Island (RI)
Ryan Dupont	Utah State University (UT)	Shahera Patel	Sardar Patel University (INDIA)
Marilyn Dyrud	Oregon Institute of Technology (OR)	Jose Pena	Purdue University Calumet (IN)
Mehran Elahi	Elizabeth City State University (NC)	Karl Perusich	Purdue University (IN)
Ahmed Elsayy	Tennessee Technological University (TN)	Thongchai Phairoh	Virginia State University (VA)
Rasoul Esfahani	DeVry University (OH)	Huyu Qu	Honeywell Corporation
Dominick Fazarro	Sam Houston State University (TX)	John Rajadas	Arizona State University (AZ)
Rod Flanigan	University of Nebraska-Kearney (NE)	Desire Rasolomampionona	Warsaw University of Tech (POLAND)
Ignatius Fomunung	University of Tennessee Chattanooga (TN)	Mulchand Rathod	Wayne State University (MI)
Ahmed Gawad	Zagazig University EGYPT)	Mohammad Razani	New York City College of Tech (NY)
Daba Gedafa	University of North Dakota (ND)	Sangram Redkar	Arizona State University-Poly (AZ)
Ralph Gibbs	Eastern Kentucky University (KY)	Michael Reynolds	University of Arkansas Fort Smith (AR)
Mohsen Hamidi	Utah Valley University (UT)	Marla Rogers	Wireless Systems Engineer
Mamoon Hammad	Abu Dhabi University (UAE)	Dale Rowe	Brigham Young University (UT)
Youcef Himri	Safety Engineer in Sonelgaz (ALGERIA)	Anca Sala	Baker College (MI)
Xiaobing Hou	Central Connecticut State University (CT)	Mehdi Shabaninejad	Zagros Oil & Gas Company (IRAN)
Shelton Houston	University of Louisiana Lafayette (LA)	Ehsan Sheybani	Virginia State University (VA)
Barry Hoy	St. Leo University (VA)	Musibau Shofoluwe	North Carolina State University (NC)
Ying Huang	North Dakota State University (ND)	Siles Singh	St. Joseph University Tanzania (AFRICA)
Charles Hunt	Norfolk State University (VA)	Ahmad Sleiti	University of North Carolina Charlotte (NC)
Dave Hunter	Western Illinois University (IL)	Jiahui Song	Wentworth Institute of Technology (MA)
Christian Hyeng	North Carolina A&T University (NC)	Yuyang Song	Toyota Corporation
Pete Hylton	Indiana University Purdue (IN)	Carl Spezia	Southern Illinois University (IL)
Ghassan Ibrahim	Bloomsburg University (PA)	Michelle Surerus	Ohio University (OH)
John Irwin	Michigan Tech (MI)	Vassilios Tzouanas	University of Houston Downtown (TX)
Sudershan Jetley	Bowling Green State University (OH)	Jeff Ulmer	University of Central Missouri (MO)
Rex Kanu	Ball State University (IN)	Mihaela Vorvoreanu	Purdue University (IN)
Reza Karim	North Dakota State University (ND)	Phillip Waldrop	Georgia Southern University (GA)
Tolga Kaya	Central Michigan University (MI)	Abraham Walton	Purdue University (IN)
Satish Ketkar	Wayne State University (MI)	Liangmo Wang	Nanjing University of Science/Tech (CHINA)
Manish Kewalramani	Abu Dhabi University (UAE)	Jonathan Williams	Lake Erie College (OH)
Tae-Hoon Kim	Purdue University Calumet (IN)	Boonsap Witchayangkoon	Thammasat University (THAILAND)
Doug Koch	Southeast Missouri State University (MO)	Alex Wong	Digilent Inc.
Rick Kribs	Vincennes University (IN)	Shuju Wu	Central Connecticut State University (CT)
Sally Krijestorac	Daytona State College (FL)	Baijian Yang	Ball State University (IN)
Ognjen Kuljaca	Brodarski Institute (CROATIA)	Mijia Yang	North Dakota State University (ND)
Chakresh Kumar	Uttar Pradesh Tech University (INDIA)	Faruk Yildiz	Sam Houston State University (TX)
Zaki Kuruppallil	Ohio University (OH)	Yuqiu You	Morehead State University (KY)
Edward Land	Johns Hopkins Medical Institute	Jinwen Zhu	Missouri Western State University (MO)
Ronald Land	Penn State University (PA)		
Jane LeClair	Excelsior College (NY)		

# DESIGN AND COMPARISON OF SINGLE INVERTED PENDULUM SYSTEM CONTROLLERS

Cheng Cheng, University of Tennessee; Yuqiu You, Ohio University

## Abstract

In this paper, the authors present the design and comparison of two methods to control and balance an inverted pendulum system based on the classical control theory and the modern control theory, respectively. These two control methods share the same mathematical model essentially derived from Newton's laws of motion. A PID controller and a pole placement controller were designed and compared in this study. After these two controllers were calculated theoretically, simulations were run on MATLAB to verify the validity of the designed controllers. Once each parameter of the controllers passed the simulation test, a comparison of their performance was studied. Then, the PID controller was tested in a LabVIEW-based control system, since PID controllers are always the simplest and most popular control method used in manufacturing systems. Future studies will focus on testing the pole placement controller on a real system to evaluate its feasibility, reliability, and robustness.

## Introduction

Figure 1 shows that the inverted pendulum system is a classic problem in the theory of control systems. It is always used to demonstrate concepts in linear control such as the stabilization of unstable systems. Since the system is inherently nonlinear, it also has been useful in illustrating some of the ideas in nonlinear control. In this system, an inverted pendulum was attached to a cart equipped with a motor that drives it along a horizontal track. The task is to make sure that the pendulum does not fall and is kept straight by moving the cart left or right. The study of the inverted pendulum has significant meaning for research on such topics as biped robot's walking problem, rocket's flight attitude adjustment, aircraft's landing, the stability of offshore oil platforms, etc.

The inverted pendulum is also a classic problem in dynamics and control theory and is widely used as a benchmark for testing control algorithms. To design a stabilizing controller for a single inverted pendulum is a typical problem in control system design based on the state space approach. A stabilized pendulum is useful for showing the power of a control mechanism to laymen of the state space theory [1]. The inverted pendulum system is a typical unstable, higher-order, multivariable, strongly coupling non-

linear system. It has two main purposes: first, as an inherently unstable nonlinear system, the inverted pendulum control system is the ideal platform to teach control theory and do research. Many typical problems such as nonlinear systems, robustness, follow-up, etc. are included in the study of the inverted pendulum system. Secondly, due to the features of the inverted pendulum system, new control methods can be tested on the inverted pendulum to see if they are able to deal with the system which is nonlinear and unstable.

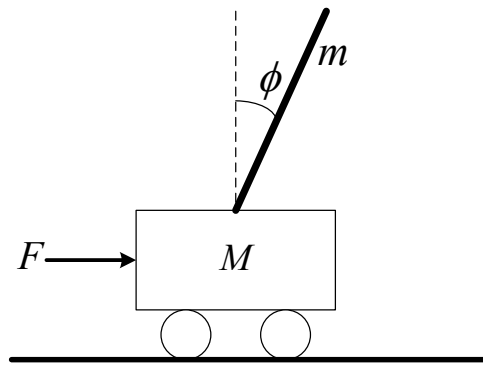


Figure 1. A Single Inverted Pendulum System

The design and comparison of a PID controller and a pole placement controller based on a single inverted pendulum system will provide supportive evidence for controller selection and implementation in real industry environment and reference for further studies in control systems.

## Review of Literature

Research on classic pendulum system controllers has been conducted and applied since as early as the 1970s. In a study by Mori et al. [2], the authors successfully controlled a single pendulum system considering the overall characteristics, including its nonlinear property which represented the real system more closely. In a study by Furuta et al. [1], the authors designed a controller using CAD to stabilize a double-inverted pendulum on an inclined rail. In 1984, Furuta et al. [3] realized the control of a triple-inverted pendulum system consisting of three arms. This pendulum was a good analogy of a human standing on a single leg without a foot; the results of that study contributed to the development of a biped locomotive machine. In 1992, Furuta et al. [4] proposed a robust swing-up control using a subspace projected from the whole state space. Based on the projected state



space or pseudo-state, the control input was determined depending on the partitioning of the state as a bang-bang type control. The control algorithm was applied in a new type of pendulum (TI Tech Pendulum), and the effectiveness and robustness of the proposed control were examined by additional experiments.

Now, most research involving the inverted pendulum is from Asian research institutions, such as Beijing Normal University, University of Science and Technology of China, Beijing University of Aeronautics and Astronautics (Beihang University) in China, Tokyo Institute of Technology, Tokyo Denki University, Tokyo University in Japan, and Pusan National University, Chungnam National University in Korea. Besides, St. Petersburg University in Russia, University of Eastern Florida in the U.S., the Russian Academy of Sciences, Poznan University in Poland, University of Florence in Italy and so on also have correlative research in this field. The experimental study of pendulum system controllers has contributed significantly to different fields of industry [5]. In this study, a PID controller and a pole placement controller were designed and compared on a single pendulum system. The result of this study can be used to determine the use of these controllers in manufacturing control systems.

## Methodology

### Mathematical Modeling

A descriptive model of the system was built to show that the system would work. This could help to estimate how an unforeseeable event could affect the system. Here, Newton's laws of motion were used to derive the mathematical model so that it could be more convenient to analyze and study the system's controllability and observability. As mentioned previously, the inverted pendulum system is a typical unstable, higher-order, multivariable, strongly coupling non-linear system. So, in order to simplify the mathematical model, some assumptions were made: 1) all components in the system are rigid; 2) the air resistance and the friction are neglected; and, 3) the entire mass of the pendulum is concentrated at the center of the mass [6]. Figure 2 and Table 1 show and list the model of a single inverted pendulum and its physical parameters and values, respectively.

The kinetic equations of the inverted pendulum system can be derived from Equations (1) and (2):

$$\ddot{\phi} = \frac{(M+m)mglsin\phi - mlF - m^2l^2\dot{\phi}sin\phi}{J(M+m) + m^2l^2(1 - cos\phi) + Mml^2} \quad (1)$$

$$\ddot{x} = \frac{(J + ml^2)F + (J + ml^2)ml\dot{\phi}sin\phi - m^2l^2g sin\phi cos\phi}{J(M+m) + m^2l^2(1 - cos\phi) + Mml^2} \quad (2)$$

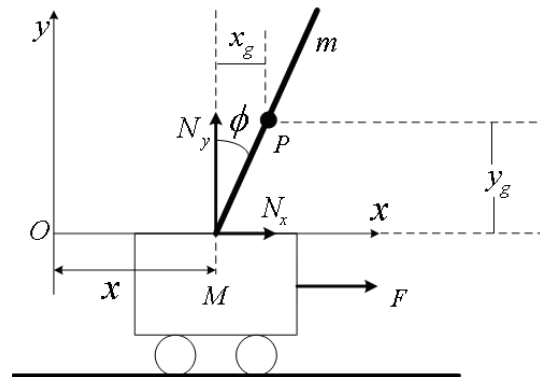


**Figure 2. The Mechanical Analysis of the Inverted Pendulum System**

**Table 1. Values and Parameters of the Inverted Pendulum System**

$m$ (kg)	Pendulum's mass	0.18
$M$ (kg)	Cart's mass	0.94
$l$ (m)	Pendulum's half length	0.30
$J$ (kg·m <sup>2</sup> )	Pendulum's moment of inertia	0.0054
$F$ (N)	Force on the cart	
$x$ (m)	Cart's position	
$\Phi$ (rad)	Pendulum's angle	

Since  $\phi$  is usually quite small while the inverted pendulum is working, the equations can be further simplified. And after substituting the variables with values from Table 1, the results are shown in Equations (3) and (4):

$$\ddot{\phi} = 27.86\phi - 2.538F \quad (3)$$

$$\ddot{x} = -1.34\phi + 1.015F \quad (4)$$

Taking the Laplace transforms of the above equations, the transfer functions could be derived as in Equations (5) and (6):

$$\frac{\Phi(s)}{U(s)} = \frac{-2.538}{s^2 - 27.86} \quad (5)$$

$$\frac{X(s)}{\Phi(s)} = \frac{9.800 - 0.400s^2}{s^2} \quad (6)$$

## System Stability

Generally speaking, most systems are unstable in open loop but stable in closed-loop configurations. In contrast, it is also possible that the system is stable in open loop but unstable in closed loop, even if this case is quite rare. Figure 3 shows the pole zero map of the open-loop system, which shows that one of the poles of the transfer function lies on the right-half side, or RHP, of the s-plane, meaning that the system is unstable. For the closed-loop situation, the root locus of the system in Figure 4 indicates that the closed-loop system is not stable, either due to the value of the loop gain or because one branch of the locus remains on the RHP of the s plane. This reveals that this system can never be controllable by unity feedback [7]. Equations (7) and (8) are shown below the figures.

$$\frac{\Phi(s)}{U(s)} = \frac{-2.538}{s^2 - 27.86} \quad \frac{X(s)}{\Phi(s)} = \frac{9.800 - 0.400s^2}{s^2} \quad (7)$$

$$\frac{\Phi(s)}{U(s)} = \frac{-2.538}{s^2 - 27.86} \quad \frac{X(s)}{\Phi(s)} = \frac{9.800 - 0.400s^2}{s^2} \quad (8)$$

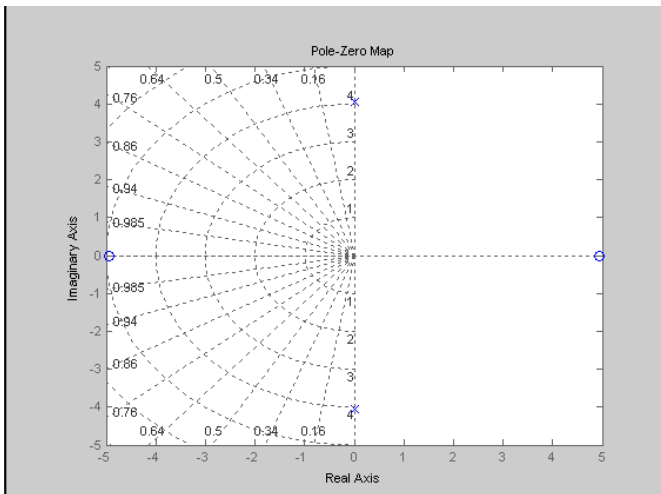
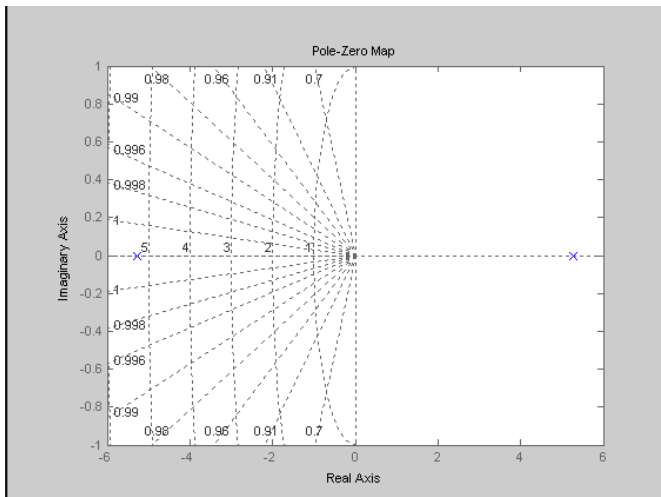


Figure 3. The Pole Zero Maps of the Open-Loop System

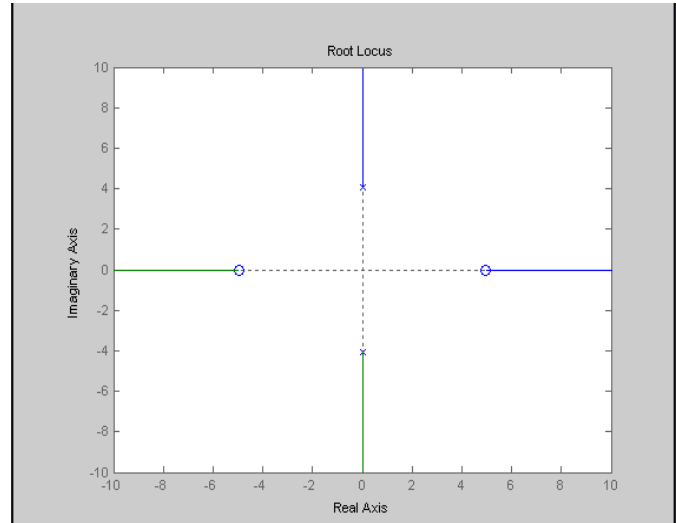
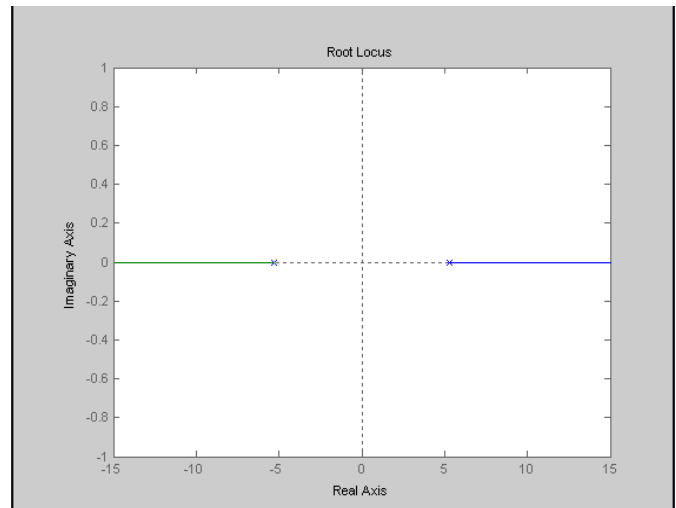
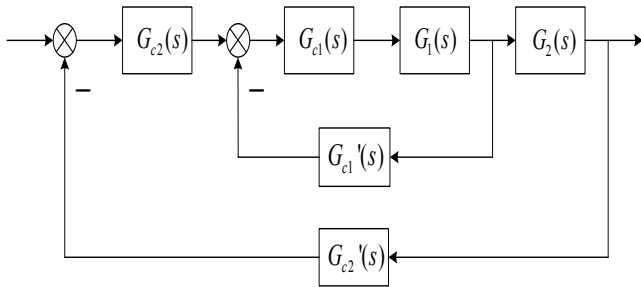


Figure 4. The Root Locus of the Closed-Loop System

The step response of the systems also confirmed what was mentioned above. So, in summary, the uncompensated systems, whether open-loop or closed-loop, are unstable [8].

## Control Strategy: PID Control

For the PID controller, a double-closed-loop control system was designed and implemented. There are two variables that need to be controlled: angle of the pendulum and position of the cart. Figure 5 shows the block diagram, in which  $G_1(s)$ , the angle, is the transfer function of the inner loop, while  $G_2(s)$ , the position, is the outer loop.



**Figure 5. Block Diagram of Double Closed-Loop Control**

Equation (9) shows the closed-loop transfer function:

$$\therefore W_1(s) = \frac{76.14}{s^2 + 76.14K_1s - 27.86 + 76.14K_2} \quad (9)$$

where,  $K = -30$ .

Equation (10) shows the standard second-order transfer function model:

$$W_1(s) = \frac{\omega_n^2}{s^2 + 2\zeta\omega_n s + \omega_n^2} \quad (10)$$

where,  $\zeta = 0.707$ ,  $\omega_n = 8.726$ , Equation (11) demonstrates the results:

$$\therefore W_1(s) = \frac{76.14}{s^2 + 12.34s + 76.14} \quad (11)$$

Equations (12) and (13) show the compensated system was verified to see if it met expectations:

$$M_p = e^{-\frac{\pi\zeta}{\sqrt{1-\zeta^2}}} = e^{-\frac{0.707\pi}{\sqrt{1-0.707^2}}} = 4.33\% \leq 5\% \quad (12)$$

$$t_s = \frac{4}{\zeta\omega_n} = \frac{4}{0.707 \times 8.726} = 0.648s \leq 2s \quad (13)$$

The controller was deemed acceptable. By using a PID controller, the root locus can be relocated to the left side of the  $s$ -plane and also change the system to a standard type II system. Therefore, the open-loop transfer function of the entire double-loop feedback system is shown in Equation

(14). Figure 6 shows the root locus of  $G(s)$ . Apparently, all of the poles are in the left half of the plane, which means that the system is stable when the locus is on the left half plane.

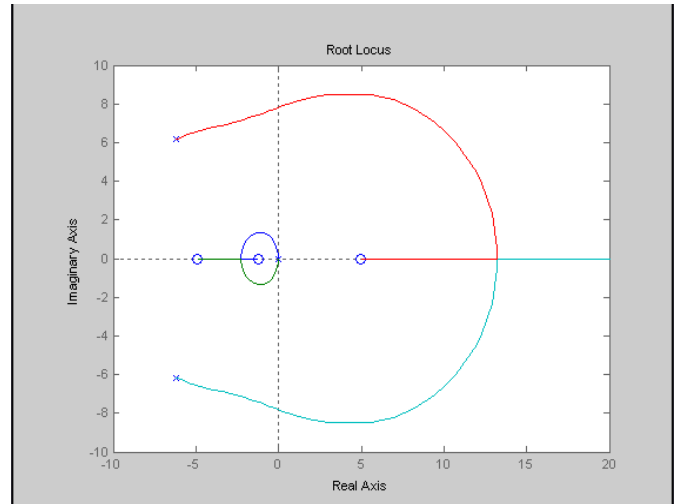


**Figure 6. The Root Locus of the Entire Closed-Loop System**

$$G(s) = G_{c2}(s)W(s)G_2(s) = \frac{-3.107s^3 - 3.837s^2 + 76.11s + 94.02}{s^4 + 12.34s^3 + 76.14s^2} \quad (14)$$

In order to see the step response of the closed-loop system, the simulation was done on Simulink in MATLAB [9]. The full diagram of the inverted pendulum system was created based on the block diagram. And the results show that the system will return to the stable state in about six seconds.

## Pole Placement

The expectations of the system are the same as the ones in PID control [10]:

- Take the optimum damping coefficient 0.707
- Overshoot  $M_p \leq 5\%$
- Settling time  $t_s \leq 2s$

Actually, Equation (15) shows that the damping coefficient is 0.707, such that the  $M_p$  will definitely be less than 5%:

$$M_p = e^{-\frac{\pi\zeta}{\sqrt{1-\zeta^2}}} = e^{-\frac{0.707\pi}{\sqrt{1-0.707^2}}} = 4.33\% \leq 5\% \quad (15)$$

Equation (16) shows the value of  $t_s$  is required to be less than two seconds:



$$t_s = -\frac{\ln(0.05\sqrt{1-\zeta^2})}{\zeta\omega_n} \leq 2 \quad (16)$$

As explained in the previous section, two variables, angle and position, were selected to control the system [11]. Equations (17) and (18) shows how the state space expression of the system can be written:

$$\begin{cases} \dot{x} = (A+BK) \times Bv \\ y = Cx + Dv \end{cases} \quad (17)$$

$$\begin{cases} \dot{x} = \begin{bmatrix} 0 & 1 & 0 & 0 \\ 23.59 & 18.59 & 88.73 & 16.80 \\ 0 & 0 & 0 & 1 \\ -58.98 & -46.50 & -197.36 & -42.00 \end{bmatrix} x + \begin{bmatrix} 0 \\ 1.015 \\ 0 \\ -2.538 \end{bmatrix} v \\ y = \begin{bmatrix} 1 & 0 & 0 & 0 \\ 0 & 0 & 1 & 0 \end{bmatrix} x + \begin{bmatrix} 0 \\ 0 \end{bmatrix} v \end{cases} \quad (18)$$

Figures 7 and 8 show the step response simulated by Simulink in MATLAB.

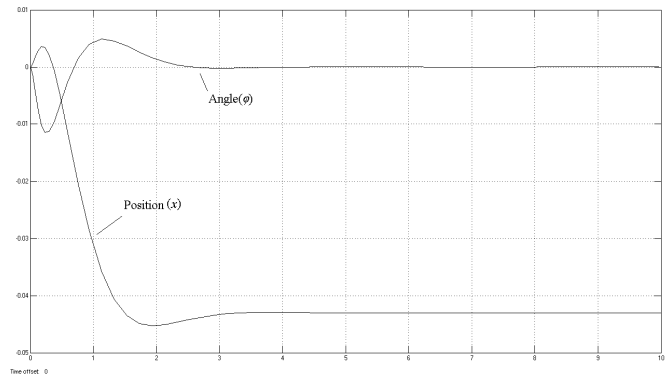


**Figure 8. Step Response of the System**

The results show that the system will return to the stable state in about 3.5 seconds.

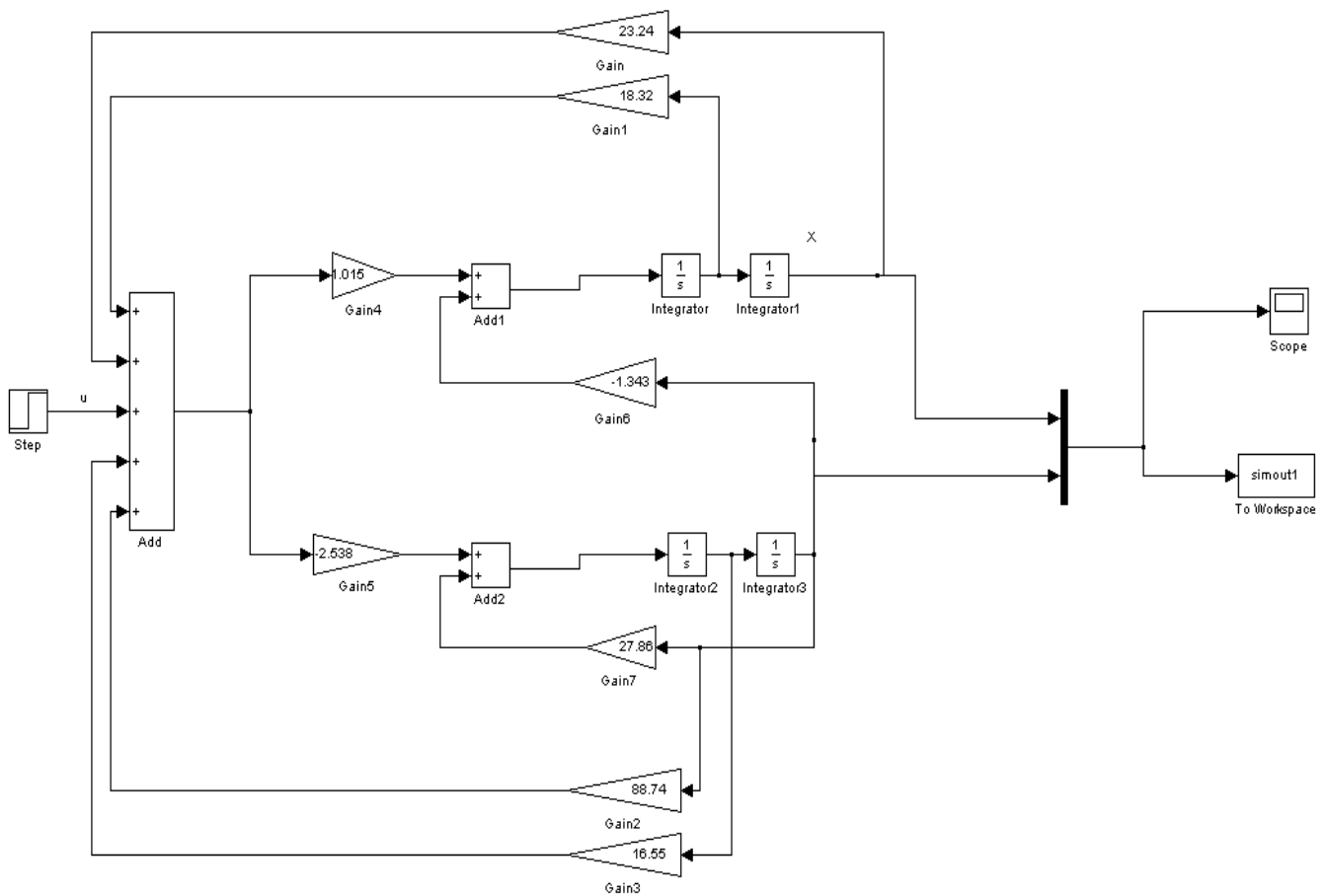


**Figure 7. Simulation Diagram of the Single Inverted Pendulum System**

## Implementation of the PID Controller

A LabVIEW-based control system was developed to implement the controller on a single inverted pendulum. Due to the limitations of the lab equipment, only one closed-loop feedback was implemented in the single inverted pendulum system. The controller will adjust the speed of the motor that drives the cart according to the changes of the pendulum angle. Figures 9 and 10 show the schematic and wiring diagrams, respectively.

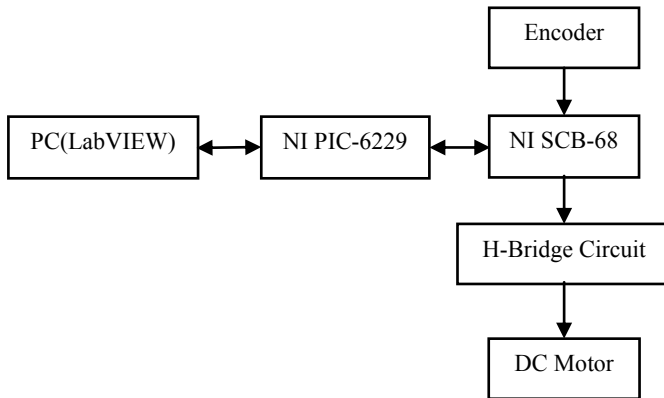


**Figure 9. Schematic Diagram of the System**

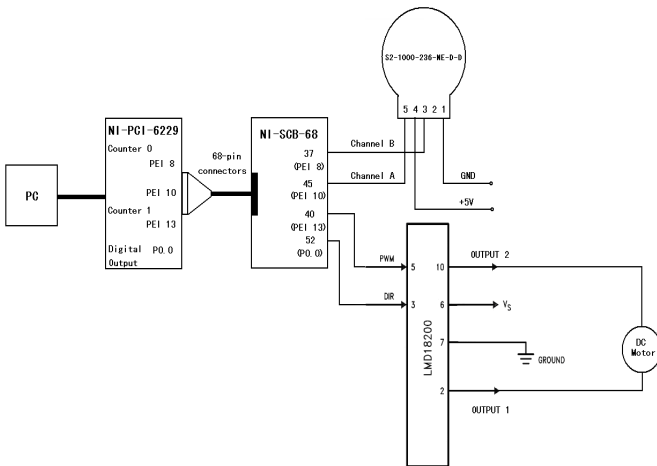


**Figure 10. Wiring Diagram for the Single Stage Inverted Pendulum System**

The controller receives signals from the encoder and sends out the pulse width modulation (PWM) signal to control the speed of the motor. The National Instruments PCI-6229 is a multifunction M Series data acquisition (DAQ) board. This board has two counters—one to read the pulse signal from the encoder and interpret the two-phase pulse trains to angle value, and the other to generate the PWM signal.

## Findings and Conclusions

### Testing

When tested in the LabVIEW environment, the real-time curve in Figure 11 shows that the angle could be sensed precisely, yielding an acceptable response time.

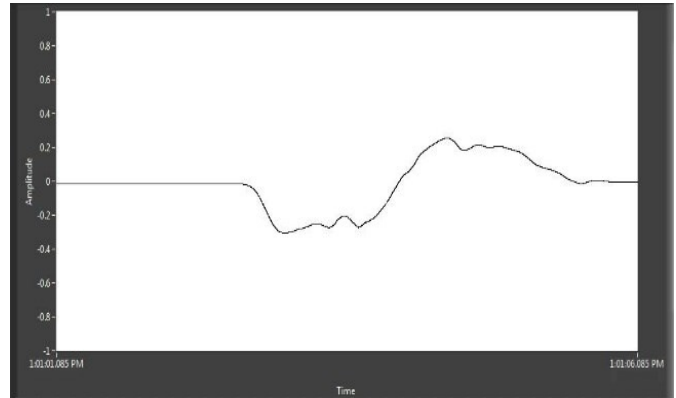


**Figure 11. Test of the Encoder**

Also the change of duty cycle on the front panel can be detected through the change of the PWM signal. The PWM signal shown on the oscilloscope indicated that the PWM signal was well adjusted by the assigned duty cycle, as shown in Figure 12.

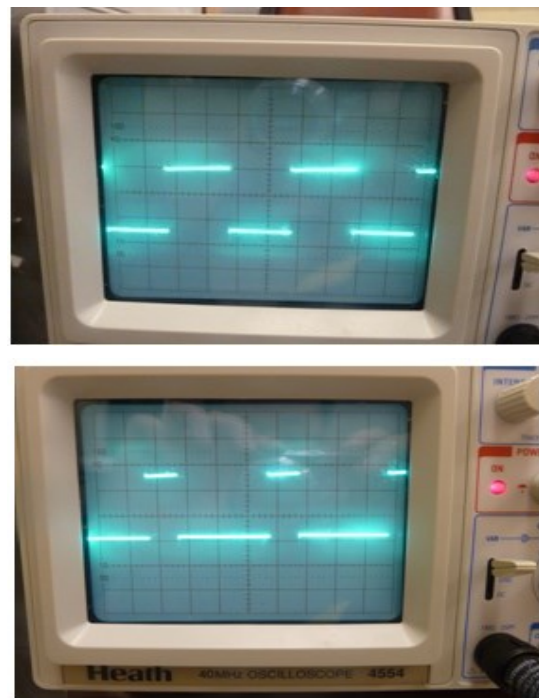


**Figure 12. PWM Signal with Duty Cycles of 0.61 and 0.23**

At the same time, the speed of the motor will change accordingly with the duty cycle. When the direction was set to 1, the motor would rotate clockwise; for 0, the motor would rotate counter-clockwise. Figure 13 shows how the speed of the motor can be easily modified in the LabVIEW environment, according to the sensed encoder angle.

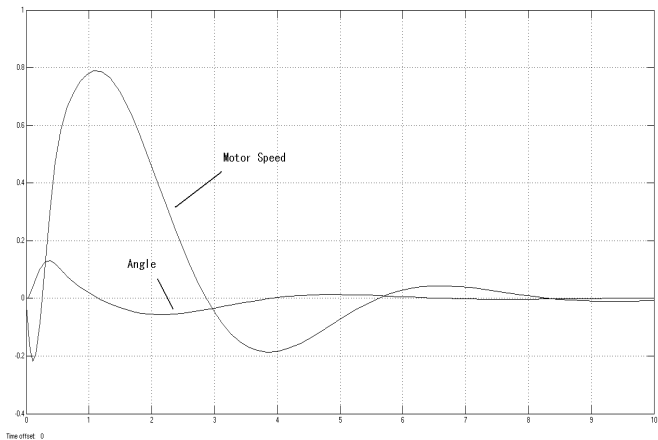


**Figure 13. Test of the Motor Controlling by Setting the Duty Cycle**

When the angle became negative, the direction of the motor changed immediately. Also, the more offset on the angle, the higher speed the motor would get. In Figure 13, a simulated sinusoidal signal was added on the angle input to observe the system's response. In order to let the inverted pendulum become balanced, proper PID parameters were assigned. The values of the PID parameters were obtained by PID tuning. Figure 14 shows that the pendulum returned to the upright position after a disturbance occurred. This basically demonstrated the self-balance of the system.

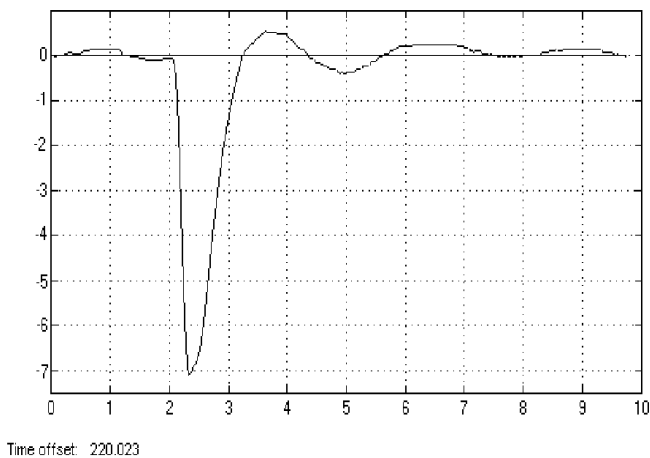


**Figure 14. Motor Speed Varies from the Angular Position**

## Advantages and Disadvantages

Due to the time and condition limit, one of the control methods cannot be tested on the real inverted pendulum system. However, from the simulation, it is apparent that both methods have advantages and disadvantages. For the PID control, the principle and algorithm of the control method are quite straightforward. Each part of the controller has different functions and, as long as they can coordinate perfectly, the system will become stable. The parameters could be adjusted while the system is working and the performance of the response is fast and clear. This is a classic and traditional control method that has been widely used in the manufacturing industry. However, the calculation of each parameter of the controller is very complicated. This requires the designer to be very familiar with not only classical control theory but also physics and mathematics. If any of the parameters like  $\omega_c$ ,  $\zeta$ , or  $K$  are not chosen properly, almost all the work will need to be redone. Usually it is time consuming to finally find suitable and proper parameters for the system.

For the pole placement, the calculation is not a problem anymore. The calculation of the PID control method is sometimes skillful, but the full-state feedback makes the calculation much easier to understand. Full-state feedback needs the system to be written in a different way which, to most people, is a bit awkward and difficult to understand. However, once the theory and how the full-state feedback can revise an unstable system are fully understood, it is not a problem to design the controller at all. In a word, this method tries to find a feedback matrix,  $K$ , to modify the state matrix,  $A$ , so that the new system can be stable. Nevertheless, not all of the state variables are easy to measure. Some of them even have no way to be measured. That makes this control method not available for practical use directly. But, with the introducing of state observer, this shortcoming can be overcome. This is one of its biggest disadvantages.

## Conclusions

Two control methods were implemented and used to design the controller of a single-inverted pendulum system. The simulation results indicated that the design had reached the expected targets and the two different control methods were compared, which were the two main goals of the study. Future work can focus on testing the designed controller by pole placement method on a real inverted pendulum system to study its performance in a practical way.



---

## References

- [1] Furuta, K., Kajiwara, H., & Kosuge, K. (1980). Digital control of a double inverted pendulum on an inclined rail. *International Journal of Control*, 32(5), 907-924.
- [2] Mori, S., Nishihara, H., & Furuta, K. (1976). Control of unstable mechanical system control of pendulum. *International Journal of Control*, 23(5), 637-692.
- [3] Furuta, K., Ochiai, T., & Ono, N. (1984). Attitude control of a triple inverted pendulum. *International Journal of Control*, 39(6), 1351-1365.
- [4] Furuta, K., Yamakita, M., & Kobayashi, S. (1992). Swing-up control of inverted pendulum using pseudo-state feedback. *Journal of Systems and Control Engineering*, 206(4), 263-269.
- [5] Liu, B., & Tang, W. (2008). *Modern control theory*. Beijing: China Machine Press.
- [6] Lu, Z., Lin, J., & Zhou, Y. (2009). *Automatic control theory*. Beijing: China Machine Press.
- [7] Sherer, E., & Hashimoto, K. (2003). Inverted pendulum balancer. Retrieved from <http://instruct1.cit.cornell.edu>
- [8] VTHokie. (2010, October 19). Counter output pwm with dynamic duty cycle updates in daqmx. Retrieved from <http://decibel.ni.com/content/docs/DOC-1379>.
- [9] Lindfield, G., & Penny, J. (1991). Numerical methods using matlab. (2<sup>nd</sup> ed). NJ: Prentice Hall.
- [10] Kurdekar, V., & Borkar, S. (2013). Inverted pendulum control: a brief overview. *International Journal of Modern Engineering Research*. 3(5).
- [11] Zare, A., & Lotfi, T. (2012). Robust control of inverted pendulum using fuzzy sliding mode control and particle swarm optimization algorithm. *International Journal of Scientific & Engineering Research*, 3(10).

turing, automation control, and remote control systems. Dr. You may be reached at [youy@ohio.edu](mailto:youy@ohio.edu)

## Biographies

**CHENG CHENG** is a PhD candidate in the Department of Electronic Engineering at the University of Tennessee. He earned his B.E. from Guangxi University in China and MS from Morehead State University. His research interests include automation control, power systems, and controller designs. Mr. Cheng may be reached at [ccheng8@utk.edu](mailto:ccheng8@utk.edu)

**YUQIU YOU** is an associate professor of engineering technology and management at Ohio University. She earned her BE degree from HuaZhong University of Science and Technology in China, M.S. from Morehead State University, and PhD (Technology Management, 2006) from Indiana State University. Dr. You is currently teaching at Ohio University. Her interests include computer-integrated manufac-

# SHORT-TERM WIND SPEED PREDICTION USING SUPERVISED MACHINE LEARNING TECHNIQUES

Frank E. Yeboah, North Carolina A&T State University; Andrea N. Ofori-Boadu, North Carolina A&T State University; Peter A. Sam, U.S. Environmental Protection Agency; Musibau A. Shofoluwe, North Carolina A&T State University

## Abstract

Renewable energy portfolios have become part of the requirements that utilities in certain states must conform to. It is therefore imperative that the availability and quantity of renewable energy resources—mostly solar and wind—are predicted ahead of time. Wind energy is highly variable and a non-stationary source of power. Also, the relationship between wind speed and wind power are nonlinear, making accurate predictions of wind speed an essential requirement for improving the predictions of wind power, especially in a day-ahead energy market. Numerical weather prediction (NWP) has been employed in forecasting wind speed in the short term. NWP forecasting, without any modeling adjustments, produces deterministic, or point, estimates and, therefore, may not be appropriate for dealing with stochastic problems such as wind prediction whose acquisition can also be prohibitive. In this study, the authors explored the use of machine learning techniques to predict wind speed one day-ahead. Emphasis was placed on decision trees ensembles, neural networks, and support vector machines (SVM). The ensemble method and SVM yield better predictions than the neural networks.

## Introduction

The use of renewable energy has become a tool for mitigating global climate change. Renewable energy technologies such as wind and solar are sometimes very difficult to integrate into electrical energy generation systems, given the fact that supply has to match demand to maintain the stability of the power grid. One of the main challenges of renewable energy technologies stems from the fact that their power generation depends on environmental factors such as wind speed and solar radiation, among others. This makes it difficult to plan and control their quantity ahead of time. Wind power, for instance, is highly variable and non-stationary in nature. Being able to accurately predict wind speed is *sine qua non* for the accurate prediction of wind energy, as wind speed is a significant contributor to wind power and is also non-linearly related as a cubic function. Any small deviation from actual wind speed could, therefore, amplify fluctuations in generation capacity, which could ultimately affect the integrity of the power grid, especially in a day-ahead energy market.

Wind resource forecasting for the short-term could be done using NWP/physical or statistical methods [1-3]. Unfortunately, the NWP model provides deterministic or point estimates, thereby limiting its usefulness to deterministic rather than stochastic problems, though ensemble methods may be developed to circumvent this shortcoming [4]. On the other hand, traditional statistical forecasting techniques such as regression, autoregressive integrated moving average (ARIMA), and other time-series models have their limitations when used for predicting renewable energy resources. These techniques [5] are referred to as data models. Where complex systems are involved and there is an abundance of data, machine learning (ML) techniques are more suitable for prediction [6, 7]. These techniques may be grouped into supervised and unsupervised techniques [6]. Supervised machine learning (SML) techniques are used in predictive modeling, whereas the unsupervised techniques, such as clustering techniques, are used for information or knowledge discovery. The focus of this study was on SML techniques. Several methods are available for solving SML problems including neural networks, support vector machines, and ensemble methods (e.g., random forest, bagging, and boosting techniques).

Perera et al. [8] reviewed different types of ML techniques used for predicting renewable energy. Artificial neural networks (ANN) have been used in modeling renewable energy resources such as solar and wind [9-13]. A comparison of different forecasting methods for predicting wind speed has also been conducted [14, 15]. Artificial intelligence methods, including ANN, support vector machines (SVMs), and nearest neighbor search (NNS) have been used to predict day-ahead and hourly wind power for single wind farms [14]. The gradient descent with the backpropagation algorithm was used in training the ANN model. The variable selection in the NNS model was carried out using particle swarm optimization. Individual models were also used to create an ensemble model for prediction. The ensemble model was found to perform better than any of the individual models. The use of the random forest ensemble technique in predicting solar radiation for renewable energy applications was also carried-out [16]. A comparison made with the feedforward neural model showed that the random forest model and its special case, the bagging technique, outperformed the feedforward neural network.

Sfetos [15] used hourly data over the course of one month to predict wind speed and noted that ML techniques performed better than their traditional statistical counterparts such as the ARIMA models. The model's one month of data, however, could not help account for seasonal variations in the model. A review of wind-speed and wind-power forecasting models has also been undertaken [17, 18]. Carpinone et al. [1] and Potter and Negnevitsky [19] presented very short-term wind-power forecasting techniques. In addition, Mendes et al. [3] reviewed several tools for forecasting very-short-term wind resources. Mohandes et al. [20] compared the use of SVMs and ANN was carried out by for predicting wind speed and reported that SVMs are better than ANN for predicting wind speed.

Artificial neural networks are often cited as appropriate modeling techniques for wind forecasting. In this current study, the authors showed that random forests and SVMs can perform better than neural network models in predicting short-term wind speed. This paper limits discussion to the random forest technique, an ensemble method, SVMs, and neural networks.

## Data Preparation and Modeling

The wind speed data for modeling came from 5-minute data samples taken over a one-year period (January 1 – December 31, 2014), which were acquired from a weather station in Greensboro, NC (Lat. 36.08° N, Lon. 79.82° W), installed by the authors. A total of 105,120 datasets of 5-minute samples were aggregated into 8760 hourly datasets for training and testing the model. The predictor (input) variables included weather data: average, minimum, and maximum temperature, dew point, and relative humidity (RH). In addition, seasonal variables (month of year; day of month; hour of day) were created from the timestamp of the data, to capture seasonality. The response (target/output) variable was the wind speed (in m/s) that was to be predicted. A separate set of data (Jan. 1 – 4, 2015) that was not used in the modeling, was used in predicting hourly and daily mean wind speed one to four days ahead. The instrument height of the wind anemometer was 10.54 ft. (3.21 m) above ground. The wind speed can be calculated for any required elevation, as given by Equation (1):

$$V_1 = \left[ \frac{H_1}{H_0} \right]^{\frac{1}{a}} \times V_0 \quad (1)$$

where,  $V_1$  is the wind speed at any given elevation  $H_1$ ;  $V_0$  is the wind speed at the elevation of the instrument height,  $H_0$ , and,  $a$  is the frictional coefficient based on terrain and other locational factors. Three main supervised machine learning (SML) techniques were used in this study: random forest, a

multilayer feedforward neural network (FFNN), and a regression support vector machine (SVM). The models may be represented as a multivariate forecast, as given in Equation (2)[3]:

$$\hat{Y}_{t+k|t} = f\left(Y_t, Y_{t-1}, \dots, \hat{X}_{t+k}, \dots, \hat{X}_{t+1}, X_t, X_{t-1}, \dots, X_{t-n}\right) + e_t \quad (2)$$

where,  $\hat{Y}_{t+k|t}$  is the variable to be predicted (wind speed in m/s) for time step  $t+k$ ;  $Y_t$  is the measured value of the response variable at current time  $t$ ;  $X_t, \dots, X_{t-n}$  is the set of measured (or past) exogenous variables (predictors such as temperature, relative humidity, month of year, etc.) and  $\hat{X}_{t+k}, \dots, \hat{X}_{t+1}$  is the corresponding prediction set;  $e_t$  is white noise; and,  $f$  is a generic function, either linear or nonlinear.

## Random Forest Model

A discussion of ensemble techniques by Yeboah et al. [16] focused on bagging, boosting, and random forest techniques and how these methods evolved from classification and regression trees. This current study used random forest. The random forest/bagged decision tree (BDT/RF) ensemble method was developed for predicting short-term wind speed. The steps involved in BDT/RF modeling include determining the optimal leaf size to grow on a tree, selecting the variables of importance, determining the optimal number of trees to grow in the forest, determining the prediction accuracy (as measured by the mean square error of the out-of-bag test samples), and using the model for prediction.

Yeboah [16] provided a description of using MATLAB Tool in developing ensemble modeling. The concept was extended to develop all the three models in this current study, namely, BDT/RF, FFNN, and SVM. Figure 1 depicts a plot of the number of leaves that can be grown on a tree in the forest and their corresponding mean square errors. It can be shown that the optimal leaf size is five, corresponding to the curve with the lowest out-of-bag (OOB) mean square error (MSE) of 0.2558. Figure 2 shows the variables of importance in the model. The importance of each predictor to the model is measured by its contribution to the accuracy of prediction, based on the training dataset [16]. While the DayOfMonth, HrOfDay, and MonthOfYear were much more important for modeling, as illustrated in the figure, the other remaining variables were also included as being important and therefore were kept in the model.

A BDT/RF model was developed with 1000 trees in the forest and five leaves per tree; the corresponding regression error, as measured by the OOB MSE, are plotted in Figure 3. This produced an OOB MSE of 0.2435 for the model if only 200 trees are grown in the forest. If 1000 trees were to

be grown in the forest, this would have yielded an OOB MSE of 0.2419, which is not significantly different from the MSE of a 200-tree forest. Therefore, beyond 200 trees, there were no improvements in the model's OOB MSE. Since more trees are equivalent to more computational time and space to store trees and other related model data, a 200-tree forest model was used in modeling the BDT/RF.

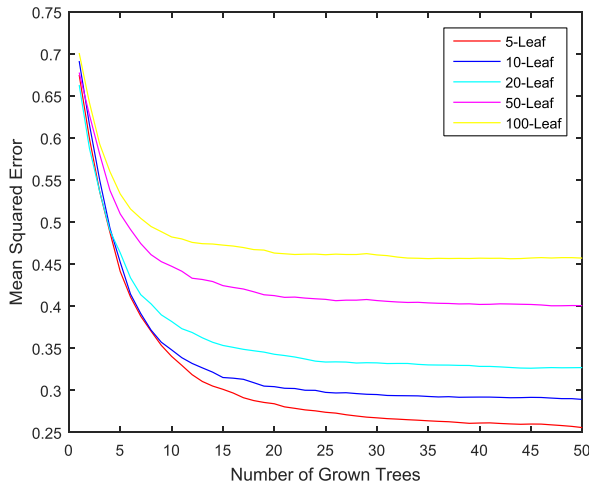


**Figure 1. Optimal Leaf Size**

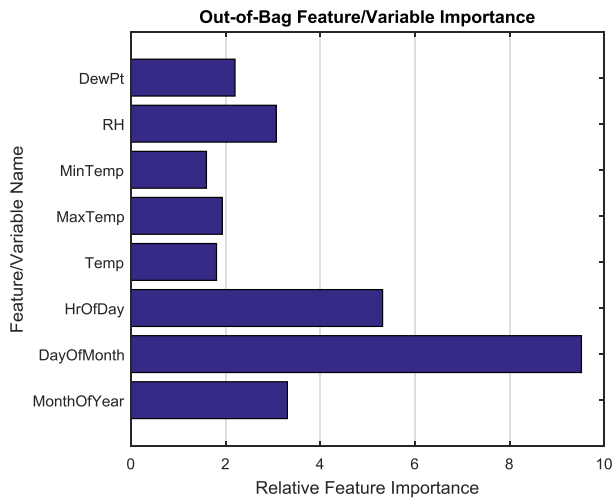


**Figure 2. Variable Selection/Importance**

## Neural Network Model

Neural networks have been touted as being one of the models suitable for nonlinear regression. There are three main types of neural networks: feedforward neural network (FFNN), radial basis function, and recurrent neural networks. In this study, an FFNN was developed as another

SML technique. Three main steps are typically used for modeling a multilayer FFNN [16]:

- Designing the network
- Training the network
- Testing the validity of the model

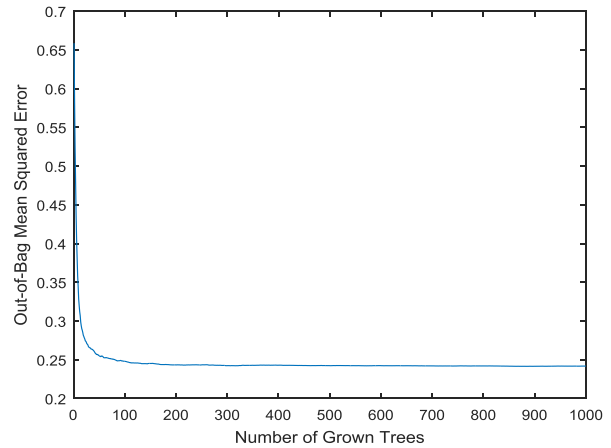


**Figure 3. Determining the Number of Trees to Grow**

Figure 4 illustrates the network architecture used in the FFNN modeling.

A multilayer FFNN involves one or more additional layers of hidden nodes placed between the input and the output layers, unconnected to both the input and output layers. Multilayer perceptrons allow nonlinearity to be incorporated into the model [21]. Designing a multilayer FFNN involves selecting or defining the number of layers and neurons to be used in each layer. In addition, transfer functions needed to convert the output from each input layer must also be defined.

These include the hyperbolic tangent sigmoid, logistic sigmoid, and linear functions [22, 23]. An optimization or training algorithm is needed to train the model during the backward iteration process, where the input parameters (biases and weights) of the feedforward process are revised to minimize the errors between the output of the feedforward process and the target value of the original output data, in this case the response variable. The optimization algorithms that may be used in FFNN include the Levenberg-Marquardt (LM), scaled conjugate gradient, and Bayesian regularization. Mean square error, root mean square error (RMSE), or mean absolute error (MAE) may be used as error functions that need to be minimized during the optimization process. They are defined mathematically, as given in Equations (3-5), respectively.



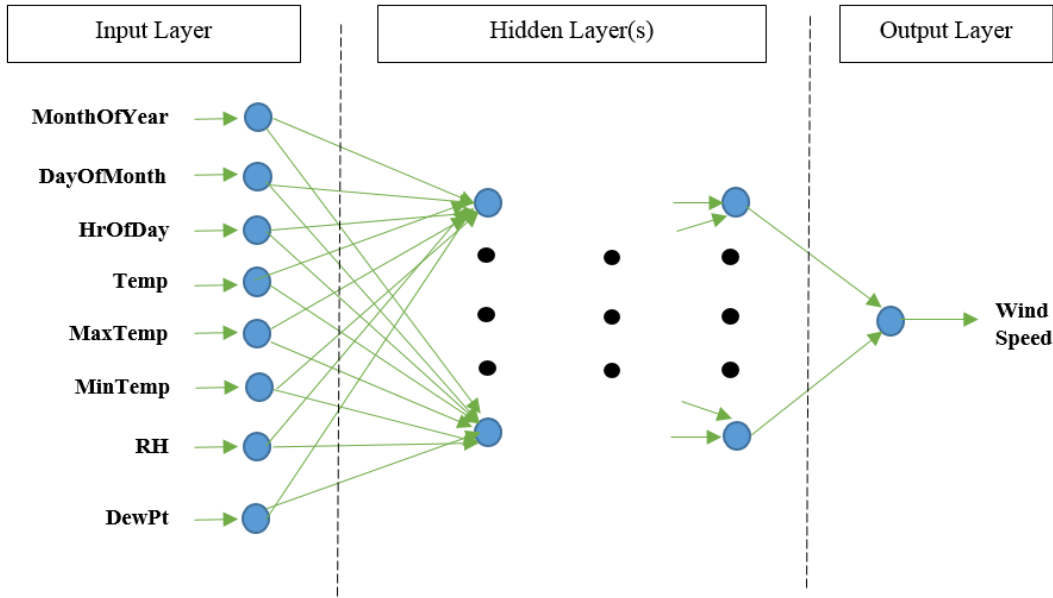


Figure 4. FFNN Model Architecture

$$MSE = \frac{1}{N} \sum_{t=1}^N (Y_t - \hat{Y}_t)^2 \quad (3)$$

$$RMSE = \left[ \frac{1}{N} \sum_{t=1}^N (Y_t - \hat{Y}_t)^2 \right]^{0.5} \quad (4)$$

$$MAE = \frac{1}{N} \sum_{t=1}^N |Y_t - \hat{Y}_t| \quad (5)$$

where,  $N$  is the forecasting horizon,  $Y_t$  is the average wind speed at time period  $t$  measured at the given geographical location, and  $\hat{Y}_t$  is the predicted wind speed from the model.

Once the architecture of the FFNN model has been designed, the model could be trained using the selected optimization algorithm (LM in this case), to optimize the selected error function and, hence, the weights and biases of the training data. The LM algorithm was selected because it is much more efficient [24]. The trained network was tested using a new set of data to determine a good balance between accuracy and generalization. The choice of the number of neurons to use in the hidden layers is an art rather than mathematics. When the number of neurons in the hidden layer is small, then the correlation of the output and input cannot be correctly studied, thereby resulting in increased error. On the other hand, an unnecessarily large number of neurons will lead to irrelevant noise to be added to the correlation, causing the error to grow [22, 25, 26]. In this study,

the trial-and-error approach was used to determine the optimal number of neurons, by increasing the number, training the model, and observing the corresponding mean square error.

Several network architectures were designed and tested. The resulting MSE and R-values of both training and testing of the models were recorded. The optimal architecture (i.e., model with the optimized error functions) is the one that used all of the input variables in the model. Based on this, FFNN architecture 8-50-50-50-1 was developed as the final model (see Figure 4), whose performance is shown in Figures 5 and 6.

## Regression SVM Model

Vapnik [27] developed the foundations of SVMs. Its attractiveness for predictive modeling stems from the fact that it is based on the principle of structural risk minimization (SRM), which is superior to empirical risk minimization (ERM), as employed in traditional neural networks [28]. As a consequence, SVM has a better generalization error than models based on ERM. Another attraction of SVM is that, unlike most data-driven techniques, such as NN, which has no functional forms, it has a functional form similar to model-driven traditional techniques like linear regression or ARIMA. While the exact nature of the functional form of model-driven techniques has to be assumed *a priori*, this assumption is not necessary in SVM. Also, like other data-

driven models, SVM can handle complex and nonlinear relationships [29]. A comparison of SVM and NN carried out by Liong and Sivapragasam [29] to forecast flood levels found that the SVM model outperformed the NN model. Originally developed to solve classification problems, the SVM technique has since been extended to solve regression problems, which is the emphasis of this paper.

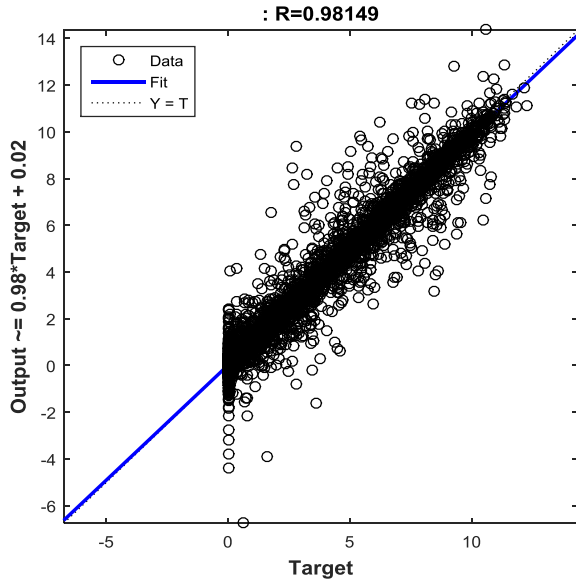


Figure 5. FFNN Model Validation—Goodness-of-Fit



Figure 6. FFNN Model Validation—Residual Analysis

When dealing with nonlinear functions, SVM maps the input data,  $\mathbf{x}$ , in input space, onto a high-dimensional feature space through a nonlinear mapping function,  $\phi$ . This allows a linear regression to be performed in the feature

space [27–31]. The final decision function for implementing nonlinear regression using SVM can then be given as in Equation (6):

$$f(x) = \sum_{i=1}^l (\alpha_i - \alpha_i^*) K(x_i, x) + b \quad (6)$$

where,  $K(x_i, x_2) = \langle \phi_i, \phi_j \rangle = \phi(x_i) * \phi(x_2)$  is a kernel function,  $\alpha_i, \alpha_i^*$  are Lagrange multipliers,  $b$  is a bias, and  $l$  is the number of training data.

Datasets corresponding to nonzero Lagrange multipliers are referred to as support vectors. The use of kernels allows the mapping of the input data into a feature space to be done implicitly and makes it possible for training a linear machine in such. This overcomes the otherwise computationally intensive evaluation of the feature space [27-29]. According to Vapnik [27], any function that satisfies Mercer’s condition can be used as a kernel function. Typical kernel functions include exponential radial basis function (RBF), Gaussian RBF, and polynomial kernels. The Gaussian RBF kernel was used in this study and is shown in Equation (7):

$$K(x_i, x_j) = \exp\left\{-\|x_i - x_j\|^2 / (2\sigma^2)\right\} \quad (7)$$

where,  $\sigma$  is a tunable parameter (width of RBF) of the Gaussian RBF kernel.

The steps involved in developing an SVM regression include

- Dividing the data into training and testing sets
- Training the model using the training set. During the training, part of the training data may be set aside for validation of the trained model
- Testing the trained model using a new set of test data
- Using the model for prediction

In this current study, 70% and 30% of the data, respectively, were training and testing data sets. Selecting an appropriate kernel function is a prerequisite for successfully training an SVM model. Kernel functions that may be used for nonlinear modeling [27, 28] include the Gaussian RBF, exponential RBF, and polynomial kernels. The optimization is done using the sequential minimization optimization (SMO) solver in MATLAB. This has been found to yield optimal results without compromising the time for training the model. Other solvers such as the iterative single data algorithm (ISDA) did not improve the results and also took longer to train. A pattern search global minimization algorithm using 10-fold cross-validation was used to train the model to obtain the optimal SVM parameters—Kernel scale and upper bound. In this study, several kernels were tested, and the corresponding model with the optimal MSE for training, testing, and prediction was selected.

The Gaussian RBF was selected because it has a minimum prediction error of 0.0522 for one-day-ahead wind speed prediction. While the polynomial kernel of order five produced the lowest training and testing errors, 0.0079 and 0.3197, respectively, its prediction accuracy for one day ahead of 0.1227 was not better than that of the Gaussian RBF (0.0522).

## Results and Discussion

This study compared three main supervised machine learning (algorithmic) models to predict short-term wind speed (i.e., 24-hr or one-day-ahead average wind speed, in  $\text{ms}^{-1}$ ). An ensemble model (BDT/RF), an FFNN model, and a regression SVM model were developed and used for the comparative analysis. Figures 7-9 depict the plots of the actual and the predicted hourly mean daily wind speeds for each of the three models.

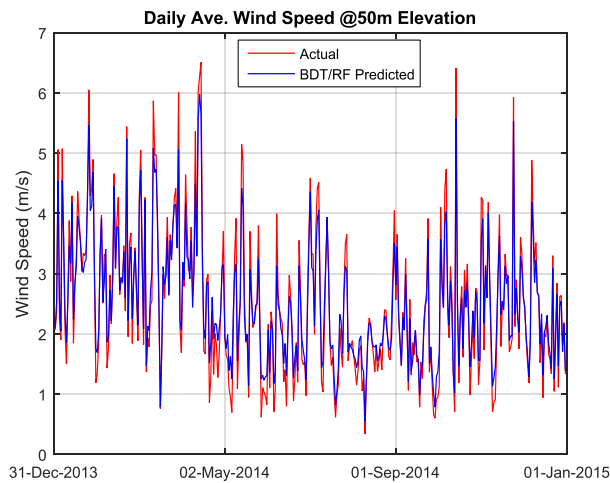


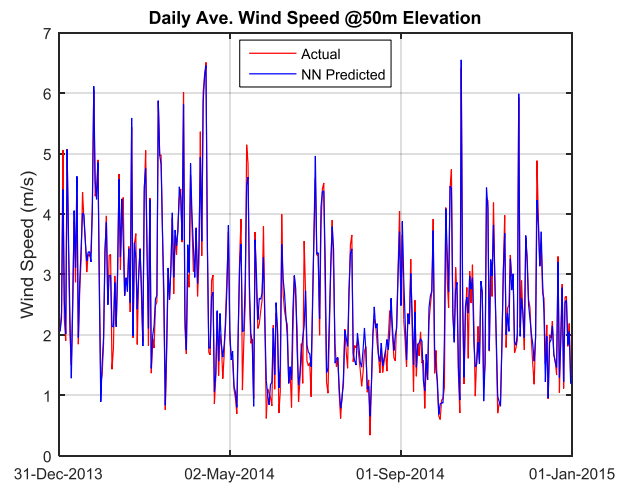
**Figure 7. Predicting Mean Daily Hourly Wind Speed using Bagged Decision Tree (BDT)/Random Forest (RF)**

As these figures show, all of the models seem to predict mean daily wind speed very well using the original data (January 1 – December 31, 2014) that were used in developing the models. The story is, however, very different when it comes to predicting with data that are new to the models. The efficacy of the models and their prediction accuracy were measured using MSE, RMSE, and MAE and may be expressed mathematically, as given in Equations (3-5).

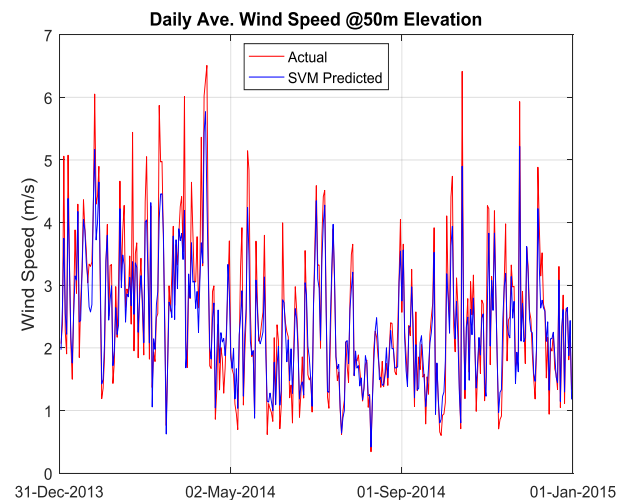
### Short-Term Prediction of Wind Speed

Table 1 depicts the accuracy of the developed models for predicting one-day-ahead mean hourly daily wind speed at an elevation of 50 m in Greensboro, NC, on January 1,

2015. The prediction accuracy for the BDT/RF model was the best, followed by the SVM. The prediction from the FFNN was very poor, in this case, compared with the ensemble method (BDT/RF) and SVM.



**Figure 8. Predicting Mean Daily Hourly Wind Speed using Feed Forward Neural Network (FFNN)**



**Figure 9. Predicting Mean Daily Hourly Wind Speed using Regression Support Vector Machines (SVM)**

**Table 1. Prediction of One-Day-Ahead Hourly Mean Daily Wind Speed in Greensboro, NC, for January 1, 2015**

WIND SPEED (m/s)	MODEL		
	BDT/RF	FFNN	SVM
Actual	1.1309	1.1309	1.1309
Predicted	1.1172	1.8700	1.0335
Prediction Error	0.0137	-0.7391	0.0974

The models were also used to predict wind speed (hourly and average daily) four days ahead, January 1-4, 2015. Figure 10 depicts the plots of the actual and the predicted hourly mean daily wind speed, for the BDT/RF, FFNN, and the regression SVM techniques, respectively.

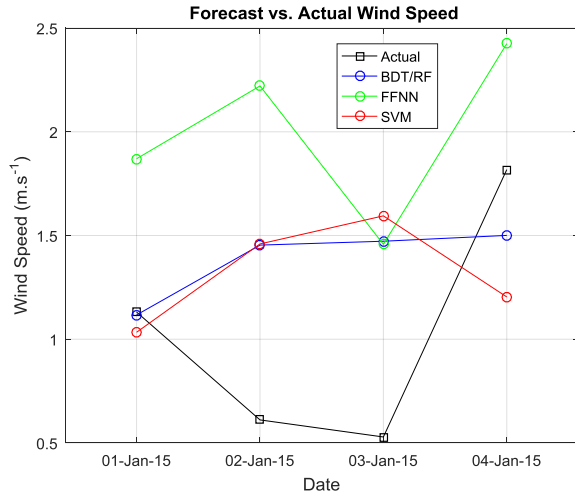


**Figure 10. Predictions of Four-Day-Ahead Mean Daily Wind Speed of the Models**

Table 2 gives the prediction errors for one-day-ahead hourly mean daily wind speed, as measured by the MAE, MSE, and RMSE, for each of the models.

**Table 2. One-Day-Ahead Hourly Prediction Errors of the Predictive Models**

MEASURE	MODEL		
	BDT/RF	FFNN	SVM
MAE	0.1945	0.7426	0.2047
MSE	0.0519	0.7878	0.0522
RMSE	0.2277	0.8876	0.2284

From the table, it is clear that, based on MAE, MSE, and RMSE, the ensemble method (BDT/RF) and SVM model depict better prediction accuracies than the FFNN model. Figure 11 illustrates the four-day-ahead prediction MSEs for the models and confirms the strength of the ensemble techniques and SVMs in predicting wind speed as compared to the neural network.

The previous figures and tables confirm that the ensemble method (BDT/RF), and the SVM are better for predicting short-term wind speed than the FFNN. FFNN models, like most neural network models, normally do show smaller errors (better prediction) when predicting data used in developing the models (refer to Figure 8). They are, however,

weak in predicting new data different from the original data used in developing the models (see Figures 10 and 11). This is where the ensemble techniques and SVM have their strengths.

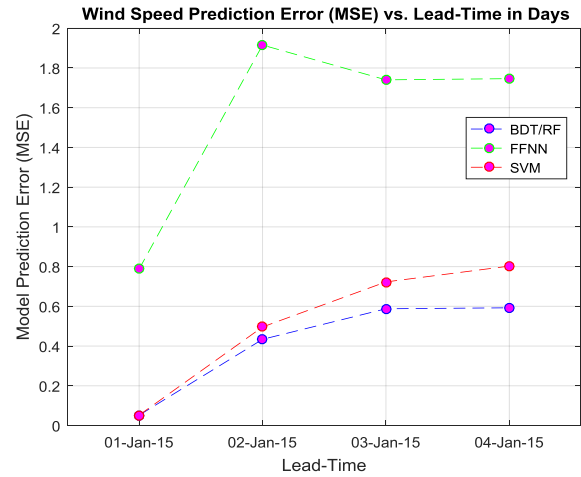


**Figure 11. BDT/RF Prediction of Four-Day-Ahead Mean Daily Wind Speed**

In Figures 7-9, while the FFNN model seems to have a lower prediction error when the prediction data come from the original data used in developing the model, its generalization error for data the model has never seen before (Figures 7-11) tends to be higher than both the BDT/RF and SVM models. In other words, the ensemble method and regression SVM are better predictors (see Table 1) than the FFNN, due to better generalization errors. Another point to note is that, while the models from the ensemble method and the SVM seem to predict very well in one-day-ahead scenarios (or 24-hour period), their accuracy deteriorates as the forecasting horizon increases, but the FFNN model deteriorates much faster than the ensemble and SVM techniques.

## Conclusions

Given the high variability of wind resources over time, their prediction in day-ahead energy markets becomes very important. In addition, wind speed is related to wind power nonlinearly as a cubic function, making the accurate predictions of the former an essential condition for accurately predicting the latter. Because of these, traditional methods such as linear regression and autoregressive integrated moving average models are not very appropriate in predicting wind resources in the short-term. In this study, the authors explored use of supervised machine learning techniques such as random forests (BDT/RF), a feedforward neural network (FFNN), as well as support vector machines (SVM) for pre-

dicting short-term wind speed one day (24 hours) ahead. While the BDT/RF and SVM methods give better prediction accuracies in day-ahead prediction, the FFNN was deemed not to produce better results, as measured by the mean square errors of the predicted wind speed. This could be attributed to the fact the neural networks employ empirical risk minimization and, hence, can give better model accuracy, but when it comes time for predicting with data the model has not seen before, they falter on generalization accuracy. Future work should consider using other neural network techniques such as radial basis function and recurrent neural networks.

## Acknowledgments

Sincere thanks and gratitude to Christian Lotte and Duc Nguyen, former construction management students, who helped with the installation of the weather station that was used in gathering the meteorological data for this research. Financial assistance from the Department of Built Environment and the Office of Student Success, School of Technology, for the acquisition of the weather station is also acknowledged.

## References

- [1] Carpinone, A., Giorgio, M., Langella, R., & Testa, A. (2015). Markov chain modeling for very-short-term wind power forecasting. *Electric Power Systems Research, 122*, 152-158.
- [2] Foley, A. M., Leahy, P. G., Marvuglia, A., & McKeogh, E. J. (2012). Current methods and advances in forecasting of wind power generation. *Renewable energy, 37*(1), 1-8.
- [3] Mendes, J., Sumali, J., Bessa, R. J., Keko, H., Miranda, V., Botterud, A., et al. (2013). *Very Short-Term Wind Forecasting: State-of-the-Art*. (ANL/DIS-14/6). Argonne, IL: Argonne National Laboratory.
- [4] Taylor, J. W., & Buizza, R. (2003). Using weather ensemble predictions in electricity demand forecasting. *International Journal of Forecasting, 19* (1), 57-70.
- [5] Breiman, L. (2001). Statistical Modeling: The Two Cultures (with comments and a rejoinder by the author). *Statistical Science, 16*(3), 199-231.
- [6] Murphy, K. P. (2012). *Machine learning: A probabilistic perspective*. Cambridge, MA: MIT Press.
- [7] Evans, J. S., Murphy, M. A., Holden, Z. A., & Cushman, S. A. (2001). Modeling Species Distribution and Change Using Random Forest. In C. A. Drew, Y.F. Wiersma & F. Huettmann (Eds.), *Predictive Species and Habitat Modeling in Landscape Ecology: Concepts and Applications* (pp. 139-159). New York, NY: Springer.
- [8] Perera, K. S., Aung, Z., & Woon, W. L. (2014). Machine Learning Techniques for Supporting Renewable Energy Generation and Integration: A Survey. In W.L. Woon, Z. Aung, & S. Madnick (Eds.), *Data Analytics for Renewable Energy Integration* (pp. 81-96). Nancy, France: Springer.
- [9] Al Shamisi, M. H., Assi, A. H., & Hejase, H. A. N. (2011). Using MATLAB to Develop Artificial Neural Network Models for Predicting Global Solar Radiation in Al Ain City – UAE. In A. Assi (Ed.), *Engineering Education and Research Using MATLAB* (pp. 219-238). Rijeka, Croatia: InTech.
- [10] Fadare, D. A. (2010). The application of artificial neural networks to mapping of wind speed profile for energy application in Nigeria. *Applied Energy, 87*(3), 934-942.
- [11] Rehman, S., & Mohandes, M. (2008). Artificial neural network estimation of global solar radiation using air temperature and relative humidity. *Energy Policy, 36*(2), 571-576.
- [12] Sözen, A., Arcaklioğlu, E., Özalp, M., & Kanit, E. G. (2004). Use of artificial neural networks for mapping of solar potential in Turkey. *Applied Energy, 77*(3), 273-286.
- [13] Stathopoulos, C., Kaperoni, A., Galanis, G., & Kallos, G. (2013). Wind power prediction based on numerical and statistical models. *Journal of Wind Engineering and Industrial Aerodynamics, 112*(0), 25-38.
- [14] Jursa, R. (2007). Wind power prediction with different artificial intelligence models. *Proceedings of the European Wind Energy Conference EWEC'07*. Milan, Italy.
- [15] Sfetsos, A. (2000). A comparison of various forecasting techniques applied to mean hourly wind speed time series. *Renewable energy, 21*(1), 23-35.
- [16] Yeboah, F. E., Pyle, R., & Bock-Hyeng, C. (2015). Predicting Solar Radiation for Renewable Energy Technologies—A Random Forest Approach. *International Journal of Modern Engineering, 16*(1), 100-107.
- [17] Lei, M., Shiyang, L., Chuanwen, J., Hongling, L., & Yan, Z. (2009). A review on the forecasting of wind speed and generated power. *Renewable and Sustainable Energy Reviews, 13*(4), 915-920.
- [18] Wang, X., Guo, P., & Huang, X. (2011). A Review of Wind Power Forecasting Models. *Energy Procedia, 12*(0), 770-778.
- [19] Potter, C. W., & Negnevitsky, M. (2006). Very Short-term Wind Forecasting for Tasmanian Power



- Generation. *IEEE Transactions on Power Systems*, 21(2), 965-972.
- [20] Mohandes, M. A., Halawani, T. O., Rehman, S., & Hussain, A. A. (2004). Support vector machines for wind speed prediction. *Renewable energy*, 29(6), 939-947.
- [21] Lippmann, R. P. (1987). An introduction to computing with neural nets. *IEEE ASSP Magazine*, 4(2), 4-22.
- [22] Yona, A., & Senjyu, T. (2012). Thermal Energy Collection Forecasting Based on Soft Computing Techniques for Solar Heat Energy Utilization System. *Smart Grid and Renewable Energy*, 3(3), 214-221. doi:10.4236/sgre.2012.3303.
- [23] Yona, A., Senjyu, T., Funabashi, T., Mandal, P., & Kim, C. (2013). Decision Technique of Solar Radiation Prediction Applying Recurrent Neural Network for Short-Term Ahead Power Output of Photovoltaic System. *Smart Grid and Renewable Energy*, 4(6A), 32-38.
- [24] Hagan, M. T., & Menhaj, M. B. (1994). Training feedforward networks with the Marquardt algorithm. *Neural Networks, IEEE Transactions on Neural Networks*, 5(6), 989-993. doi: 10.1109/72.329697
- [25] Kermanshahi, B. (1998). Recurrent neural network for forecasting next 10 years loads of nine Japanese utilities. *Neurocomputing*, 23(1-3), 125-133.
- [26] Kermanshahi, B., & Iwamiya, H. (2002). Up to year 2020 load forecasting using neural nets. *International Journal of Electrical Power & Energy Systems*, 24(9), 789-797.
- [27] Vapnik, V. (1995). *Statistical Learning Theory*. New York, NY: Springer.
- [28] Gunn, S. R. (1998). Support vector machines for classification and regression. Technical Report, University of Southampton.
- [29] Liong, S. Y., & Sivapragasam, C. (2002). Flood Stage Forecasting with Support Vector Machines. *Journal of The American Water Resources Association*, 38(1), 173-186.
- [30] Lee, Y. C. (2007). Application of support vector machines to corporate credit rating prediction. *Expert Systems with Applications*, 33(1), 67-74.
- [31] Pai, P. F., & Lin, C. S. (2005). A hybrid ARIMA and support vector machines model in stock price forecasting. *Omega*, 33(6), 497-505.
- [32] Cristianini, N., & Shawe-Taylor, J. (2000). *An Introduction to Support Vector Machines*. Cambridge, United Kingdom: Cambridge University Press.
- [33] Vapnik, V. (1999). An Overview of Statistical Learning Theory. *IEEE Transactions on Neural Networks*, 10(5), 988-999.

## Biographies

**FRANK E. YEBOAH** is an assistant professor of construction management in the Department of Built Environment, North Carolina Agricultural and Technical State University (NCATSU). He is also a faculty member of the Indiana State University Consortium PhD Program in Technology Management, and a visiting professor of Energy Economics at the Kwame Nkrumah University of Science and Technology in Ghana. He is also a senior research fellow at the Center for Energy Research and Technology at NCATSU. He earned his ME (Dipl.-Ing.) from the Technical University of Clausthal, Germany (Mining and Mineral Economics, 1997), and D.Eng.Sc degree (Earth and Environmental Engineering, 2004) from Columbia University in the City of New York. His research interests include environmental sustainability, energy security and independence, numerical and Monte Carlo simulation of energy systems, applied financial management, risk management, modeling and forecasting using machine learning techniques such as random forest, bagged decision trees, support vector machines, and artificial neural Networks. Dr. Yeboah may be reached at [feyeboah@ncat.edu](mailto:feyeboah@ncat.edu)

**ANDREA N. OFORI-BOADU** is an assistant professor of construction management in the Department of Built Environment, North Carolina Agricultural and Technical State University (NCATSU). She earned her BS degree from the University of Science and Technology, Ghana (Building Technology, 1997). In 2004, she earned her MS (Industrial Technology) degree with a Construction Management specialization from North Carolina Agricultural and Technical State University. Her PhD (Technology Management - Construction Management, 2012) was from Indiana State University. Dr. Ofori-Boadu's research interests include sustainability, quality management and STEM education. She is affiliated with ATMAE, NAWIC, AACEI, and USGBC. Dr. Ofori-Boadu may be reached at [andre-ao@ncat.edu](mailto:andre-ao@ncat.edu)

**PETER A. SAM** is an environmental scientist and adjunct professor of environmental studies and sustainable development at the University of Kansas. He served as a senior executive in-residence and as assistant/associate dean for Research/professor and Graduate Programs at North Carolina A & T University. Dr. Sam has worked both in the private and public sectors (local, state, and federal) and at the international sector (NGO/CSO, International Development/Assistance Agencies and Governments). His research interest is in environmental management and renewable energy. He holds a doctorate degree (Environmental Geography, 2000) from the University of Kansas, a master's degree (Environmental Planning, 1986) from the University of

---

Colorado, and a bachelor's degree (Biology, 1984) from Regis University. Dr. Sam may be reached at [aercgc31@aol.com](mailto:aercgc31@aol.com)

**MUSIBAU A. SHOFOLUWE** is a professor of construction management in the Department of Built Environment, North Carolina Agricultural and Technical State University (NCATSU). He also serves as NCATSU's Coordinator/Faculty Member of the Indiana State University Consortium PhD Program in Technology Management. He is also a visiting professor in the Architecture Department at Bells University of Technology, Ota, Nigeria. Dr. Shofoluwe earned his BS degree (Industrial Technology-Building Construction, 1982) from NCA&T State University; MSc (Technology-Construction Management, 1983) from Pittsburg State University; and Doctorate of Industrial Technology (Construction Management specialization, 1992) from the University of Northern Iowa. He is an OSHA-authorized construction safety trainer, a BPI-certified building Analyst, a certified grants writer/reviewer, and a North Carolina State licensed general contractor. Dr. Shofoluwe's teaching and research interests include construction contracts administration, risk management, sustainable development and construction, construction safety, and construction management practices. Dr. Shofoluwe may be reached at [musibaus@ncat.edu](mailto:musibaus@ncat.edu)

# A SOFTWARE TOOL TO PREDICT THE RISK OF HEREDITARY BREAST CANCER

Rajeev Agrawal, North Carolina A&T State University; Sherin John, North Carolina A&T State University

## Abstract

Breast cancer is a malignant tumor commonly found in women but rarely in men. A family history analysis and genetic test can identify the presence of a potential carrier of the gene behind hereditary breast cancers. In this paper, the authors discuss a software program that can predict inheritable breast cancer. This program can predict the mutation risk in the next generation after analyzing the inheritance pattern of the mutated genes. The software tool combines National Comprehensive Cancer Network (NCCN) guidelines of BRCA1/BRCA2, TP53, and PTEN gene mutations. This tool could help people outside the medical field, who have the least knowledge about breast cancer and genetic inheritance, and help them to identify the presence of the mutated gene. The software tool was developed using JavaScript, HTML, and CSS.

## Introduction

Medical data stored in computers present many promising advantages in medical research. Thus, research that exploits medical data brings new advancements in medical systems. In this computer-driven world, genome mapping and medical technology have made it possible to get genetic information at a low cost, which was not possible earlier. Therefore, exploiting these advancements brings new possibilities to assess a person's risk factors for any disease that is inherited or related to a genetic defect. As the years go by, family health history stored in computers provides better assessments, accuracy, and standardization in forecasting diseases. Combining all known diseases, symptoms, and diagnoses helps medical practitioners to determine and forecast diseases in current and subsequent generations. A family history gives a report about a person and his or her relatives [1]. Families have many common factors, such as genes, lifestyle, environment, and ethnic background. These common factors can relate to some medical conditions that run in families. One can use genetic reports, family history, medical reports, and lab reports to forecast a person's probability of developing inheritable diseases [2, 3]. Study and research about cancer is on the rise for various reasons. The World Health Organization (WHO) estimates significant growth in cancer patients worldwide, and cancer is poised to overtake heart disease as the world's top killer. Cancer screening can detect early symptoms of cancer. Everyone has the risk of

developing cancer in his or her lifetime. The factors behind developing cancer include age, lifestyle, chemicals, radiation, genetics, immune system, and infection [4,5]. Most cancers are non-hereditary, and inherited genetic defects commonly cause hereditary cancers [5]. Hereditary cancer is associated with highly penetrant genes and passes to the next generation through different inheritance patterns [2]. It can be predicted earlier based on a pedigree analysis [6]. A pedigree is a chart or diagram of family history analysis that includes parents, grandparents, and previous generations and checks for the occurrence of any inherited diseases.

A family history analysis and genetic test can identify the potential carrier gene behind breast cancer [7]. The risk factors involved with breast cancers are age, gender, genetic factors, family history, race/ethnicity, and habits [8]. Breast cancer occurs more often in females than in males because of female hormones like estrogen and progesterone, which help cancer cell growth. The risk of developing breast cancer increases with age [9].

## Related Work

The presence of a mutated breast cancer gene is detectable in any person based on the information gathered from a family history [3,7]. Family health history plays a major role in determining the risk factors, as it gives a link to hereditary, environmental, cultural, and behavioral factors of the entire family [7]. Collecting data from close relatives is necessary for determining the risk. Small families may limit risk prediction. Several hereditary cancers might be perfect to include in a family history tool as they can be predicted with higher accuracy through a pedigree analysis. Prediction of diseases like hereditary breast, ovarian, colorectal, and prostate cancers have a high degree of accuracy if developed based on family history [10]. Mutated genes such as BRCA1, BRCA2, PTEN, and TP53 put the individual at a high lifetime risk of breast cancer [11]. There are other genes, such as PALB1, BRIP, and LKB1, behind breast cancer, which contribute moderate risk. However, BRCA1, BRCA2, TP53, and PTEN are the genes considered most often for clinical studies [12].

Both the BRCA1 and BRCA2 genes are responsible for protein involvement in tumor suppression. BRCA1 is located on chromosome 17 and is involved in the repair and regulation of DNA damage. The BRCA2 gene is located on

---

chromosome 13 and is involved in DNA breaks and repairs [13]. Both genes exhibit high penetrance, ranging from 41% to 90% [14], with increased risk of other related cancers such as ovarian cancer, epithelial cancer, pancreatic cancer, and prostate cancer. Male carriers of the BRCA gene confer high risk of breast cancer, especially if the gene is BRCA2 [15]. The risk of breast cancer increases if the person has close blood relatives having breast cancer. The risk increases as the number of affected relatives increases and varies in accordance with people's race and ethnicity [16]. A woman who is an Ashkenazi descendant has more risk of developing breast cancer if she is a carrier of the mutated genes BRCA1 and BRCA2 [16].

PTEN is a tumor suppressor gene that regulates normal cell processes including growth, adhesion, migration, invasion, and apoptosis [17]. Approximately 80% of patients carry the mutated PTEN gene if they meet NCCN clinical criteria for Cowden syndrome [15, 18]. Women identified with Cowden syndrome have a high risk of benign fibrocystic breast diseases, and their lifetime risk of breast cancer is estimated at 25%-50% with an average age between 38 and 46 years at diagnosis [15].

The tumor protein TP53 is another gene that causes breast cancer, which is common in women with Li-Fraumeni syndrome (LFS) [15]. There are different tumors associated with the LFS syndrome [19]. The LFS tumor spectrum includes soft tissue sarcoma, osteosarcoma, pre-menopausal breast cancer, brain tumors, adrenocortical carcinoma, leukemia, and lung bronchioloalveolar cancer (LFS tumor spectrum) [15]. The lifetime risk of breast cancer in a woman with the TP53 gene is 49% by the age of 60 [20]. According to clinical studies, a patient with invasive breast cancer and no family history of a core cancer has a 0% chance of having the p53 mutation. However, a person with breast cancer under age 30 and a family history of one or more core cancers in a first- or second-degree relative has a 100% chance of having the p53 mutation [20].

Many software programs are available for assessing breast cancer risk and screening. Based on the Gail model, scientists at the National Cancer Institute (NCI) have developed the Breast Cancer Risk Assessment Tool (<http://www.cancer.gov/BCRISKTOOL>) [21]. The IBIS tool (the international breast cancer intervention study, also called the Tyrer-Cuzick model) is used to calculate a person's likelihood of carrying the BRCA 1 or 2 mutations, which are associated with increased breast cancer risk (<http://www.ems-trials.org/riskevaluator>) [22]. The Myriad II risk assessment tool (<http://www.myriadpro.com/bcrisk-calculator/calc.htm>) was developed based on empirical data from 10,000 women with germline mutations in BRCA1/

BRCA2 genes [23]. BOADICEA is another tool used in conjunction with MENDEL, pedigree software (<http://ccge.medschl.cam.ac.uk/boadicea/advice-for-the-public/>), which estimates the risks of breast and ovarian cancer in women [15]. This is a free Web-based tool (<http://www.afcri.upenn.edu/itacc/penn2/>) that uses logistic regression based on pedigrees from Europe and North America [24]. The Breast Cancer Surveillance Consortium (BCSC) risk calculator was created by participating scientists (<https://tools.bcscc.org/BC5yearRisk/intro.ht>) [25]. The Hall Detailed Breast Risk Calculator is another open source breast cancer risk calculator designed by Dr. Halls (<http://halls.md/breast/risk.ht>) [26]. This risk assessment tool includes many factors not included in the Gail model.

These tools have many limitations and only consider the BRCA1 or BRCA2 mutations. None of the existing breast cancer tools available considers other high-risk genes such as PTEN and TP53 [27] and related diseases [12]. Many of the existing tools are proprietary and not available to the general public and were developed from data collected from particular demography or ethnicity, and many of these tools do not consider third-degree relatives and family history. This software program combines BRCA1/BRCA2, TP53, and PTEN gene risk. It was developed based on the NCCN guidelines to predict BRCA1, BRCA2, TP53, and PTEN mutation risk.

The NCCN is an association of 25 global leading cancer centers. The association develops guidelines for most cancers and updates by 47 individual panels, including over 950 clinicians and oncology researchers from 25 member NCCN institutions. The panel members include clinicians and researchers from a number of academic disciplines. According to NCCN guidelines [15], "It should be emphasized that these guidelines were not developed as a substitute for professional genetic counseling. Although, cancers other than breast and ovarian cancers are associated with these hereditary syndromes, the main focus of this NCCN Guidelines is on the management of breast and ovarian cancer risk in these individuals."

## Proposed Design for the Software Tool

Figure 1 shows the proposed block diagram of the program. This software tool considers different possibilities, including inheritance pattern, family history assessments, and medical reports, to generate the program. As described earlier, this program has three sections (BRCA1/BRCA2 checking, TP53 checking, and PTEN mutation checking). Figure 1 shows how the program analyzes personal history, family history, and already known mutation conditions. The program checks individual known mutation history,

personal history, and family history for BRCA1/BRCA2, TP53, and PTEN gene mutations. The results contain the risk of passing on the mutation risk, or getting cancer, to the next generation. The family history includes first-, second-, and third-degree relatives' health history. Different models and software programs have been developed to predict the risk of breast cancer [28, 29]. Existing tools for checking hereditary breast cancer only consider the BRCA1/BRCA2 genes. However, these tools do not consider other genes such as TP53 and PTEN that are risk factors in breast cancer. Some of the tools do not consider family history. This software program includes PTEN and TP53 genes and considers first-, second-, and third-degree relatives.

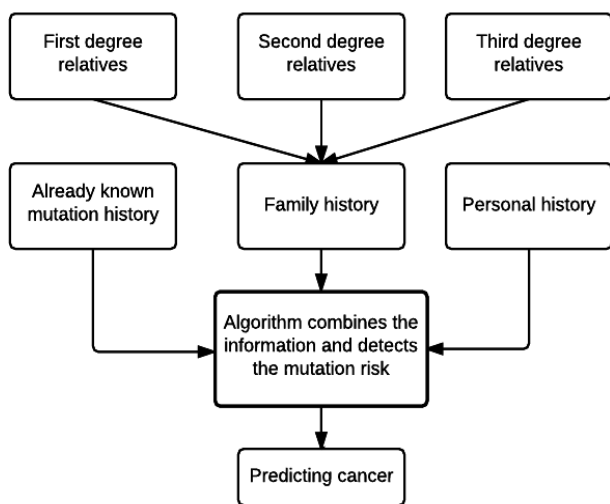


Figure 1. Proposed Design for the Software Tool

## Software Tool

The backbone of this software program includes the NCCN guidelines. The program analyzes the inheritance pattern of the gene to check the risk of cancer in the next generation. Based on the guidelines, the analysis was divided into three sessions: 1) hereditary breast/ovarian cancer syndrome analysis; 2) Li-Fraumeni syndrome analysis; and, 3) Cowden syndrome analysis. These three are related to germline mutations of BRCA1/BRCA2, TP53, and PTEN gene mutations and have a high impact on hereditary breast cancer diagnoses.

## Hereditary Breast/Ovarian Cancer Syndrome Analysis

The logical flowcharts for checking hereditary breast and ovarian cancers are explained in this section. This part would check different criteria defined by the NCCN to de-

tect the presence of the BRCA1/BRCA2 genes. Based on NCCN guidelines, the analysis of the flowchart was divided into three sections: 1) individuals with already known or diagnosed BRCA1/BRCA2 mutations; 2) checking the personal history of different types of cancer histories such as breast cancer, epithelial ovarian cancer, male breast cancer, pancreatic or prostate cancer, and Ashkenazi ancestry; and, 3) checking family history of the person.

- 1) Persons with a known mutation: This part will check whether an individual has already been diagnosed with BRCA mutations or if he or she has a known personal/family history of a BRCA1/BRCA2 mutation.
- 2) Personal history: The program analyzes the personal history of cancers related to the BRCA1 and BRCA2 mutations. This section was divided into four subsections: (a) personal history of breast cancer, (b) epithelial ovarian cancer, (c) male breast cancer, and (d) pancreatic or prostate cancer.
  - (a) The personal history of breast cancer was divided into four different age groups: 45 and under, 50 and under, 60 and under, and diagnosed at any age. The tool considers the result positive (at risk) if any individual with a personal history of breast cancer meets any of the following criteria:
    - Diagnosed at the age of 45 or under.
    - Diagnosed at the age of 50 or under and having two breast primaries or with one or more close relatives with breast cancer at any age or with unknown family history.
    - Diagnosed at the age of 60 or under with triple-negative breast cancer.
    - Diagnosed at any age with one or more close relatives with breast cancer diagnosed at the age of 50 years or younger OR with a relative with epithelial cancer at any age OR two or more relatives with pancreatic cancer or prostate cancer OR having a close relative with male breast cancer OR belonging to Ashkenazi ancestry.

Figure 2 shows the procedures of personal history analysis of BRCA1 or BRCA2 mutation risk.

- (b) A person diagnosed with epithelial cancer at any age will be at risk of hereditary breast cancer.
- (c) Personal history of male breast cancer is a potential factor related to hereditary breast cancer. Men with breast cancer are more susceptible to the BRCA2 gene mutation than the BRCA1 mutation. The lifetime risk of breast cancer with the BRCA2 gene is 6% by the age of 70, but only 1% with the BRCA1 gene.





---

(d) Men with BRCA1 or BRCA2 mutations have a higher risk of developing prostate cancer. Both men and women with BRCA1 or BRCA2 mutations have a higher risk of pancreatic cancer. The result will be “at risk” if the person has a personal history of prostate cancer or pancreatic cancer at any age, and has two or more close relatives with breast, ovarian, pancreatic, or prostate cancer. For pancreatic cancer, if the person belongs to Ashkenazi Jewish ancestry, only one affected relative is sufficient to put the person at risk [15].

- 3) Family history: In the next section, the program checks the family history. The tool examines the family history and determines the risk based on frequency of cancer appearing in first-, second-, or third-degree relatives. The output is stored based on the analysis of the family history. This section was separated into two parts in order to qualify the different conditions for the diagnosis:
- (a) First- or second-degree relatives, who satisfy the conditions.
  - (b) Third-degree relatives with breast cancer and/or ovarian cancer with two or more close blood relatives with breast cancer (one at least before the age of 50) or ovarian cancer.

After collecting the information about already known or diagnosed mutations of the BRCA1/BRCA2 gene, the program checks the personal history for breast cancer. To do this, the flowchart was divided into four groups, based on different age categories. The risk criteria are met if the person is under age category ‘a’ (age  $\leq 45$ ) and there are no additional criteria needed to satisfy the ‘at risk’ condition. The criteria are met if the person is under or at the age of 50 and if he or she has any additional primary breast cancers or more than one close blood relative with breast cancer. The person is at risk if he or she has an unknown family history. The result is stored if the person is identified as having a triple-negative breast cancer and is under the age of 60. For the at-any-age category, the criteria are met if there is more than one close blood relative with breast cancer at age 50 or younger, has more than two close blood relatives with breast cancer at any age, has more than one close blood relative with male breast cancer, or has more than one close blood relative with pancreatic or prostate cancer. The result is stored if the person belongs to Ashkenazi ancestry and if the person has a personal history or family history of breast or prostate cancer. After checking the personal history for pancreatic or prostate cancer, the family history of breast, ovarian, pancreatic, and prostate cancers is checked. If two or more relatives from the same side of the family are affected with any of these cancers, the result is stored as “at

risk.” For pancreatic cancer, if the person belongs to Ashkenazi ancestry, then only one affected relative is needed to meet the criteria.

After collecting the information of already known or diagnosed gene mutation, the relative’s family history is checked. For that, the flowchart collects the information about first- or second-degree relatives’ personal history of breast cancer. Checking personal history of breast cancer was divided into four categories based on age group. The information is collected separately for different age categories. After that, the flowchart checks if the person has a history of epithelial ovarian cancer. Next, it checks for the presence of pancreatic and prostate cancer and if there is a history of male breast cancer. If the person has a first- or second-degree relative with these cancers, the result is stored and entered into the next section.

To check a third-degree relative’s family history, a different method was followed. If a third-degree relative is identified with breast or ovarian cancer, the flowchart checks the number of other relatives identified with breast or ovarian cancer on the same side of the family. The result is stored as ‘at risk’ if there are more than two people identified with breast or ovarian cancer (one at least before the age of 50). The risk of breast cancer increases if the person has close blood relatives with a history of breast cancer. Figure 3 is an image of the software program checking personal history of breast cancer; Figure 4 shows the flowchart of a family history analysis. The same steps that were used for checking personal history analysis are used to check the family history (only for first- or second-degree relatives) analysis. The risk increases as the number of affected relatives increases and varies with people’s race and ethnicity. The next section analyzes Li-Fraumeni syndrome (TP53).

## Li-Fraumeni Syndrome Analysis

At this stage, the software tool checks the presence of the Li-Fraumeni syndrome (LFS), as breast cancer is common in these women. The flowchart to check the TP53 mutation (LFS) is given in flowchart section b. The program can be divided into four parts based on different checking criteria. In this section, the software tool checks four different conditions: 1) an individual with known mutations; 2) classic LFS criteria; 3) Chompret criteria; and, 4) early age onset criteria. Figure 3 shows how the analysis was done.

- 1) Individual from a family with known mutation: In this part, the program checks to see if the individual is from a family that has already been diagnosed with the mutation of TP53. If the individual already has the mutation of TP53, then the program would consider the person at

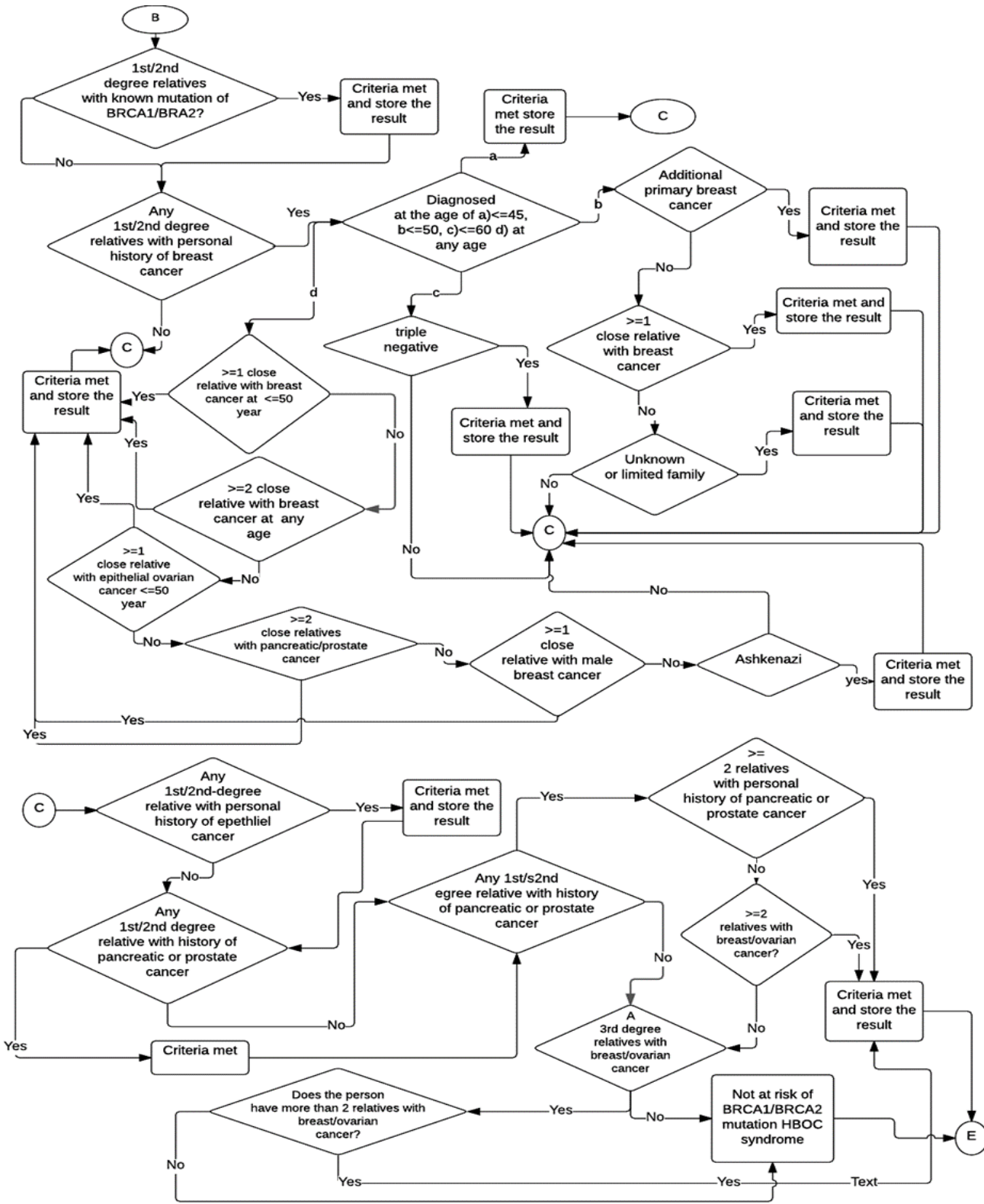


Figure 4. Flowchart—BRCA1/BRCA2 Family History Analysis

risk and enter into the next section after storing the result.

**Breast Cancer Analysis Tool**

**Personal History - Checking BRCA1/BRCA2 mutation**

- Do you have any family member with known hereditary breast cancer(BRCA1/BRCA2 mutation)?
- Have you ever diagnosed with breast cancer?
- Select the following criteria if you have diagnosed with Breast Cancer:
  - Diagnosed  $\leq 45$  year old
  - Diagnosed  $\leq 50$  y and with the following:
  - Diagnosed  $\leq 60$  year old with triple negative breast cancer
  - Diagnosed at any age with any of the following:
- Do you have ever diagnosed with epithelial ovarian cancer?
- Do you have ever diagnosed with male breast cancer?
- Personal history of prostate cancer at any age with any of the following:
- Belongs to Ashkenazi Jewish family:
- Personal history of pancreatic cancer with any of the following:

**Figure 3. Personal History Analysis—BRCA1/BRCA2**

- Checking classic LFS criteria: To meet NCCN criteria for classic LFS criteria, the person should satisfy all three of the following conditions:
  - The individual was diagnosed with sarcoma (cancer related to connective tissues) before the age of 45 years.
  - The individual has a first-degree relative with cancer, and it was diagnosed before the age of 45.
  - The individual has one or more first- or second-degree relatives with cancer diagnosed before the age of 45 or with a sarcoma at any age.
- Checking Chompret criteria: This part of the program analyzes the following three conditions. If any of the conditions are met, the output is stored, and the program exits from the section.
  - The individual has a tumor from the LFS tumor spectrum (soft-tissue sarcoma, osteosarcoma—cancer develops in the bone—brain tumor, breast cancer, adrenocortical carcinoma, leukemia, lung broncho alveolar cancer) before 46 years of age, and one or more first- or second-degree relatives with cancers that are included in the LFS spectrum before the age of 56 years or with multiple primaries at any age.
  - The individual has multiple tumors with at least two of them belonging to the LFS spectrum and diagnosed before the age of 46 years.
  - The individual was diagnosed with adrenocortical carcinoma (a cancer that begins at the outer layer of the adrenal gland) or choroid plexus carcinoma (a tumor that arises from brain tissues) at any age of onset, regardless of the family history.

- If the individual was diagnosed with breast cancer before the age of 35, he or she is a person at risk of TP53 mutation.

Figure 5 is an image of the software program, and Figure 6 represents the flowchat for TP53 analysis.

**Breast Cancer Analysis Tool**

**Checking Li-Fraumeni Syndrome (Tp53 mutation)**

- Individual from a family with known mutation of Tp53?
- Have you ever diagnosed with sarcoma before the age of 45?
- Do you have a 1st degree relative diagnosed with cancer before the age of 45?
- Do you have a 1st or 2nd degree relative with a cancer before age 45 or sarcoma at any age?
- Please select if you have diagnosed with any (before the age of 46):
- Please select if you have 1st or 2nd degree relative diagnosed with any (before the age of 56):
- Do you have diagnosed with any of the condition in the list before the age of 46 (press ctrl to select multiple)?
- At least one first- or second degree relative diagnosed before the age of 56 with:

*The LFS tumor spectrum includes osteogenic and chondrosarcoma, rhabdomyosarcoma, breast cancer, brain cancer (especially glioblastomas), leukemia, lymphoma, and adrenocortical carcinoma.*

- Have you ever diagnosed with:
- Early age at onset (before the age of 35) of breast cancer?

**Figure 5. TP53 Analysis**

As Figure 6 shows, the information is collected if the person already has a TP53 mutation. In the next step, it checks whether the person meets classic LFS criteria or not. In order to check the classic LFS criteria, the flowchart checks if the person has a sarcoma before the age of 45. If the person has been diagnosed with sarcoma, a check is made of the first or second relative’s history of cancer before the age of 50. If the first- or second-degree relative has cancer, it checks the additional relative’s history of cancer. The result will be stored as “at risk” if all three criteria have been met. Next, the procedure enters into the Chompret criteria section and starts by identifying an individual with a tumor that belongs to the LFS tumor spectrum before the age of 46. The LFS tumor spectrum includes sarcoma, brain tumor, breast cancer, leukemia, adrenocortical carcinoma, and lung broncho alveolar cancer. Next, the relative’s history of LFS tumors (including breast primaries) is checked if the individual is identified as having LFS tumors. After that, it checks whether the individual has multiple tumors and if two or more of them belong to the LFS spectrum or not. If yes, the result is stored as “at risk.” In the final step, the flowchart checks to see if the individual has been diagnosed with adrenocortical carcinoma or Choroid plexus carcinoma.

In the next step, the flowchart checks if the person had been diagnosed with breast cancer before or at the age of 35. If the person meets the criterion, he or she is at risk of both TP53 and BRCA gene mutations. The result is collected and the program enters into PTEN mutation analysis.

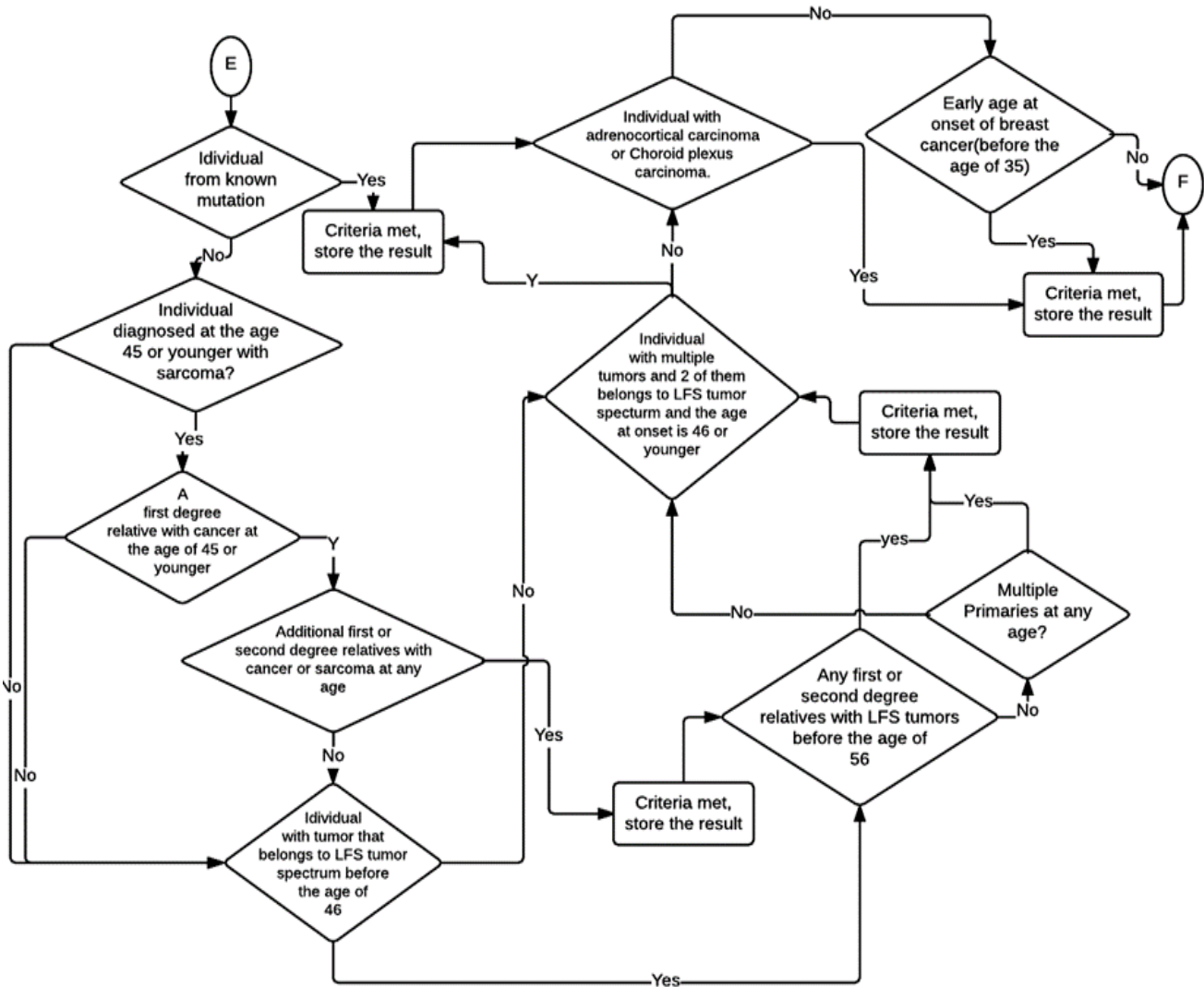


Figure 6. Flowchart—Tp53 Analysis

## Cowden Syndrome Analysis

In this part, the program checks the PTEN (Cowden syndrome) mutation. The Cowden syndrome is related to mutations in the PTEN gene. In order to calculate the risk, the flowchart checks four criteria. There are major and minor criteria that, if satisfied, would identify the person to be at risk. Major criteria include breast cancer, endometrial cancer, Follicular thyroid cancer, multiple GI hamartomas or ganglioneuromas, macrocephaly (58 cm in adult women, 60 cm in adult men), macular pigmentation of glans penis, and mucocutaneous lesions with one biopsy-proven trichilemmoma, or multiple palmoplantar keratosis or multi-

focal or extensive oral mucosal papillomatosis or multiple cutaneous facial papules. Minor criteria include esophageal glycogenic acanthoses, lipomas, mental retardation, papillary or Follicular variant of papillary thyroid cancer, thyroid structural lesions, renal cell carcinoma, single GI hamartoma or ganglioneuroma, testicular lipomatosis, or vascular anomalies.

First, the flowchart (see Figure 7) checks to see if the person already has the PTEN gene mutation and then the result is collected. In next step, if the individual meets the clinical diagnostic criteria for CS/PHTS, the information is collected. After that, it checks the personal history of Bannayan-



Riley-Ruvalcaba syndrome, and the information will be stored if identified. Next, the flowchart enters into a check of personal history for adult Lhermitte-Duclos disease, and the result will be stored if the person has or had a history of the disease. Then, it checks the personal history for autism spectrum disorder and macrocephaly condition. After that, it checks for the presence of two or more biopsy-proven trichilemmomas as well as if the person meets three major clinical diagnostic criteria without macrocephaly.

Next, the flowchart enters into the identification of two or more major criteria with macrocephaly or whether the person meets one major criterion and more than three minor criteria. In the next step, the flowchart checks whether the individual meets more than four minor criteria or not. The result is stored if any of the individual's family members meet one major criterion and two or more minor criteria. In the final section, the results stored from different sections are combined and displayed. The final output gives a separate report based on the three sections.

Figure 7 represents the flowchart to check the PTEN mutation. Figure 8 is a screenshot of the PTEN analysis section. Figure 7 shows how the program checks individual known mutation history, personal history, and family history. The major and minor criteria dropdowns include different clinical criteria for PTEN gene testing.

The program has four sections: 1) an individual from a family with an already known mutation, 2) an individual meeting clinical diagnostic criteria, 3) an individual with personal history and other NCCN criteria, and 4) an individual with a close blood relative meeting NCCN criteria.

- 1) First, the flowchart will check if the individual has a known mutation of the PTEN gene.
- 2) An individual with a personal history of any of the following diseases:
  - (a) Bannayan-Riley-Ruvalcaba syndrome
  - (b) Adult Lhermitte-Duclos diseases
  - (c) Autism spectrum disorder and macrocephaly
  - (d) Two or more biopsy-proven trichilemmomas
  - (e) Two or more major criteria
  - (f) Three major criteria, without macrocephaly
  - (g) One major and more than three minor criteria
  - (h) More than four minor criteria
- 3) The program checks the family history of close blood relatives with any one or more major criteria or two or more minor criteria. The program stores the test results before starting the next section. Figure 8 is an image of the PTEN analysis program.

Figure 8. PTEN Analysis

## Forecasting Cancer in Future Offspring

Children inherit two copies from their parents, one from their mother and one from the father. BRCA1/BRCA2, TP53, and PTEN genes are not associated with x-linked inheritance. Therefore, children can inherit the mutations. Offspring of the individual with any of these gene mutations can inherit the mutation. As BRCA1, BRCA2, TP53, and PTEN genes exhibit autosomal dominant inheritance pattern, there are four possible combinations for the children's gene copy. As shown in Figure 9, two of the four, or 50%, can inherit the mutated genes (aA, aA). The other 50% do not inherit the mutated genes (AA, AA). These four combinations are possible every time a pregnancy occurs. The gender of the children does not matter. Consider a mother who carries the BRCA1 mutated gene, and her partner carries normal genes. In each pregnancy, the chances of a having normal child is 50% and the chances of a child with the abnormal gene is also 50%. Using this information, one can predict the probability of hereditary breast cancer in the offspring to be born, if this tool determines the individual to be at risk.

## Output

In the final session, the output from different sections is combined and displayed along with the next generation's risk, with different outputs based on the different sections. The result contains mutated gene risk and breast cancer risk. The result also displays the risk of passing mutated genes on to the next generation. However, the result is not a substitution for a professional genetic test. If the individual is at risk, the tool recommends a discussion with an oncologist

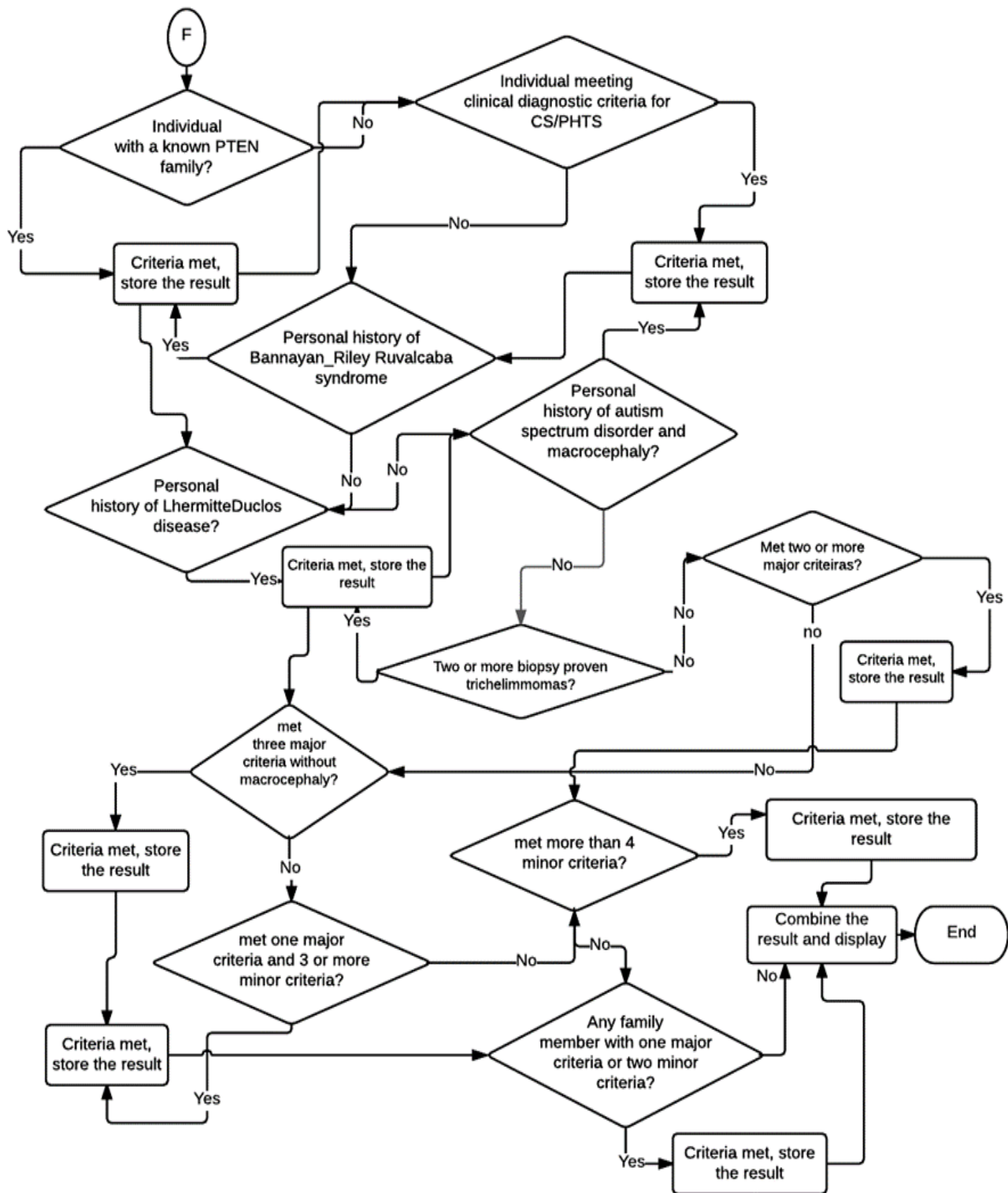


Figure 7. Flowchart—PTEN Analysis

for better treatment. This program will have four different outputs based on different gene mutation analyses: BRCA1/BRCA2, TP53, PTEN, and not-at-risk situations. The user can print the result and consult an oncologist for further assessments and treatments. Figure 10 depicts an output scenario of a person, who meets the family history criterion of the HBOC syndrome analysis.

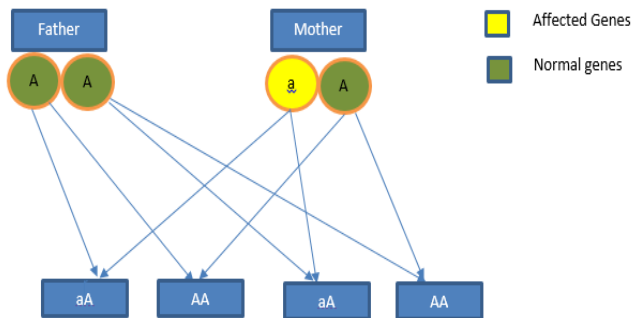


Figure 9. Autosomal Dominant Inheritance Pattern

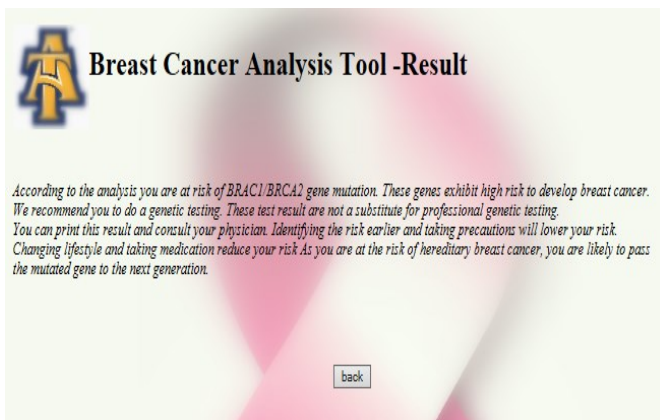


Figure 10. Output—BRCA1/BRCA2 Mutation

Figure 11 shows the analysis result from a Cowden syndrome or PTEN gene mutation. Figure 12 is a screen image of the output of the program for a user who met the TP53 mutation criteria. Figure 13 represents the output for a user who does not meet any criteria.

## Features of the Program

The program

- includes PTEN and TP53 genes: This tool includes high-risk TP53 and PTEN genes; none of the existing breast cancer tools available considers these high-risk genes.
- takes into account ovarian, prostate, and pancreatic cancer history.

- includes Ashkenazi Jewish history.
- is available to the public: many of the existing tools are proprietary and are not available to the public but this tool is open source.
- is user-friendly: this is a very easy-to-use software tool and any person with basic knowledge in computer operation can easily use it.
- is easy to understand: It is easily understood by people who have little breast cancer awareness.
- has universal acceptance: This tool was designed based on NCCN guidelines and is not restricted to a set of people based on their demography or ethnic group. The guidelines were developed in coordination with 25 global leading cancer centers. Most of the existing tools were developed based on the data collected from a particular demography.
- includes third-degree relatives: Considers family history that includes first-, second-, and third-degree relatives. Many tools available do not consider third-degree relatives and family history.

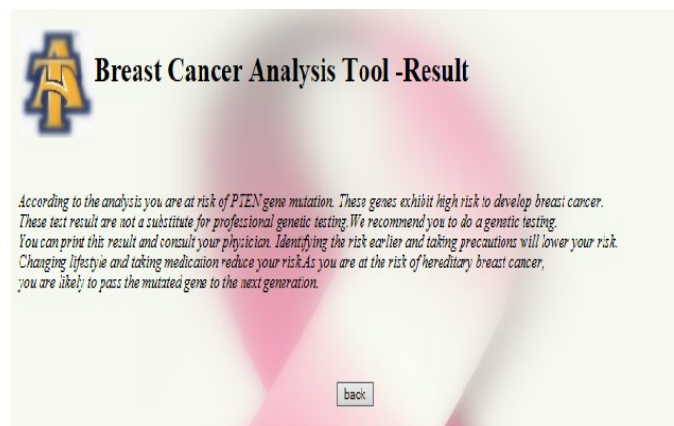


Figure 11. Output—PTEN Mutation

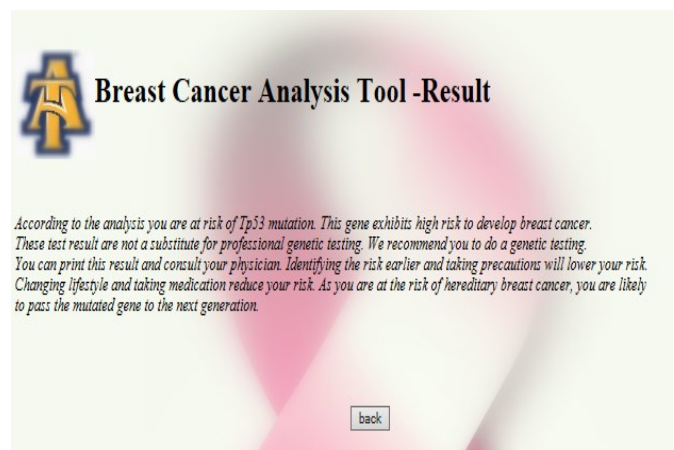


Figure 12. Output—TP53 Mutation



**Figure 13. Output—“not-at-risk” Case**

Early detection and screening would help to prevent cancer or to find the disease at an early age. Taking drugs would prevent or delay cancer onset if the individual is at risk of hereditary breast cancer syndrome. For example, medicines such as Tamoxifen and Raloxifene lower breast cancer risk in the general population [30]. Individuals at risk may choose to have surgery to reduce their risk. The individual at risk is strongly recommended to have breast or ovarian cancer screening, including mammograms, MRI exams, ultrasound, and breast exams, performed by a physician.

## Conclusions and Future Work

Predicting disease with computer modeling and mathematical analysis is becoming more popular. Combining all known diseases and diagnoses would help medical practitioners to determine and predict diseases in current or next generations. As the years go by, family health history stored in computers provides better assessments, accuracy, and standardization in forecasting diseases. Integrating this tool with other common inherited diseases such as cystic fibrosis, Down syndrome, type-2 diabetes, inherited heart diseases, or other hereditary cancers, will help both common people and medical professionals. The future version will be a comprehensive computer software application to predict most of the common inheritable and predictable diseases. This tool may also include more hereditary and non-hereditary cancers and be improved to include other moderate-risk genes such as PALB1, BRIP, and LKB1. Other non-hereditary risk factors such as lifestyle and diet can also improve prediction accuracy. A smartphone version of this tool can provide anytime access to users.

## References

[1] Agrawal, R., Suleiman, M., Seay, C., & Gloster, C. (2013). Dynamic Disease Forecast Network Using

Family Medical History. *IEEE International Conference on Healthcare Informatics*, 486-486.

[2] American Cancer Society. Genetic Testing for Cancer: What You Need to Know. Retrieved from <http://www.cancer.org/acs/groups/cid/documents/webcontent/002548-pdf>

[3] Yoon, P. W. (2002). Can family history be used as a tool for public health and preventive medicine? *Genetics in Medicine*, Jul-Aug, 4(4), 304-10.

[4] Anand, P., Kunnumakara, A. B., Sundaram, C., Harikumar, K. B., Tharakan, S. T., Lai, O. S., et al. (2008). Cancer is a preventable disease that requires major lifestyle changes. *Pharmaceutical research*, 25(9), 2097-2116.

[5] American Cancer Society-What causes cancer? Retrieved from <http://www.cancer.org/cancer/cancercauses/index>

[6] Riley, B. D., Culver, J. O., Skrzynia, C., Senter, L. A., Peters, J. A., Costalas, et al. (2012). Essential elements of genetic cancer risk assessment, counseling, and testing: updated recommendations of the National Society of Genetic Counselors. *Journal of Genetic Counseling*, 21(2), 151-161.

[7] Yoon, P. W., Scheuner, M. T., & Khoury, M. J. (2003). Research priorities for evaluating family history in the prevention of common chronic diseases. *American Journal of Preventive Medicine*, 24(2), 128-135.

[8] American Cancer Society. What are the risk factors for breast cancer? Retrieved from <http://www.cancer.org/cancer/breastcancer>

[9] Centers for Diseases Control and Prevention - What Are the Risk Factors for Breast Cancer? Retrieved from [http://www.cdc.gov/cancer/breast/basic\\_info/risk\\_factors.htm](http://www.cdc.gov/cancer/breast/basic_info/risk_factors.htm)

[10] Qureshi, N., Wilson, B., Santaguida, P., Carroll, J., Allanson, J., Culebro, et al. (2007). Collection and use of cancer family history in primary care, *US Department of Health and Human Services, Public Health Service, Agency for Healthcare Research and Quality*.

[11] U.K. Cancer Research. Breast Cancer Genes. Retrieved from <http://www.cancerresearchuk.org/about-cancer/type/breast-cancer/about/risks/breast-cancer-gene>

[12] Allain, D. C. (2008). Genetic counseling and testing for common hereditary breast cancer syndromes. *The Journal of Molecular Diagnostics*, 10(5), 383-395.

[13] Murray, A. J., & Davies, D. M. (2013). The genetics of breast cancer. *Surgery (Oxford)*, 31(1), 1-3.

[14] Chen, S., & Parmigiani, G. (2007). Meta-analysis of BRCA1 and BRCA2 penetrance. *Journal of Clinical Oncology*, 25(11), 1329-1333.



- 
- [15] Daly, M. B., Axilbund, J. E., Buys, S., Crawford, B., Farrell, C. D., Friedman, S., et al. (2010). Genetic/familial high-risk assessment: breast and ovarian. *Journal of the National Comprehensive Cancer Network*, 8(5), 562-594.
- [16] American Cancer Society-What is breast cancers. Retrieved from <http://www.cancer.org/cancer/breastcancer/detailedguide/breast-cancer-what-is-breast-cancer>
- [17] Yamada, K. M., & Araki, M. (2001). Tumor suppressor PTEN: modulator of cell signaling, growth, migration and apoptosis. *Journal of Cell Science*, 114(13), 2375-2382.
- [18] Gonzalez, K. D., Noltner, K. A., Buzin, C. H., Gu, D., Wen-Fong, C. Y., Nguyen, et al. (2009). Beyond Li Fraumeni Syndrome: clinical characteristics of families with p53 germline mutations. *Journal of Clinical Oncology*, 27(8), 1250-1256.
- [19] Masciari, S., Dillon, D. A., Rath, M., Robson, M., Weitzel, J. N., Balmana, J., et al. (2012). Breast cancer phenotype in women with TP53 germline mutations: a Li-Fraumeni syndrome consortium effort. *Breast Cancer Research and Treatment*, 133(3), 1125-1130.
- [20] National Cancer Institute - Breast Cancer Risk assessment tool. Retrieved from <http://www.cancer.gov/brisktool>
- [21] Boughey, J. C., Hartmann, L. C., Anderson, S. S., Degnim, A. C., Vierkant, R. A., Reynolds, C. A., et al. (2010). Evaluation of the Tyrer-Cuzick (International Breast Cancer Intervention Study) model for breast cancer risk prediction in women with atypical hyperplasia. *Journal of Clinical Oncology*, 28(22), 3591-3596.
- [22] United States Department of Health and Human Services. My Family Health Portrait. Retrieved from <https://familyhistory.hhs.gov/fhh-web/home.action>
- [23] University of Pennsylvania, The Penn II BRCA1 and BRCA2 Mutation Risk Evaluation, Retrieved from <http://www.afcri.upenn.edu/itacc/penn2>
- [24] Breast Cancer Surveillance Consortium Risk Calculator, Retrieved from <https://tools.bscsc-ccc.org/BC5yearRisk/calculator.htm>
- [25] Detailed Breast Cancer Risk Calculator. Retrieved from <http://halls.md/breast/risk.ht>
- [26] USA. National Cancer Institute. A to Z List of Cancers. Retrieved from <http://www.cancer.gov/cancertopics/types/alphalis>
- [27] U.K. Cancer Research U.K. Breast cancer genes. Retrieved from <http://www.cancerresearchuk.org/about-cancer/type/breast-cancer/about/risks/breast-cancer-gene>
- [28] National Cancer Institute. Breast Cancer Risk Prediction Models. Retrieved from, [http://epi.grants.cancer.gov/cancer\\_risk\\_prediction/breast.htm](http://epi.grants.cancer.gov/cancer_risk_prediction/breast.htm)
- [29] Evans, D., & Howell, A. (2007). Breast cancer risk-assessment models. *Breast Cancer Research*, 9(5), 213.
- [30] Moyer, V. A. (2013). Medications for risk reduction of primary breast cancer in women: US Preventive Services Task Force recommendation statement. *Annals of Internal Medicine*, 159(10), 698-708.

## Biographies

**RAJEEV AGRAWAL** is an assistant professor in the Department of Computer Systems Technology at North Carolina A&T State University. He earned his BS degree from G.B. Pant University, India; MS degree from Thaper University, India; and, PhD from the Wayne State University. His interests include health informatics, big data analytics, and cloud security. Dr. Agrawal may be reached at [ragrawal@ncat.edu](mailto:ragrawal@ncat.edu)

**SHERIN JOHN** completed her MS in information technology in spring 2015 from North Carolina A&T State University and MS (Electronics, 2005) from Mahatma Gandhi University, India. Ms. John may be reached at [sherin\\_jhn@yahoo.com](mailto:sherin_jhn@yahoo.com)



# ENERGY EFFICIENCY PERFORMANCE OF CONTROLLERS ON AIR-OPERATED DOUBLE-DIAPHRAGM PUMPS

David W. Goodman, Indiana University-Purdue University Indianapolis;  
Robert J. Durkin, Indiana University-Purdue University Indianapolis

## Abstract

In this study, the authors conducted comparative validation testing and analysis of standard and new air-operated diaphragm pump controllers. The experiments compared energy consumption of four air-operated double-diaphragm (AODD) pumps using conventional air controls with consumption using a new smart supply valve. In all trials and at all set points, the new controller reduced diaphragm pump air consumption. The air consumption reductions varied by pump, but the new controller reduced the AODD mean air consumption by 19.9% to 47.8%. The supply air pressure and pump fluid flow rates varied but did not significantly impact pump performance. The equations developed in this study can predict the percentage of air consumption savings for new pumps or existing pumps when the fluid flow rate is known.

## Introduction

The international market size for fluid transfer pumps was recently estimated to have exceeded \$27.1 billion in 2010 [1]. This market is dominated by four technologies; centrifugal (62.0%), reciprocating (12.1%), rotary (11.8%), and diaphragm (9.4%) pumps [1]. In addition to being the “second-most widely used machine in the world,” U.S. Department of Energy records show that pumping systems account for 27% to 33% of electricity used in the industrial sector [2]. Centrifugal and rotary pump designs are commonly used to transfer water below 10.34 bar (150psig), while reciprocating pumps are designed to withstand water pressures as high as 482.63 bar (7000 psig). Diaphragm pumps also transfer water but the technology is geared toward thicker, high-viscosity fluids such as paste, paint, syrup, oil sludge, or even pulp and paper slurries. These applications are generally too severe for the other pump technologies and left to diaphragm pumps in these manufacturing processes and their industrial plants [3].

AODD Pump: Air-operated double-diaphragm (AODD) pumps are especially well-suited for manufacturing processes and their ingredient transfer systems. These diaphragm pumps feature nominal displacement capacity from 189 to

757 lpm (50-200 gpm) at nearly 97% volumetric efficiency. While the other pump technologies are driven by electric motors, AODD pumps use compressed air to power the reciprocating chambers of the pump [4]. Their consumption of compressed air is why AODD pumps have traditionally been identified as a non-efficient pumping method.

Compressed Air: Nearly all industrial facilities generate and consume compressed air. The U.S. Department of Energy estimates that 10% of the electricity consumed in an industrial facility is used to generate compressed air, which is not very efficient. The overall efficiency of a compressed-air system is 10%-15%, so it takes seven or eight electrical horsepower to operate a one-horsepower air motor [5]. Normally considered the most expensive utility in the factory, 1000 standard cubic feet of air is produced at a cost of \$0.15 -0.30. Consumption of compressed air is measured in normal cubic meters per hour (Nm<sup>3</sup>/h) [standard cubic feet per minute (scfm)]. Data from AODD pump operation indicates consumption between 96.45 and 241.12 scNm<sup>3</sup>/h (60-150 scfm), averaging \$0.0236 per minute.

Compressed Air and AODD Pump Delivery: Operation of the AODD has two compressed air requirements; pressure to generate diaphragm force and sufficient quantity to fully extend the diaphragm within the pump chamber [6]. The force generated from air pressure is necessary to overcome the discharge pressure and complete diaphragm extension is necessary to force all of the fluid volume to be expelled from the chamber. Conventional control systems direct compressed air into the diaphragm chamber and continue to supply air until the diaphragm is completely extended [7].

This control method finishes the diaphragm extension under full air pressure. Finishing at full air pressure creates a significant problem for the diaphragm’s retraction during the reciprocating cycle. The reciprocating diaphragm must overcome full system pressure trapped behind the extended diaphragm to discharge its air and collapse the diaphragm. Some of the force generated by the reciprocating diaphragm is lost while forcing the exhaust of the trapped air; this causes a reduction in overall efficiency of the AODD pump design.

**Higher Efficiency AODD Concept:** If the trapped air were less than system pressure, overall pump efficiency would improve, due to less force lost to exhaust the air. A control system to reduce trapped air pressure was designed to block the supply of compressed air to the extending diaphragm such that the compressed air already in the chamber expands to completely extend the diaphragm. The expanding air finishes the stroke at less than system pressure. An electronically controlled air supply valve could do exactly this. Initially, the valve rapidly opens and closes to deliver a series of compressed air pulses to the AODD at the beginning of each diaphragm stroke [8]. The valve closes before the diaphragm finishes its extension [9]. Compressed air that has already entered the diaphragm chamber expands to finish the stroke at a progressively lower pressure according to Boyle's Law ( $P_1V_1 = P_2V_2$ ).

## Methodology

The purpose of this study was to conduct comparative validation testing on an air-operated diaphragm pump with standard and electronic controls. The experiments compared energy consumption of four air-operated double-diaphragm (AODD) pumps using conventional air controls with consumption using supply air valve electronic controls. Testing proceeded at ambient operating conditions while pumping water. The objectives of this study included

- Document pump performance parameters.

- Evaluate pump performance variables at various operating conditions, including flow rates and operating pressures.
- Analyze test data and conclude changes related to energy efficiency.

## Testing Protocol

A diaphragm pump test rig was designed and constructed and validated according to ANSI/HI 10.6-2010 (see Figures 1 and 2) and used to conduct trials on four randomly selected two- and three-inch nominal pump sizes from different manufacturers (identified as silver, blue, orange, and white) [10]. Specifically, Figure 1 is a graphical representation of the text requirements in ANSI/HI 10.6. AODD pump performance was controlled by conventional air controls and an electronic supply valve controller called MizAir provided by Proportion-Air LLC. Data were collected using an Onset automatic data acquisition and recording system. This equipment was used to measure and collect data on the following variables: testroom ambient air temperature, testroom ambient relative humidity, test-room barometric pressure, test-rig inlet fluid temperature, test-rig inlet fluid pressure, test-rig outlet fluid pressure, test-rig fluid flow rate, compressed-air pressure, compressed-air flow rate, compressed-air temperature, compressor energy usage, and test-rig pump speed. The pulse adaptor for pump speed failed and was replaced with an oscilloscope.

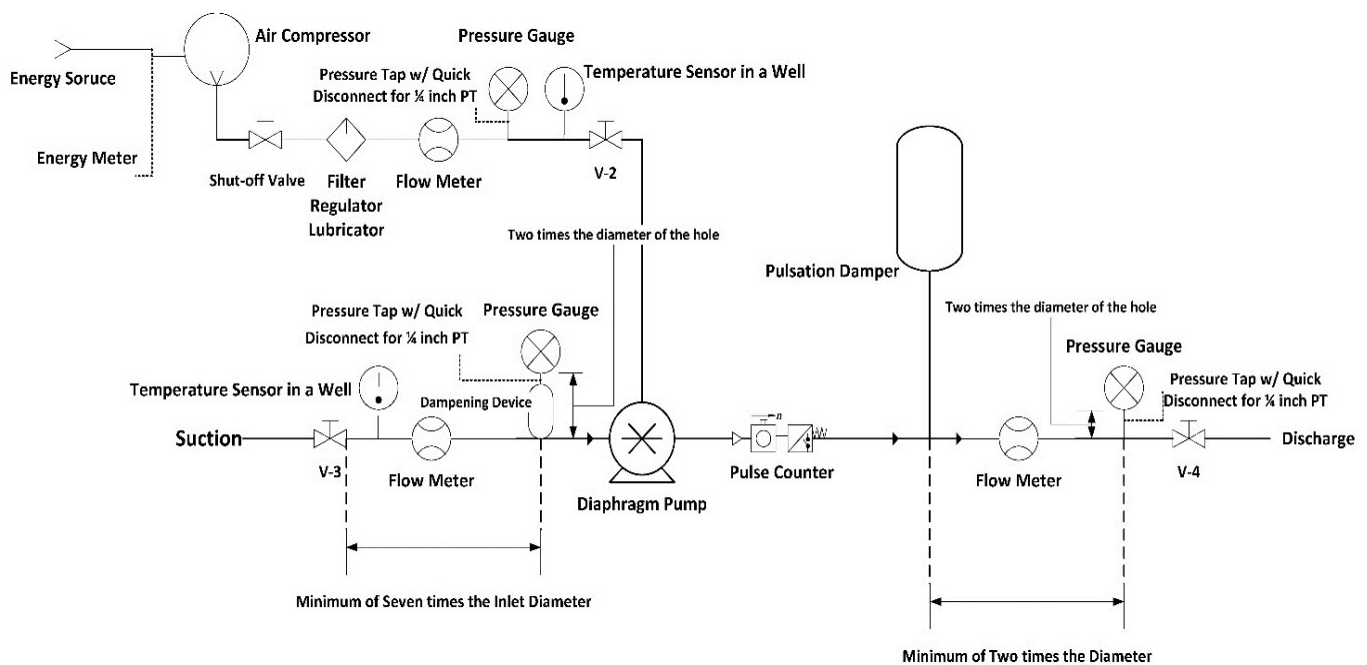


**Figure 1. ANSI/HI 10.6-2010 Test Rig Block Diagram**

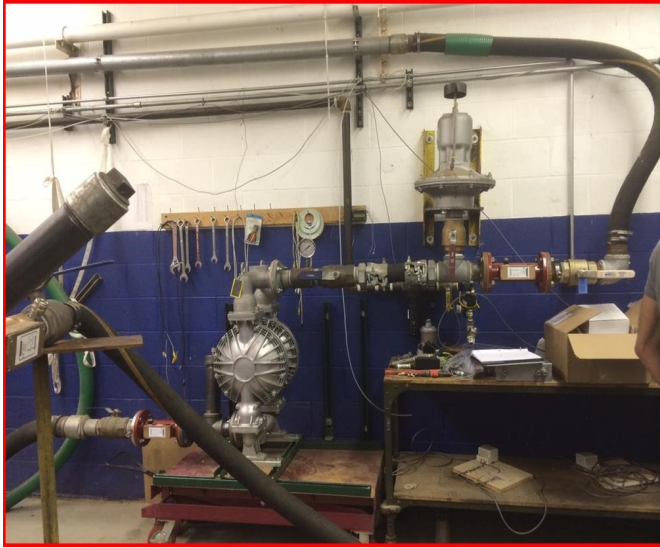


**Figure 2. ANSI/HI 10.6-2010 Test Rig Assembly**

**Method:** A two-dimensional matrix of operating conditions was established to collect data at two air supply pressures (5.52 and 6.90 bar, or 80 psig and 100 psig) and three standard pump flow rates (nominal minimum, nominal maximum, and unrestricted maximum flow rate) for each of the four pumps.

**Pump Specifications:** The four pumps (see Table 1) were randomly selected from stock and all had been successfully used on other research projects.

**Table 1. Description of the Tested Pumps**

Test No.	Pump size and Manufacturer	Model No.
# 1 Pump (Silver)	3" Yamada	DP-80BAN-HD
# 2 Pump (Blue)	3" Sandpiper	S30B1ABBANS000
# 3 Pump (White)	2" Yamada	DP-50BPS-HD
# 4 Pump (Orange)	3" Wilden	NA- Experimental*

\* The model number has not been assigned.

## Test Procedure: Testing Sequence

The initial trial was conducted with pump #1 in the standard control mode (without electronic control). Operating pressure was set to 6.90 bar (100 psig) and water flow rate to 568 lpm (150 gpm). Data were collected for 10 minutes at a sampling interval of 10 seconds (exceeding ANSI/HI 10.6-2010 data requirements) and 30 contiguous measure-

ment points were extracted for graphical analysis. Once the standard control mode trial was completed, the electronic controller was attached and tested using the same operating conditions and sampling time. The procedure was repeated for the other three pumps, resulting in 48 trials, which produced 1450 valid data files that were saved for analysis.

## Results and Analysis

Operating air pressure was analyzed using standard and electronic controls to determine what AODD pump performance factors might be affected by the different air supply control methods. Four performance factor observations were made. Data showed that AODD pumps using standard controls consumed more compressed air than pumps using the electronic control. These data also revealed that pump delivery performance was negatively affected by air pressure variation; and, as air pressure was increased, pump delivery was further reduced by its variation.

Pump #2 (see Figures 3 and 4) suffered the greatest reduction in output flow, due to electronically controlled air pressure fluctuation and so is featured in this discussion. Performance testing was conducted on pump #2 at nominal air pressures of 5.52 bar and 6.90 bar (80 psig and 100 psig) and for nominal water flows of 568, 663, and 757 lpm (150, 175, and 200 gpm). As water flow increased from 568 lpm to 757 lpm (150 gpm to 200 gpm), air pressure variation from 5.52 bar (80 psig) remained at 0.069 bar (1 psig) using standard control, but rose from 0.207 to 0.345 bar (3 to 5 psig) with electronic control. Comparison of data from Figures 3 and 4 revealed that, as flow increased, flow fluctuation grew in variation with either control but was of higher magnitude with electronic control. Similar increases with air pressure and water flow variations occurred when the supply pressure was raised to 6.90 bar (100 psig).

Variances in water flow rates were similarly observed with standard and electronic controls. Figures 3 and 4 show that the water flow rate for pump #2 was generally lower with electronic control but was often equal to or higher than under standard control. Additionally, the magnitude of variation in water flow rate for standard and electronic controls was not significantly different. An analysis of 1450 data files was conducted on the four pumps to determine the net effect of higher air pressure variation of the electronic control on pump delivery. A paired two-sample means hypothesis test determined that there was a difference in pump delivery using standard and electronic controls (see Table 2). The null hypothesis,  $H_0$ , states that there is no difference between the pump deliveries, and the alternative hypothesis,  $H_a$ , states that the electronic control pump delivery is less than delivery using standard controls.

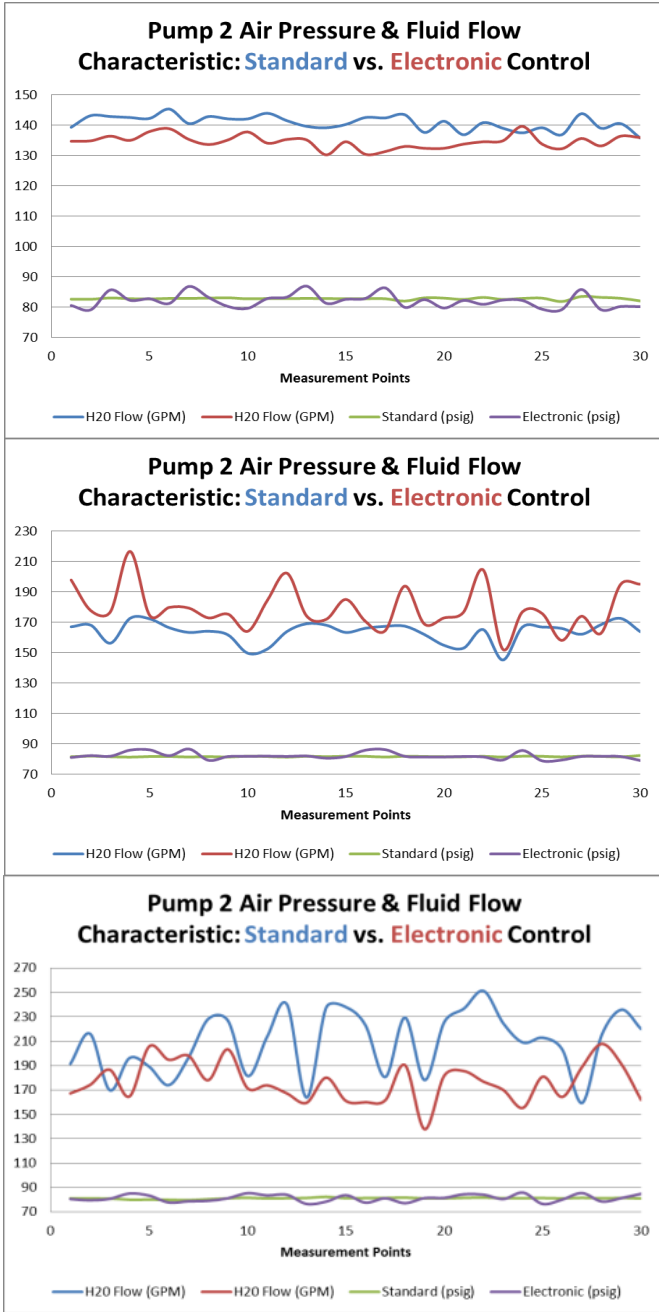


**Figure 3. 5.52 bar (80 psig) Air Pressure and Flow with and without Electronic Control**

Using 5.52 bar (80 psig) nominal air pressure, the resultant t-stat of 3.318 and a one-tail p-value of 0.00048 concluded that electronic control pump delivery is less than delivery using standard controls. A 95% confidence interval calculates that the electronic control results in 6.541 to 25.510 lpm (1.728 to 6.739 gpm) lower mean pump delivery than standard controls. Applying the same test at 6.90

bar (100 psig) nominal air pressure, the resultant t-stat of 8.0548 and a one-tail p-value of  $1.611 \times 10^{-15}$  concludes that electronic control pump delivery is less than delivery using standard controls. A 95% confidence interval calculates that the electronic control results in 23.651 to 38.891 lpm (6.248 to 10.274 gpm) lower mean pump delivery than standard controls.

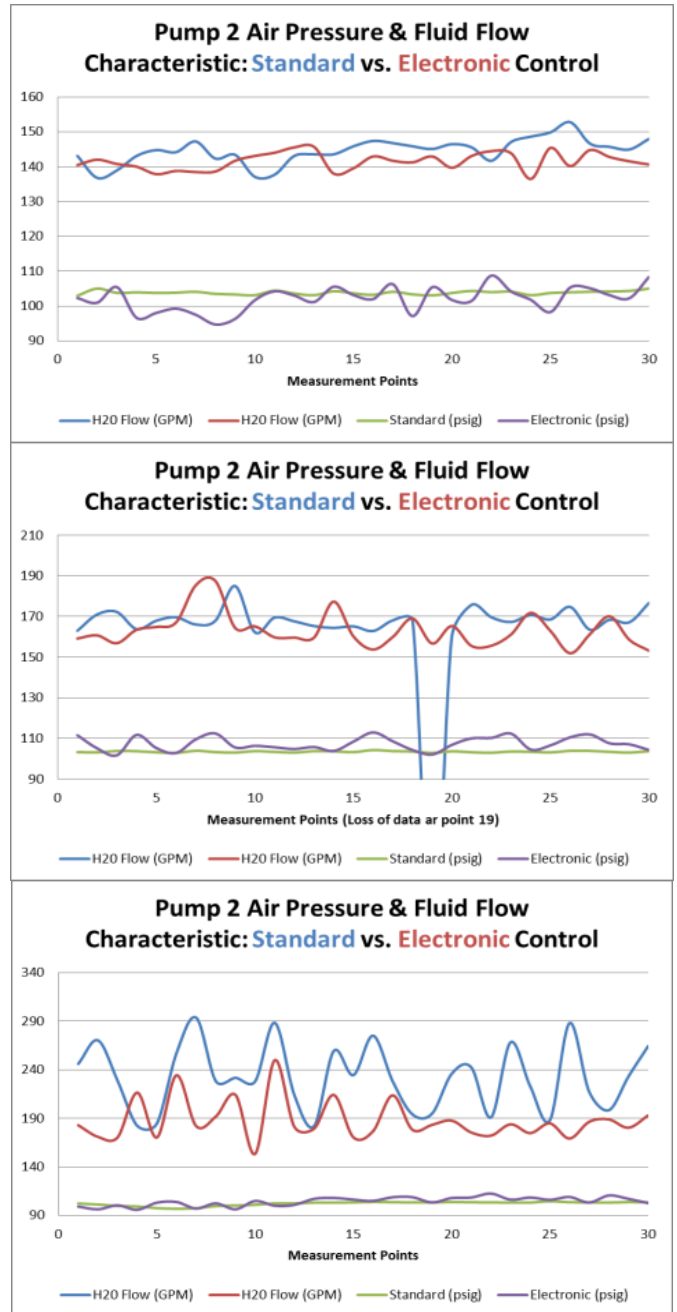


**Figure 4. 6.90 bar (100 psig) Air Pressure and Flow with and without Electronic Control**

**Table 2. Pump #2 Fluctuation of Air Pressure with and without Electronic Control**

	5.52 bar_757 lpm (80 psig – 200 gpm)		5.52 bar_663 lpm (80 psig – 175 gpm)		5.52 bar_568 lpm (80 psig – 150 gpm)	
	w/o Electronic	With Electronic	w/o Electronic	With Electronic	w/o Electronic	With Electronic
Max.	1.21%	5.05%	0.87%	5.35%	1.13%	6.04%
Min.	-0.52%	-6.41%	-0.50%	-4.14%	-1.30%	-3.68%
	6.90 bar_757 lpm (100 psig – 200 gpm)		6.90 bar_663 lpm (100 psig – 175 gpm)		6.90 bar_568 lpm (100 psig – 150 gpm)	
	w/o Electronic	With Electronic	w/o Electronic	With Electronic	w/o Electronic	With Electronic
Max.	1.25%	5.93%	0.88%	6.31%	1.15%	5.04%
Min.	-1.02%	-7.79%	-0.58%	-7.99%	-0.77%	-6.19%

Another paired two-sample means hypothesis test was employed to determine the differences in AODD pump compressed air consumption using standard and electronic controls. Air consumption for each pump was plotted (see Figures 5 and 6).

The null hypothesis,  $H_0$ , states that there is no difference between the air consumption, and the alternative hypothesis,  $H_a$ , states that the electronic control air consumption is less than standard controls. Using nominal 5.52 bar (80 psig), the resultant t-stat of 71.85 and a one-tail p-value of zero concluded that electronic control air consumption is less than standard controls. A 95% confidence interval calculates that the electronic control results in 49.48 to 52.40 Nm<sup>3</sup>/h (30.862 to 32.597 scfm) lower mean air consumption than standard controls. With respect to Figure 6, applying the same test at nominal 6.90 bar (100 psig), the resultant t-stat of 72.30 and a one-tail p-value of zero concluded that electronic control air consumption is less than standard controls. A 95% confidence interval calculates that the electronic control results in 67.02 to 70.76 Nm<sup>3</sup>/h (41.694 to 44.0212 scfm) lower mean air consumption than standard controls.

The energy reduction offered by electronic controls can be converted to kilowatts by applying the energy required to compress 1.00 Nm<sup>3</sup>/h (0.62 scfm) of air (single-stage compression) at 5.52 bar (80 psig) = 0.0844 kW or 6.90 bar (100psig) = 0.0961 kW [11]. Equation (1) calculates the energy savings for the average mean air consumption savings attributed to the electronic controller. Table 3 shows that the air saving percentage using the electronic controller goes up as the fluid flow rate through the pump increases. Although supply air pressure and current fluid flow rate can be used to predict air saving percentage for the test pumps,

other comparisons were also studied to generalize for all pumps. Comparisons and regression analysis included fluid flow rate by individual pump, fluid flow rate by all pumps, fluid flow by pressure, and fluid flow by pressure and capacity. These results revealed that the slopes of air consumption savings, with respect to fluid flow rates, decline as capacity increases, and that an air savings chart is not possible, due to non-linearity between pumps.

$$kW \text{ Saving} = \tag{1}$$

$$\text{Saving} \times \text{kW required to compress } 1.00 \text{ Nm}^3/\text{h} \text{ at } 6.90 \text{ bar}$$

$$= 68.89 \text{ Nm}^3/\text{h} \times 0.0961 \frac{\text{kW}}{\text{Nm}^3/\text{h}} = 6.62 \text{ kW}$$

## Conclusions

In all trials and at all set points, the electronic controller reduced diaphragm pump air consumption. The air consumption reductions varied by pump, but the electronic controller reduced the AODD mean air consumption by 19.9% to 47.8%. The air supply pressure was varied to 5.52 bar (80 psig) and 6.90 bar (100 psig), while adjusting pump fluid flow rates to three nominal rates, including max flow rate. Figure 7 depicts a linear relationship between air consumption and water flow when the air pressure is 5.52 bar (80 psig) and 6.90 bar (100 psig) for capacities above and below 568 lpm (150 gpm), respectively. Therefore, the graphed data can predict the percentage of air consumption savings for new pumps or existing pumps when the fluid flow rate is known.



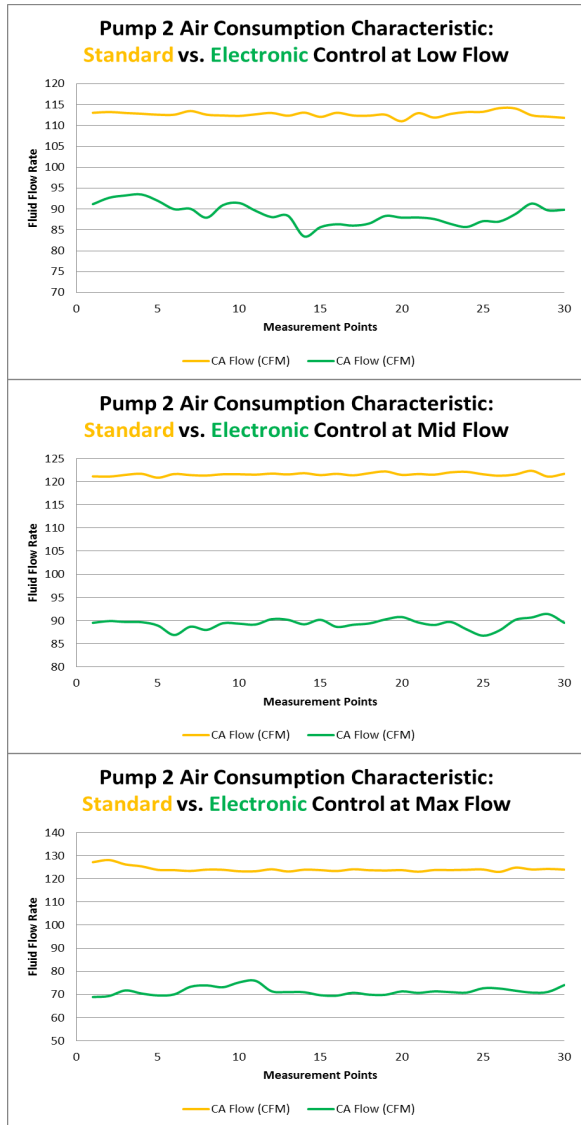


Figure 5. 5.52 bar (80 psig) Air Consumption with and without Electronic Control

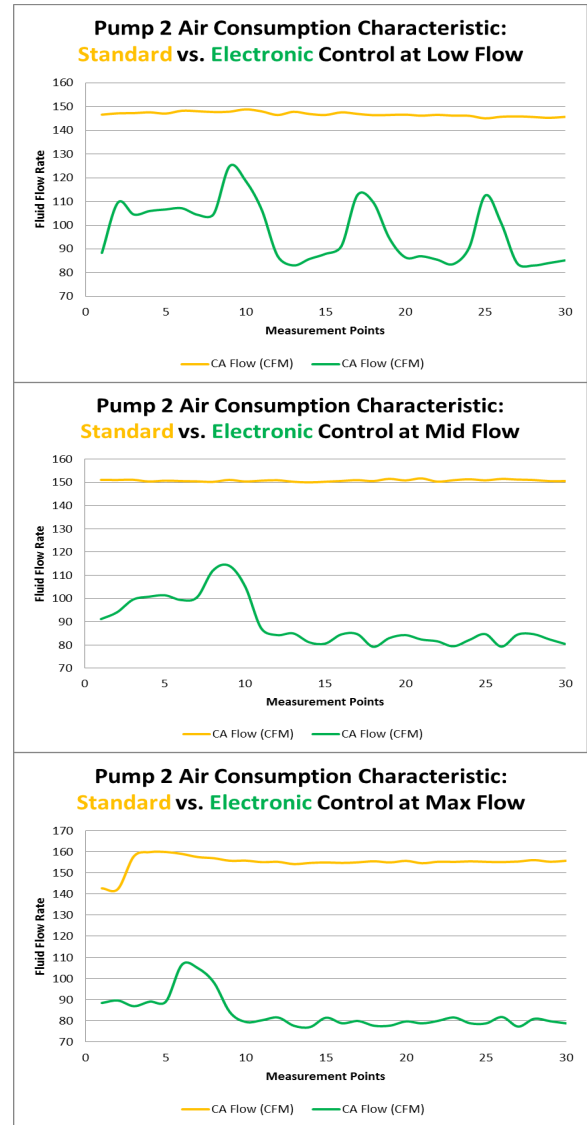


Figure 6. 6.90 bar (100 psig) Air Consumption with and without Electronic Control

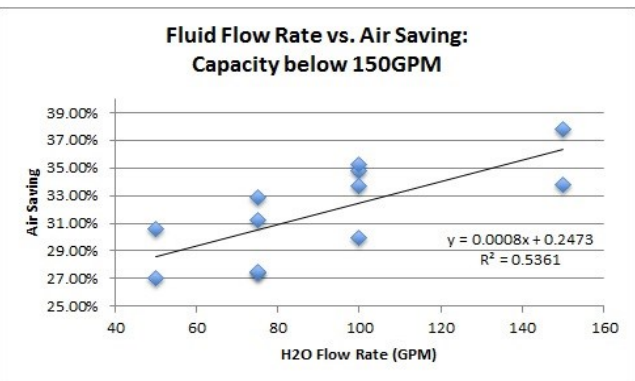
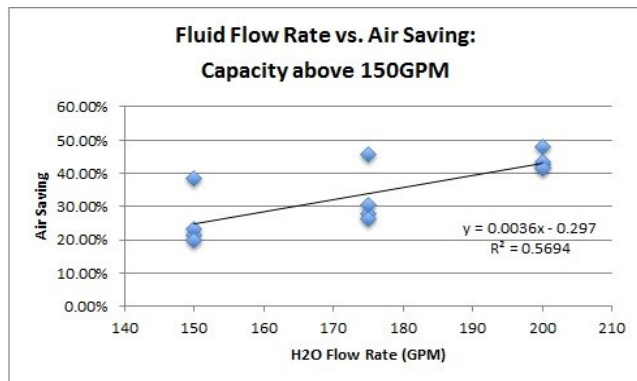


Figure 7. Fluid Flow Rate versus Air Consumption Savings above and below 568 lpm

**Table 3. Consolidated Air Consumption Savings by Pump and Supply Pressure**

Air Pressure	Pump #1		Pump #2	
	H2O Flow Rate in LPM (gpm)	Air Saving	H2O Flow Rate in LPM (gpm)	Air Saving
6.90 bar (100 psig)	568 (150)	33.80%	757 (200)	47.80%
	379 (100)	30.00%	662 (175)	45.60%
	284 (75)	27.40%	568 (150)	38.60%
5.52 bar (80 psig)	568 (150)	37.80%	757 (200)	42.70%
	379 (100)	34.80%	662 (175)	27.90%
	284 (75)	27.50%	568 (150)	21.20%
Air Pressure	Pump #3		Pump #4	
	H2O Flow Rate in LPM (gpm)	Air Saving	H2O Flow Rate in LPM (gpm)	Air Saving
6.90 bar (100 psig)	379 (100)	33.70%	757 (200)	43.60%
	283 (75)	32.90%	662 (175)	26.20%
	189 (50)	30.60%	568 (150)	23.20%
5.52 bar (80 psig)	379 (100)	35.20%	757 (200)	41.70%
	283 (75)	31.20%	662 (175)	30.30%
	189 (50)	27.00%	568 (150)	19.90%

## Acknowledgments

This work was supported in part by the U.S. Department of Energy under grant number DE-FOA-0000490.

## References

- [1] Reidy, R. (2006). *Profile of the International Pump Industry. Market Prospects to 2010*. (6<sup>th</sup> ed.). Elsevier Science.
- [2] Glauber, C. (2013). AODD Pumps Improve Production & Energy Efficiency. Retrieved from <http://www.dovercorporation.com/globalnavigation/our-markets/fluids/aodd-pumps-improve-production--energy-efficiency>
- [3] Fluid Transfer Using All-Flo Double Diaphragm Pumps. (n.d.). Retrieved from <http://www.all-flo.com/applications/fluid-transfers.html>
- [4] Graco Technical Communications Department Module No. 321-048. (1996). Double Diaphragm Pumps. Retrieved from [file.seekpart.com/keywordpdf/2011/5/20/201152023540480.pdf](http://www.all-flo.com/applications/fluid-transfers.html)
- [5] U. S. Department of Energy. (2000.) *Determine the Cost of Compressed Air for Your Plant* (DOE/GO-102000-0986). Retrieved from [http://www.energystar.gov/ia/business/industry/compressed\\_air1.pdf](http://www.energystar.gov/ia/business/industry/compressed_air1.pdf)
- [6] The Working Principle of a Verderair Double Diaphragm Pump. (n.d.). Retrieved from <http://www.verderair.com/diaphragm-pump-technology>
- [7] Orr, D. R. (2008). Air Operated Double Diaphragm Pumps. Retrieved from <http://www.pumpsandsystems.com/topics/pumps/pumps/air-operated-double-diaphragm-pumps>
- [8] Proportion Air. (n.d.). Retrieved from <http://www.proportionair.com/literature/brochures/MizAir-Brochure.pdf>
- [9] MizAir Installation Guide. (n.d.). Retrieved from <http://www.proportionair.com/literature/installation-guides/MizAir-Installation.pdf>

- 
- [10] American National Standards Institute. (2010), ANSI/HI 10.6-2010 Air-Operated Pump Tests.
- [11] Amiss, J. M. (2004). Machinery's Handbook Guide 27. Industrial Press Inc.

## Biographies

**DAVID W. GOODMAN** is an assistant professor of engineering technology at Indiana University-Purdue University Indianapolis. He earned his BS degree in electrical engineering from Purdue University; MS degree (Mechanical Engineering Technology, 2005) from Purdue University; and, PhD (Engineering Technology, 2009) from Purdue University. His interests include energy efficiency, sustainability, and renewable energy systems. Dr. Goodman may be reached at [dwgoodma@iupui.edu](mailto:dwgoodma@iupui.edu)

**ROBERT J. DURKIN** is a lecturer of engineering technology at Indiana University-Purdue University Indianapolis. He earned his BS degree in electrical engineering from Indiana Institute of Technology and MBA from the University of Notre Dame. Mr. Durkin has over twenty-five years' of industry experience and is currently teaching at Indiana University-Purdue University Indianapolis. His interests include fluid power, control systems, and manufacturing. Mr. Durkin may be reached at [rjdurkin@iupui.edu](mailto:rjdurkin@iupui.edu)

# A STUDY OF FLASH ATOMIZATION IN A PRESSURE SWIRL NOZZLE

Mebougna L. Drabo, Alabama A&M University; Narinder K. Tutu, Brookhaven National Laboratory; Thomas Butcher, Brookhaven National Laboratory; Rebecca Trojanowski, Brookhaven National Laboratory

## Abstract

Due to the emphasis on energy conservation in residential buildings, there is a need for the development of low firing-rate, load-modulating residential oil burners. The excessive on/off cycling of current fixed firing-rate residential oil burners leads to an overall reduction in the energy efficiency of the heating system and an increase in environmental pollution. It also results in frequent plugging of the spray nozzles. In this study, the authors investigated the use of flash atomization to achieve the objective of developing such a low firing rate fuel nozzle that can maintain its atomization quality, while the fuel firing rate is changed by altering one or more control parameters. In this article, the authors report on the first experimental atomization performance results obtained from a pressure swirl nozzle, as a function of fuel temperature (up to the flashing conditions), using water as a fuel simulant.

## Introduction

Due to the emphasis on energy conservation in residential buildings, there is a need for the development of low firing-rate, load-modulating residential oil burners. There are two reasons for this. First, because of new energy-efficient design requirements, heating requirements for new construction are significantly lower than for old residential buildings. Thus, a lower firing rate-boiler is sufficient for fulfilling peak demand. This is especially true for smaller homes. Secondly, because the heating requirements during a given day continuously change with time due to changing weather conditions and demand from occupants, a conventional residential boiler must cycle (on/off) many times during a day. During the starting phase, the combustion efficiency of oil burners is much lower than during steady-state operation; consequently, the level of pollutants emitted is higher. Therefore, excessive on/off cycling leads to an overall reduction in energy efficiency of the heating system and an increase in the environmental pollution contribution. Furthermore, it also results in larger temperature swings within the house. A low firing-rate, load-modulating oil burner not only provides more thermal comfort for the occupants, it also results in lower fuel costs and a reduction in pollutants emitted. Excessive on/off burner cycling also leads to frequent plugging of the swirl nozzles.

Standard pressure swirl nozzles are designed for a constant oil firing rate. If one attempts to lower the oil firing rate by reducing the pump supply pressure, the resulting atomization is poor (larger fuel droplets), leading to poor combustion. Bypass pressure swirl nozzles, such as those from Delevan, do allow operation at lower firing rates, but the minimum oil firing rate for which the fuel atomization quality is still acceptable is still not small enough (smaller than 0.25 gallons per hour). In order to circumvent this problem, the authors of this current study investigated using flash atomization to achieve the objective of developing a low firing-rate fuel nozzle that will maintain its atomization quality, while the fuel firing rate is changed by altering one or more of the control parameters. Flash atomization or, more descriptively flash-boiling atomization, occurs when a heated liquid at high pressure (but still locally subcooled) is injected into a lower pressure combustion chamber in which the pressure is lower than the saturation pressure of the liquid. Thus, when the liquid jet enters the combustion chamber, it is locally in a superheated state; this results in the boiling of a small fraction of the liquid. The bursting vapor bubbles lead to very fine atomization of the liquid. In practice, to improve the quality of atomization, the flash atomizers are designed to undergo flashing (boiling) before discharge into the combustion chamber. Under these conditions, the nozzle exit discharges a two-phase bubbly mixture.

Extensive publications on the subject of flash atomization are available in the literature [1, 2]. Sher et al. [3] gave a review of the technical basis for flash atomization. Kamoun et al. [4] gave additional design guidelines for flash atomization nozzles, who also provide dimensionless correlations (in terms of the Weber and Jacob numbers) for the onset of bubble nucleation and a fully developed atomization regime. The Brown and York study [5] concluded that high pressures and velocities are not required for the flash atomization process. However, superheating was necessary. Brown and York found that mean drop sizes nominally decrease with an increase in jet Weber number at a given temperature at the same bubble growth rate. Work by Oza and Sinnamon [6] revealed that external flashing occurs at a lower degree of superheat, where the jet is intact when leaving the nozzle and rapidly breaks, due to rapid bubble growth. Oza [7] explored the mechanisms responsible for flash boiling and showed spray images of propane, metha-

nol, and indolene fuel injection through an electromagnetic injector. He recognized two regimes of flash-boiling injection: 1) flashing with an essentially constant spray-cone angle and 2) flashing with an external expansion. Park and Lee [8] investigated the flash atomization mechanism and provided an excellent description of it [8]. Here, the authors report on the first experimental atomization performance results obtained from a pressure swirl nozzle as a function of fuel temperature (up to the flashing conditions), using water as a fuel simulant. Spray nozzle manufacturers routinely use water to characterize the droplet size distribution from their nozzles [9, 10].

## Experimental Setup

Figure 1 shows a schematic layout of the spray nozzle setup. The nitrogen gas pressure in the liquid tank was set at 100 psig during the experiments. A variac was used to control the heater power. The temperature of the water entering the spray nozzle was regulated by a temperature controller. The spray nozzle used in this experiment was a Delevan 0.4 GPH 60° DOF swirl nozzle (see Figure 2). The liquid tank sat on a digital balance. The actual fuel firing rate during the experiment was measured by monitoring the indicated weight on the scale as a function of time.

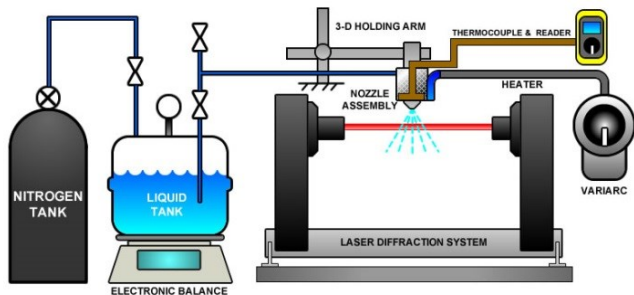


Figure 1. Schematic Layout of the Spray System

A Malvern Spraytec System from Malvern Instruments Ltd. was used to measure the droplet size distribution within the liquid spray at various liquid temperatures. This system has a particle detection range of 0.1  $\mu\text{m}$  to 900  $\mu\text{m}$ . This instrument used the laser diffraction pattern from the droplet spray and Mie theory [11] to compute the particle size distribution in the measurement zone. It consisted of two main modules (transmitter and receiver), PC, and the associated software. The spray to be measured was located in-between the transmitter and receiver modules. The transmitter outputted a 10-mm diameter, 5 mW helium-neon collimated laser beam. The receiver module consisted of the collecting optics, an array of detectors at the focal plane of the collecting lens, and associated control and analysis electronics.

Figure 3 shows a schematic of the optical setup of the instrument. For clarity, only two scattered light rays are shown and the detector array is at the focal plane of the lens.

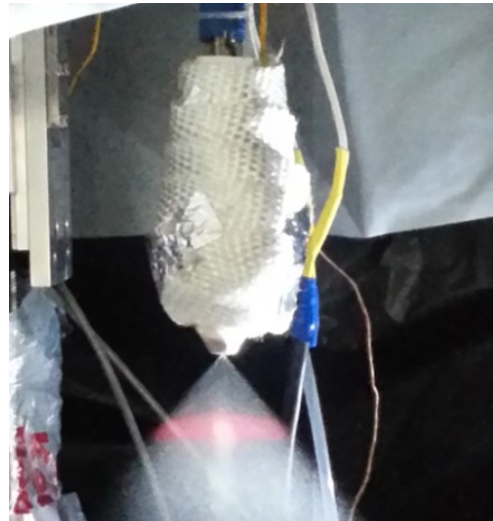


Figure 2. A Close-up of the Water Spray in the Malvern Laser Beam during the Experiments

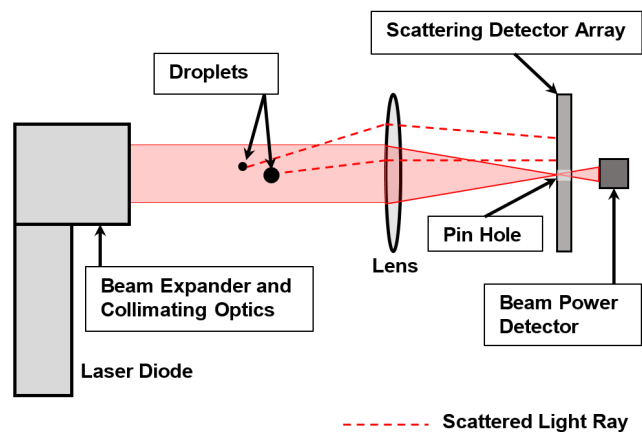


Figure 3. Schematic of the Optical Setup of the Malvern Spraytec System [not to scale]

## Results and Discussion

A Delevan 0.4 GPH 60° DOF swirl nozzle performed droplet size distribution measurements, with distilled water was used as the fuel simulant. The water was supplied to the heated and insulated nozzle holder at 100 psig. Its temperature was varied from room temperature to 151°C. The measured Sauter mean diameter  $D[3,2]$  and the volume moment mean diameter,  $D[4,3]$  are shown in Figure 4 as a function of the nozzle temperature. While both mean diameters decreased with increasing temperature, there was a sharp re-



duction in the Sauter mean diameter at 143°C. This indicated a significant droplet size reduction due to flash atomization. Also, there was a significant reduction in the water flow rate as the temperature increased. This was due to the reduction in the dynamic viscosity of the water with increasing temperature.

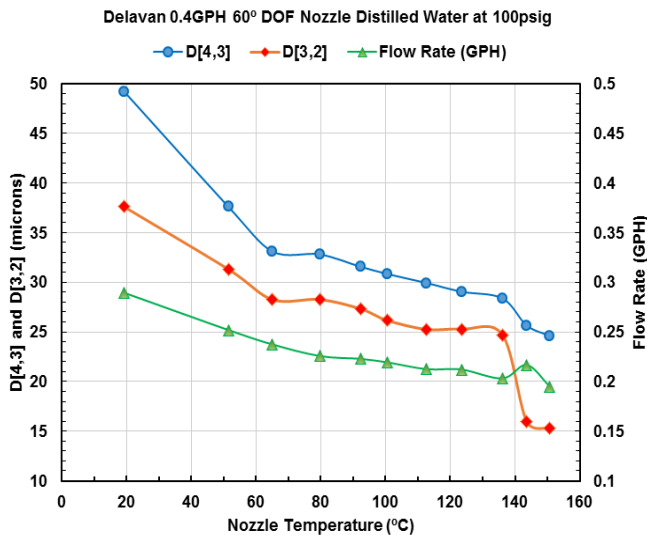


**Figure 4. Droplet Mean Diameters and Nozzle Flow Rate as a Function of Nozzle Temperature**

Figures 5-7 are photographs of the spray pattern during the experiment. Figure 5 shows the spray picture at room temperature. The spray behavior shows a gradual change with increasing temperature up to roughly the boiling point of water (see Figure 6). When the temperature was increased above the boiling point (see Figure 7), the spray pattern showed a sharp change.

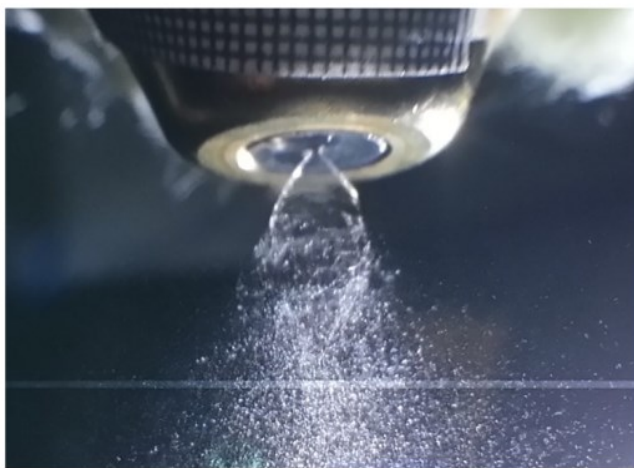


**Figure 5. Spray Picture at a Temperature of 19.3°C**

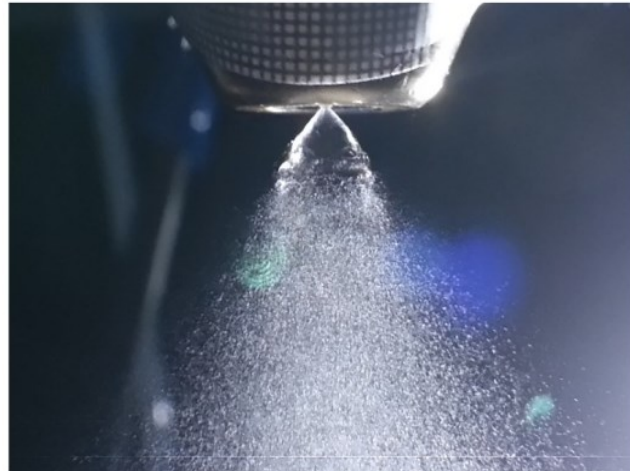


**Figure 6. Spray Picture at a Temperature of 92.2°C**

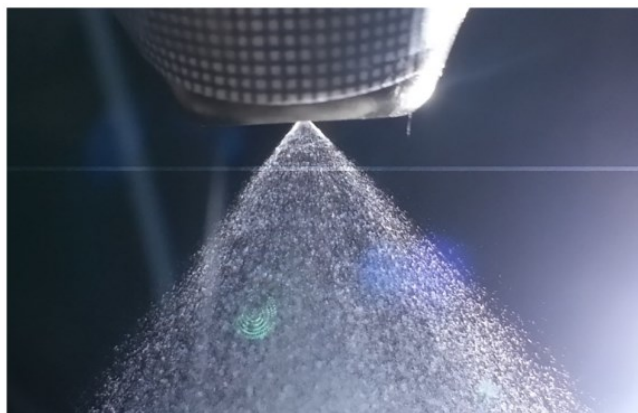


**Figure 7. Spray Picture at a Temperature of 136.1°C**

While mean diameters are important, they do not show a complete picture of the particle size distribution within the spray. Figure 8 shows an evolution of the droplet size distribution histogram as a function of nozzle temperature. Shifting of the peak towards smaller size and a narrowing of the distribution was clearly observed. Also observed was a secondary peak at 2 μm at 151°C. It is not clear if this peak was due to smaller droplets being generated as result of flash atomization or to the condensation of flashed steam.

## Conclusions and Future Work

These preliminary results clearly demonstrate significant improvement in atomization at elevated fuel temperatures. However, one of the key findings of this study was that flash atomization by itself cannot reduce the fuel firing rate (see Figure 4) to a level needed for a practical load modulating oil burner (say, a turn-down ratio of 3:1 or 4:1). Bypass nozzles allow significant reduction in fuel firing rate; how-

ever, at low flow rates, there is a large increase in droplet size distribution. Therefore, the use of a variable flow bypass nozzle in combination with flash atomization should prove to be an effective solution for developing a load-modulating, low firing-rate oil burner. Future work by the authors will explore this option.

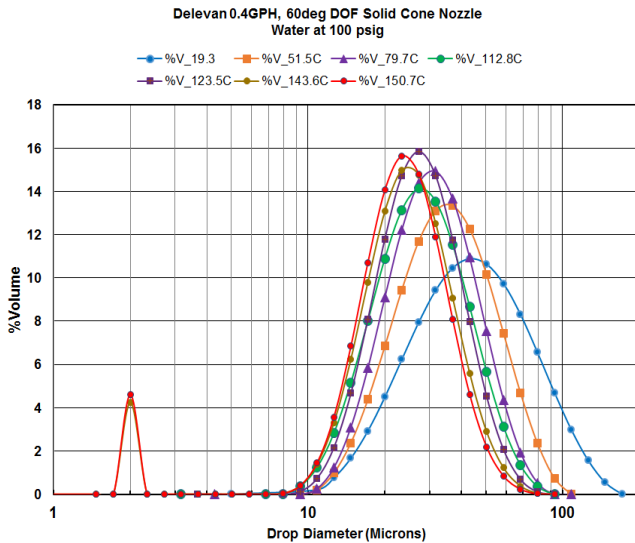


**Figure 8. Evolution of Droplet Size Distribution Histogram as a Function of Nozzle Temperature**

## Acknowledgments

The first author gratefully acknowledges the support of the U.S. Department of Energy, Office of Science, and Office of Workforce Development for Teachers and Scientists (WDTS). This project was also supported in part by the National Oilheat Research Alliance (NORA). The authors would like to thank Mr. Yusuf Celebi and Mr. George Wei for their assistance in the laboratory throughout this project.

## References

- [1] Ju, D., Fang, J., Zhang, T., Qiao, X., Xiao, J., & Huang, Z. (2015). High-speed shadow imaging in internal flow pattern and macroscopic characteristics of an R134a flash-boiling spray discharged through a vertical twin-orifice atomizer. *International Journal of Multiphase Flow*, 75, 224-236.
- [2] Breton, K., Fleck, B. A., & Nobes, D. S. (2013). A Parametric Study of a Flash Atomized Water Jet Using a phase Doppler Particle Analyzer. *Atomization and Sprays*, 23(9).
- [3] Sher, E., Bar-Kohany, T., & Rashkovan, A. (2008). Flash-Boiling Atomization. *Progress in Energy and Combustion Science*, 34(4), 417-439.

- [4] Kamoun, H., Lamanna, G., & Weigand, B. (2010). High-Speed Shadowgraphy Investigations of Superheated Liquid Jet Atomization. *ILASS-Americas 22nd Annual Conference on Liquid Atomization and Spray*. Zustems, Cincinnati, OH.
- [5] Brown, R., & York J. L. (1962). Sprays formed by flashing liquid jets. *A.I.Ch.E. Journal*, 8(2) 149–153.
- [6] Oza, R. D., & Sinnamon, J. F. (1983). An Experimental and Analytical Study of Flash-Boiling Fuel Injection. *SAE Technical paper 830590*, doi:10.4271/830590.
- [7] Oza, R. D. (1984). On the mechanism of flashing injection of initially subcooled fuels. *Journal of Fluids Engineering*, 106(1), 105–109.
- [8] Park, B. S., & Lee, S. Y. (1994). An experimental investigation of the flash atomization, mechanism. *Atomization Sprays*, 4(2), 159–179.
- [9] Law, D., Shepard, T., & Strykowski, P. (2014). Numerical Simulations of Near-Nozzle Exit Characteristics for an Effervescent Atomizer at Low Gas to Liquid Mass Flow Ratio. In *ASME 2014 4<sup>th</sup> Joint US-European Fluids Engineering Division Summer Meeting collocated with the ASME 2014 12<sup>th</sup> International Conference on Nanochannels, Microchannels, and Minichannels* (pp. V01CT23A008-V01CT23A008). American Society of Mechanical Engineers.
- [10] Shemirani, F. M., Church, T. K., Lewis, D. A., Finlay, W. H., & Vehring, R. (2015). Onset of Flash Atomization in Propellant Microject. *ASME Journal of Fluids Engineering*, 137(9), 091101-9.
- [11] Hergert, W., & Wriedt, T. (2012). *The Mie Theory*. Springer Series in Optical Sciences 169, DOI: 10.1007/978-3-642-28738-1\_2.

## Biographies

**MEBOUGNA L. DRABO** is an assistant professor of mechanical engineering at Alabama A&M University. His research interests include flash atomization, laser diagnostics in IC engines, IDLTS, alternative fuels, and advanced combustion IC engine concepts. Dr. Drabo may be reached at [mebougna.drabo@aamu.edu](mailto:mebougna.drabo@aamu.edu)

**NARINDER K. TUTU** is currently a guest scientist at the Brookhaven National Laboratory (BNL), who retired from the BNL after about 27 years of research. His areas of interest include: a) instrumentation in the fields of fluid dynamics, multiphase flows, and heat transfer; b) two-phase flow and transient heat transfer in porous media; c) safety studies of severe nuclear reactor accident scenarios; and, d) energy conservation in buildings. Tutu can be reached at [tutu@bnl.gov](mailto:tutu@bnl.gov)

---

**THOMAS BUTCHER** is the deputy chair of the Sustainable Energy Technologies Department and leader of the Energy Conversion Group. Work within this group includes liquid fuel combustion and oil-fired heating system efficiency, biofuels applications, polymer composite heat exchangers, solar thermal systems, micro-combined heat and power concepts, absorption heat pumps, wood boiler emissions and efficiency, and advanced materials for geothermal energy applications. Dr. Butcher may be reached at [butcher@bnl.gov](mailto:butcher@bnl.gov)

**REBECCA TROJANOWSKI** received her BS in Chemical Engineering and M.S. in Mechanical Engineering from Worcester Polytechnic Institute and is now currently working towards her EngScD at Columbia University in the Earth and Environmental Engineering Department. She is an associate staff engineer in the Energy Conversion Group at Brookhaven National Laboratory. Her interests focus primarily on technical solutions to advance building energy systems, fossil fuel reduction, and emissions. Some of her research and development areas include advanced HVAC concepts, biofuels, solid fuels, air pollution, and combustion and system concepts. Rebecca may be reached at [rtrojanowski@bnl.gov](mailto:rtrojanowski@bnl.gov)

# THEORETICAL PREDICTION AND EXPERIMENTAL VALIDATION OF YOUNG'S MODULUS FOR ENGINEERING MATERIALS

Yaomin Dong, Kettering University

## Abstract

The modulus of elasticity is one of the most important material properties in mechanical design and analysis. Material properties change at elevated temperatures. The modulus-temperature relationship is traditionally determined experimentally, and the procedure is time-consuming, expensive, and often impossible. The main goal of this study was to develop a theoretical relationship between the modulus of elasticity and temperature, based on the kinetic nature of the strength of solids and a nonlinear equation of state for materials. Such a modulus-temperature relationship was then compared with existing experimental data. The validation results showed good correlations between theory and experiment and demonstrated the potential to theoretically predict the modulus of elasticity of different engineering materials as a function of temperature.

## Introduction

Engineering materials deform under various loads in a structure. Engineers need to perform detailed engineering analyses when designing the structure in order to meet product specifications. Material response is a function of applied load, temperature, time, and other conditions. Material scientists investigate these mechanical properties by testing materials using standard procedures such as those published by the American Society for Testing and Materials (ASTM).

Temperature-dependent material properties are very important for applications in an environment with changing temperatures. In metal forming and machining processes, for instance, the workpiece temperature changes significantly, due to tool-workpiece interfacial friction and deformation. Such a process is typically transient; that is, the temperature distribution inside the material is a function of time and location. In a finite element analysis (FEA), this would require an analyst to input material properties in the form of tabulated data for different temperatures. These material data are often experimental, difficult to obtain, prone to error, and tedious to input. Because the experimental data are scattered, some approximations are necessary to smooth the data.

This introduces errors and often causes difficulties in achieving a converged solution in a numerical analysis. One of the most important mechanical properties, the modulus of elasticity or Young's modulus, is sensitive to both temperature and rate of loading; i.e., the stress or strain rate. The modulus-temperature relationships  $E(T)$  of different engineering materials are always determined experimentally. Engineers and scientists need to perform time-consuming and costly experiments to determine the modulus of elasticity of the materials for specific temperature ranges based upon their own project needs. A well-validated theoretical model for predicting the modulus of elasticity of engineering materials within certain temperature ranges would be a valuable alternative to the traditional time-consuming, expensive, and very often impossible empirical methods. The establishment of such a relationship between the modulus of elasticity and temperature for engineering materials would help engineers and designers in their product design and development.

The objective of this study was to establish a comprehensive theoretical model for predicting the relationship between modulus of elasticity and temperature for a wide spectrum of engineering materials, and validate the theory with experimental data in published studies.

## Theoretical Model

The theoretical modulus of elasticity-temperature relationship is based on the nonlinear stress-strain relationship for industrial materials and the kinetic nature of the strength of solids [1,2]. As Equation (1) shows, this relationship follows from the diatomic model of a solid body [3,4], which shows the nonlinear approximation of the potential energy of two atoms as a function of the distance between them:

$$U(r) \approx \frac{1}{2}\beta(r-r_o)^2 - \frac{1}{3}g(r-r_o)^3 \quad (1)$$

where,  $\beta$  is the coefficient of linear elasticity;  $g$  is the anharmonic coefficient;  $r_o$  is the distance between atoms at the equilibrium position; and,  $r$  is the instantaneous distance between two atoms.

If the potential energy of two atoms is a parabola, then the interaction force between the atoms,  $F$ , is proportional to the displacement from equilibrium,  $r-r_0$ :

$$F = dU/dr = \beta(r-r_0), \text{ or } F/r_0^2 = E_0(r-r_0)/r_0$$

where,  $E_0 = (\beta/r_0)$  is the modulus of elasticity.

It is important to point out that in this case the atoms oscillate harmonically, the values of energy at negative and positive displacement are equal, and the distance between atoms does not change with temperature.

The cubic term in Equation (1) leads to asymmetry of the potential energy. In comparison with parabolic potential, the curve of potential energy is flatter at positive displacements and steeper at negative displacements. The resulting decrease in potential energy for positive displacement leads to expansion of the material, a shift of the center of anharmonic thermal oscillations, and softening of the mechanical properties of the solid. In particular, the modulus of elasticity decreases linearly with linear thermal expansion [3, 4], as shown in Equation (2):

$$E(T) = \frac{\beta}{r_0} \left( 1 - \frac{2gr_0\alpha(T-T_0)}{\beta} \right) = E_0 - 2g\alpha(T-T_0) \quad (2)$$

where,  $E(T)$  is the modulus of elasticity at temperature  $T$ ;  $E_0$  is the modulus of elasticity at the reference temperature  $T_0$ ;  $g$  is the anharmonic coefficient; and,  $\alpha$  is the coefficient of linear thermal expansion.

Equation (2) indicates the general trend: the modulus of elasticity decreases as the temperature increases. For common structural materials, the anharmonic coefficient  $g$  is often of the same order of magnitude as  $E_0$  [3]. If  $g = 0$ , the effect of temperature vanishes. Equation (2) defines the value of the modulus of elasticity at different temperatures in the diatomic model of a solid body and depends only on the asymmetry of the interatomic forces represented by  $g$ . However, the diatomic model does not take into account the influence of impurities and defects and the time (or rate) of loading.

Numerous experimental results currently available indicate that the modulus of elasticity and nonlinear deformation of materials are affected much more by micro- and macrostructure features (dislocations, micro-pores, and micro-crevices), the stress/strength ratio, and stress (or strain) rate of loading than by asymmetry of interatomic forces. The data provided by Bell [1] show that the change of the modulus of elasticity cannot be caused only by the change

of density of a material due to thermal expansion. According to the kinetic theory of the strength of solids, fracture is a change in the thermal movement of atoms, and a strain (stress) rate dependent phenomenon [2]. At the atomic-molecular level, the breaking of interatomic bonds due to thermal fluctuations control the fracture process. At the macroscopic level, the fracture of solid develops by a process that begins to develop in the body from the moment a load is applied and the fracture itself is the final act in this process. The material is a dynamic system of atoms interacting with external forces, rather than a static system. The thermal pressure caused by interatomic vibrations can be estimated [3] using Equation (3):

$$P = \frac{gkT}{2E_0W_a} \quad (3)$$

where,  $k = 1.38 \cdot 10^{-23}$  J/°K is Boltzmann's constant and  $W_a \approx 10^{-29}$  m<sup>3</sup> is the volume of an atom.

This thermal pressure leads to an equivalent stress of elastic forces and increases the local stress between atoms. A rough estimate illustrates that vibration of atoms with average kinetic energy causes load 'jerks' on the atomic bonds with stresses of the same magnitude as the strength of engineering materials [2]. For example: if  $g/E_0 \approx 1$  and  $T = 298$  K, then  $kT = 411 \cdot 10^{-23}$  J ( $\approx 2.5$  kJ/mol) and the thermal pressure is  $P \approx 206$  MP<sub>a</sub>. Thermal fluctuations of energy have an essential influence on the structure of real materials and predetermine their behavior under loading. In accordance with the kinetic nature of strength [2, 5], the fracture is the result of a process of nucleation, accumulation, and development of damage elements; i.e., a time-dependent phenomenon. It was shown [5] that the strength of different solid materials,  $\sigma_r$ , depends on the temperature and rate of loading given in Equation (4):

$$\sigma_r = U_0 / \gamma - (kT / \gamma) \ln(kT / \tau_0 \gamma) + (kT / \gamma) \ln \dot{\sigma} \quad (4)$$

where,  $U_0$  is the initial dissociation energy of the interatomic bonds;  $\gamma$  is structurally sensitive coefficient;  $\tau_0 \sim 10$ -13 seconds is the period of interatomic vibration; and,  $\dot{\sigma}$  is the stress rate of loading.

Also, according to the kinetic theory of solid strength, the linear extrapolation of the dependence  $\sigma_r \cdot (\ln \dot{\sigma})$  to  $\sigma_r = 0$  leads to a certain value of  $\ln \dot{\sigma}_0$ , which can be estimated [2, 5] using Equation (5):

$$\ln(\dot{\sigma}_0) = - \left[ \frac{U_0}{kT} + \ln \left( \tau_0 \frac{\gamma}{kT} \right) \right] \quad (5)$$

Then Equation (4) becomes Equation (6):



$$\sigma_r = kT / \gamma \ln(\dot{\sigma} / \dot{\sigma}_o) \quad (6)$$

Typical values of  $\gamma$  are 0.84~4.01 kJ·mol<sup>-1</sup>·MPa<sup>-1</sup> for metals and 0.06~0.39 kJ·mol<sup>-1</sup>·MPa<sup>-1</sup> for polymers [2]. From Equation (5), it follows that the dependencies on  $\tau_o$  and  $\gamma$  are logarithmic (small in comparison with linear dependency on  $U_o$ ). Thus,  $\ln(\dot{\sigma}_o)$  is determined essentially by the activation energy,  $U_o$ , of the solid. Therefore, knowing the values of  $kT$ ,  $\tau_o$ , and the level of activation energy  $U_o$ ,  $\ln(\dot{\sigma}_o)$  can be estimated using Equation (7):

$$\ln(\dot{\sigma}_o) = - \left[ \frac{U_o}{kT} + \ln \left( \tau_o \frac{\gamma}{kT} \right) \right] \quad (7)$$

Dynamic and quasi-static experiments show a nonlinear dependence between stress and strain, even at infinitesimal values of deformation ( $10^{-6} \sim 10^{-4}$ ) for a wide range of materials (metal, stone, concrete, wood, glass, polymers, etc.). Engineering materials deviate from Hook's law, and the stress-strain relationship may be approximated by a second-order Taylor series polynomial, as shown in Equation (8):

$$\sigma = E_o \varepsilon - b \varepsilon^2 \quad (8)$$

where,  $\sigma$  is stress,  $\varepsilon$  is strain;  $E_o$  is the elastic modulus; and,  $b$  is the nonlinear parameter [1].

Equation (8) clearly illustrates that the modulus of elasticity is linearly proportional to the strain given by Equation (9):

$$E = d\sigma / d\varepsilon = E_o - 2b\varepsilon \quad (9)$$

Corresponding values of the nonlinear parameter  $b$  can be determined by Equation (10):

$$b = (E_o - E) / 2\varepsilon = E_o(1 - E/E_o) / 2\varepsilon \quad (10)$$

By assuming equal distribution of an external load, all interatomic connections are strained equally, and the average stress,  $\sigma$ , acting on the body is equal to the stress  $\sigma_a$  acting on the atom. Under the action of stress  $\sigma_a$ , which is less than the ultimate value, the potential energy,  $U(\sigma_a)$ , is proportional to the volume of the atom,  $W_a$ , then Equation (8) becomes Equation (11) [3, 6]:

$$U(\sigma_a) = U_o - W_a \sigma_a b / E_o \quad (11)$$

On the other hand, Equation (12) shows that the potential energy decreases linearly with applied stress [2]:

$$U(\sigma) = U_o - \gamma \sigma_a \quad (12)$$

Then from Equations (11) and (12),  $b$  can be determined by Equation (13):

$$b = \gamma E_o / W_a = (kT / \sigma_r)(E_o / W_a) \ln(\dot{\sigma} / \dot{\sigma}_o) \quad (13)$$

It can be seen from Equations (8) and (13) that the adequate equation of state can be expressed as Equation (14):

$$\sigma = E_o \varepsilon - \frac{kT E_o}{W_a \sigma_r} \ln \left( \frac{\dot{\sigma}_s}{\dot{\sigma}_o} \right) \cdot \varepsilon^2 \quad (14)$$

Equation (15) shows the relationship between modulus of elasticity,  $E$ , and temperature,  $T$ :

$$E(T) = E_o - \left( \frac{2k E_o \varepsilon}{W_a \sigma_r} \ln \left( \frac{\dot{\sigma}_s}{\dot{\sigma}_o} \right) \right) \cdot T \quad (15)$$

Equations (14) and (15) are generally applicable for all solids that obey the kinetic theory of strength and that can be described with a parabolic stress-strain relationship. From a practical point of view, the right-hand side of Equations (14) and (15) depends on the known standards for solids [7-9]; that is, mechanical properties of specimens at a given reference temperature (typically 25°C): elastic modulus,  $E_o$ ; strength,  $\sigma_r$  (tensile or compressive); corresponding strain,  $\varepsilon$ ; and, stress rate of loading  $\dot{\sigma}_s$  and  $\dot{\sigma}_o$ .

## Case Studies

Equation (15) indicates the relationship between modulus of elasticity and temperature, as well as stress (strain) rate of loading. The temperature dependence is linear, while the stress (strain) rate dependence is logarithmic. Since the linear temperature dependence is stronger, the validity of the temperature dependence predicted by Equation (15) will be investigated first. Before making a rigorous comparison between Equation (15) and the published data, it should be noted that a number of studies [10-14] show that the relationship between Young's modulus and temperature is essentially linear for different engineering materials, consistent with Equation (15).

The following sections present a detailed theoretical scheme to estimate the relationship between modulus of elasticity and temperature. Then two very different engineering materials—ductile materials (solders and plastics) and brittle materials (concrete) will be used to illustrate the possible breadth of the theory. A benefit of disseminating this theory to the research community, along the sample cases presented here, is to allow experimental investigators

to compare their data with theory and encourage them to publish relevant test conditions along with their data.

## Metals

Existing published data [10-14] are used first to validate the hypothesis that Equation (15) describes in general the relationship between modulus of elasticity and temperature for metallic materials (steels, copper and copper alloys, nickel and nickel alloys, titanium, and aluminum and aluminum alloys). Figure 1 depicts the experimental data of modulus of elasticity versus temperature for ten different metals [10].

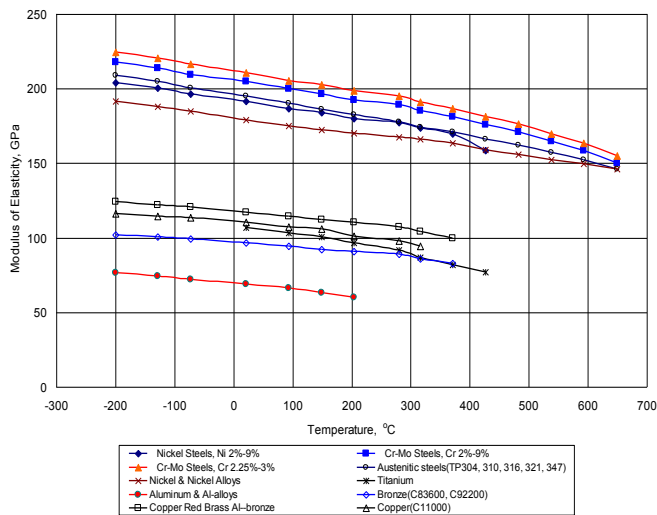


**Figure 1. Modulus of Elasticity versus Temperature for Metals**

On the other hand, the slope of the E-T curves can be expressed by Equation (16) from Equation (15):

$$\frac{dE}{dT} = -\frac{2k}{W_a} \frac{E_o \varepsilon}{\sigma_r} \ln \left( \frac{\dot{\sigma}_s}{\dot{\sigma}_o} \right) \quad (16)$$

The slopes ( $dE/dT$ ) and correlation coefficients for metals are calculated using Equation (16) and tabulated in Table 1. The correlation coefficients range from -0.945 to -0.998, indicating a very good linear relationship between modulus of elasticity and temperature for these materials. The modulus of elasticity decreases progressively with increasing temperature. The slope  $dE/dT$  is negative, and the relationship is essentially linear for all metals. The parameter values needed for the theoretical expression are available in the standards and literature [7, 8]. Therefore, published data were used also to check if Equation (15) predicts the absolute values of modulus of elasticity for different temperatures. For instance, the modulus of elasticity of lead-free

solders is a key material property that needs to be measured accurately in order to facilitate design, ensure reliability, and promote compliance with legislative restrictions on hazardous substances [11].

**Table 1. Existing Experimental Data for Metals**

Metals	$dE/dT$ , GPa/°C	Correlation Coefficient	Temperature Range, °C
Nickel steel Ni: 2%-9%	-0.065	-0.985	-200 and +427
Cr-Mo steels Cr.:0.5%-2%	-0.075	-0.989	-200 and +649
Cr-Mo steels Cr.:2.25%-3%	-0.078	-0.990	-200 and +649
Cr-Mo steels Cr.:5%-9%	-0.106	-0.945	-200 and +649
Austenitic steels	-0.072	-0.998	-200 and +649
Cooper (C11000)	-0.037	-0.987	-198 and +371
Cooper red brass Al-bronze	-0.040	-0.988	-198 and +371
Nickel, Monel 400	-0.052	-0.998	-198 and +649
Titanium	-0.075	-0.993	+21 and +427
Aluminum and Al-alloys	-0.040	-0.994	-198 and +204

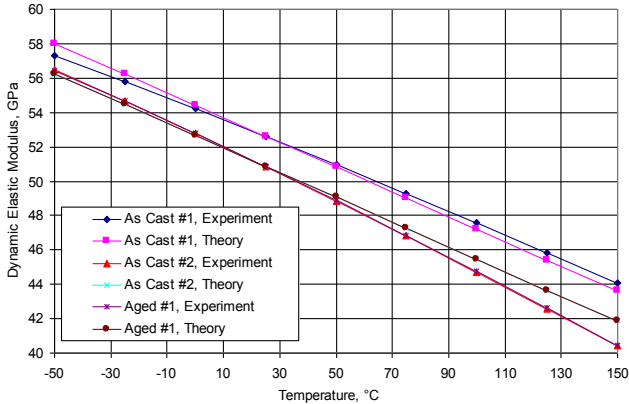
Data for the lead-free solder 96.Sn-3.5Ag [12-14] includes the following:

- Young's modulus of elasticity,  $E_o = 49$  GPa at 25°C and strain  $\varepsilon \approx 0.1\%$ , allows us to assume elastic behavior [9].
- Ultimate tensile strength,  $\sigma_r = 26.3$  MPa, at a strain rate of  $2.0 \times 10^{-4} \text{ s}^{-1}$ .
- The average of mean elastic modulus at 25°C (as-cast #1) = 5357.75 MPa, and mean elastic modulus at 25°C (aged) = 4312.55 MPa, and a strain rate of  $2.0 \times 10^{-4} \text{ s}^{-1}$  for calculating stress rate at static loading  $\dot{\sigma}_s$ .
- Average value of activation energy  $U_o \approx 09.85 \text{ kJ} \cdot \text{mol}^{-1}$  [11] for Equations (15) and (16).

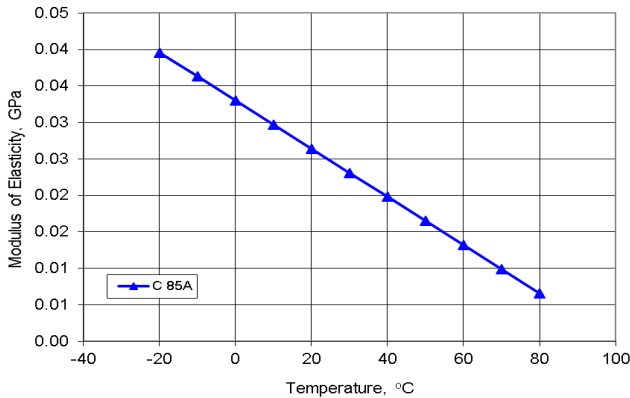
Figure 2 shows the comparison between theory, Equation (15), and experimental data for three solders: as-cast #1, as-cast #2, and aged #1 [11, 13]. Because the necessary test parameters were known, the differences between the theoretical and experimental values of the elastic modulus for the cases shown in Figure 2 are less than 4% at all temperatures, which is within the range of experimental error. The theory matches the published data reasonably well.

# Plastics

The values of the correlation coefficients were examined for different plastics at different ranges of temperature. Comparisons [9] also showed agreement between the theoretical modulus-temperature relationship and existing experimental data for plastics such as Elastollan Polyester C85A (Figure 3), Celcons M90 and GC25 (Figure 4), Polyethylene-HDPE (Figure 5), Chlorinated Polyvinyl Chloride-CPVC, and Polyvinylidene Fluoride-PVDF (Figure 6 and Table 2).



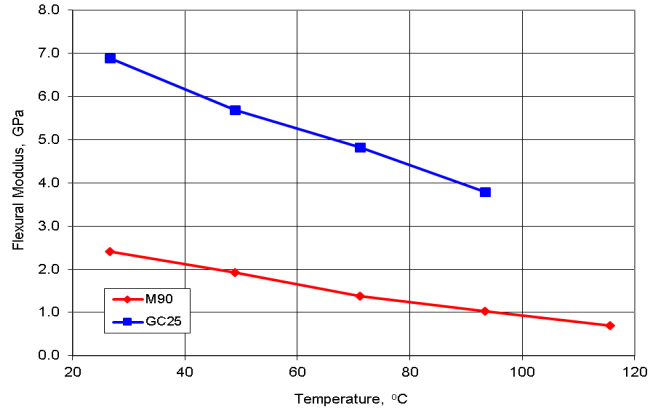
**Figure 2. Comparison of Theory, Equation (15), and Experimental Data for Three SnAgCu Solders**



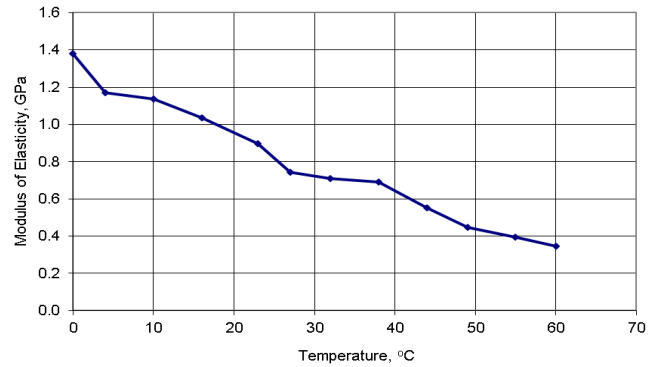
**Figure 3. Modulus of Elasticity versus Temperature for Elastollan Polyester**

Table 3 shows the values of slope ( $dE/dT$ ) for these plastics. It can be seen that the values of the slope ( $dE/dT$ ) are different for different materials and, consequently, depend on corresponding mechanical properties (e.g., modulus of elasticity at room temperature, strength, and activation energy) and on the test conditions (e.g., stress or strain rate of loading), which is in agreement with Equation (15). The correlation coefficients ranged from  $-0.950$  to  $-1.000$ , indi-

cating a good linear relationship between modulus of elasticity and temperature for these plastics. Therefore, it is possible to predict the modulus of elasticity at different temperatures using the mechanical properties of plastics at standard test conditions.



**Figure 4. Modulus of Elasticity versus Temperature for Celcons**



**Figure 5. Modulus of Elasticity versus Temperature for HDPE Pipe**

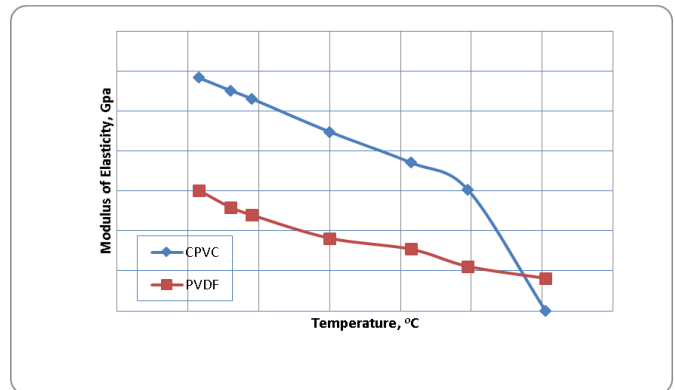


**Figure 6. Modulus of Elasticity versus Temperature for Plastics**

**Table 2. Existing Experimental Data for CPVC and PVDF**

	CPVC	PVDF
°C	E, GPa	E, GPa
23	2.917	1.510
32	2.758	1.296
38	2.655	1.200
60	2.241	0.910
83	1.855	0.772
99	1.517	0.558
121		0.407
Correlation Coefficient	-0.999	-0.984

**Table 3. Existing Experimental Data for Plastics**

Plastics	dE/dT, GPa/ °C	Correlation Coefficient	Temperature Range, °C
Celcon M90	-0.020	-0.990	+27 and +116
Celcon GC25	-0.046	-1.00	+27 and +93
Poluethylene (HDPE)	-0.016	-1.00	+60 and -1
PVC	-0.027	-1.00	+23 and +60
CPVC	-0.018	-1.00	+23 and +99
PP	-0.014	-0.950	+23 and +82
PVDF	-0.011	-0.990	+23 and +121
Ellastolan Polyester, C64D	-0.009	-0.900	-20 and +80

**Concrete**

Figure 7 shows the experimental data for modulus of elasticity at different temperatures for four concrete mixtures [15]. It can be seen that the modulus of elasticity decreases approximately linearly with the temperature increment. According to thermal properties, Equation (2), and the kinetic nature of strength of solid materials, the modulus of elasticity–temperature relationship, Equation (15), can be expressed [16] as Equation (17):

$$\frac{E}{E_o} = 1 - \frac{2k}{W_a} \frac{\sigma}{f'_o} \ln\left(\frac{\dot{\sigma}_s}{\dot{\sigma}_o}\right) \frac{T - T_o}{E_o} \quad (17)$$

where, E is the modulus of elasticity at the in situ temperature (T), Eo is the modulus of elasticity, and f' o is the strength of concrete specimens; both Eo and f' o are at the reference temperature To (typically room temperature).

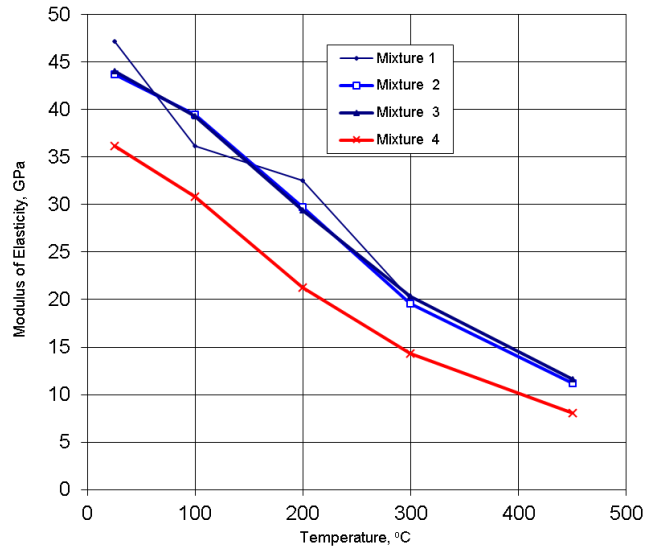


**Figure 7. Modulus of Elasticity versus Temperature for Concrete**

To determine the relative value of the static modulus of elasticity at elevated temperatures, Equation (17) requires the stress/strength ratio and the stress rate of loading. According to ASTM C469 [17],  $\sigma / f'_o = 0.4$  and  $\dot{\sigma}_s = 0.24$  MPa/s. Using these values for the test parameters, the ratio of modulus of elasticity can be calculated using Equation (18a) or Equation (18b):

$$\frac{E}{E_o} = 1 - 0.069 \frac{T - T_o}{E_o} \quad \text{when } 100^\circ\text{C} \leq T \leq 600^\circ\text{C} \quad (18a)$$

$$\frac{E}{E_o} = 1 - 0.079 \frac{T - T_o}{E_o} \quad \text{when } 100^\circ\text{C} \leq T \leq 450^\circ\text{C} \quad (18b)$$

The different slopes for the temperature range  $100^\circ\text{C} \leq T \leq 600^\circ\text{C}$  and  $100\text{--}450^\circ\text{C}$  are due to the different values of  $\ln(\dot{\sigma}_o)$  at  $U_o \approx 430 \text{ kJ}\cdot\text{mol}^{-1}$  [16], Equation (15), in the test procedures.

Tables 4 and 5 show experimental results for stressed tests with silica fume (mixture I: water-cement ratio w/c = 0.22,  $f'_o = 98$  MPa; mixture II: w/c = 0.33,  $f'_o = 88$  MPa) [15]. Tables 6 and 7 give experimental results of unstressed tests for concrete without silica fume (mixture III: w/c = 0.33,  $f'_o = 75$  MPa), and with silica fume (mixture II) [15]. The average slope of the elastic modulus in the temperature range  $100\text{--}450^\circ\text{C}$  was  $-0.079$ . In all cases, as shown in the tables, the relative static elastic modulus–temperature de-

pendencies are similar; they are all approximately linear (correlation coefficients close to  $-1.000$ ), which shows good correspondence to the general analytical model presented here.

**Table 4. Relative Static Modulus of Elasticity Mixture I, Stressed Tests,  $E_0 = 45$  MPa**

T, °C	E/E <sub>0</sub> , [15]	Eq. (18a)
25	1.00	1.00
100	0.79	0.88
200	0.69	0.73
300	0.53	0.58
450	0.24	0.35
600	0.13	0.12
Correl	-0.989	-1.000

**Table 5. Relative Static Modulus of Elasticity Mixture II, Stressed Tests,  $E_0 = 42$  MPa**

T, °C	E/E <sub>0</sub> , [15]	Eq. (18b)
25	1.00	1.00
100	0.89	0.87
200	0.78	0.70
300	0.59	0.53
450	0.34	0.27
Correl	-0.997	-1.000

**Table 6. Relative Static Modulus of Elasticity Mixture III, Unstressed Tests,  $E_0 = 43$  MPa**

T, °C	E/E <sub>0</sub> , [15]	Eq. (18b)
25	1.00	1.00
100	0.87	0.87
200	0.70	0.70
300	0.48	0.53
450	0.29	0.27
Correl	-0.996	-1.000

The tests for residual dynamic modulus of elasticity were performed by NIST at room temperature (before and after heating) in accordance with ASTM C215 [18]. Figures 8-10 show that the relative residual dynamic modulus of elasticity decreases approximately linearly with temperature. The error between the predicted, Equation (10b), and experimental values does not exceed 15% in the temperature range 100–450°C (except Mixture IV at 450 °C).

**Table 7. Relative Static Modulus of Elasticity Mixture II, Unstressed Tests,  $E_0 = 42$  MPa**

T, °C	E/E <sub>0</sub> , [15]	Eq. (10b)
25	1.00	1.00
100	0.93	0.87
200	0.72	0.70
300	0.47	0.53
450	0.27	0.27
Correl	-0.993	-1.000

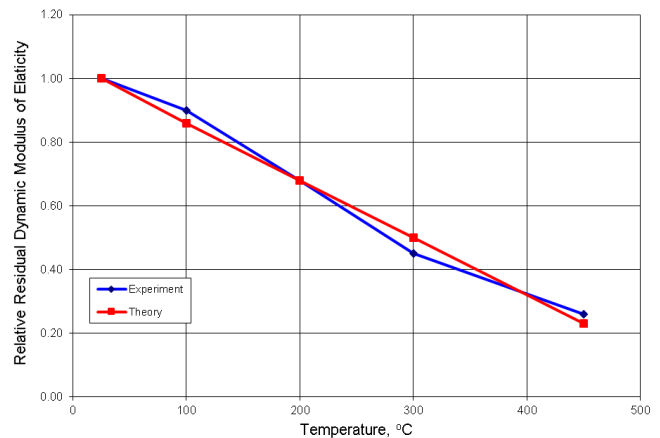


**Figure 8. Relative Residual Dynamic Modulus of Elasticity versus Temperature (Mixture II)**

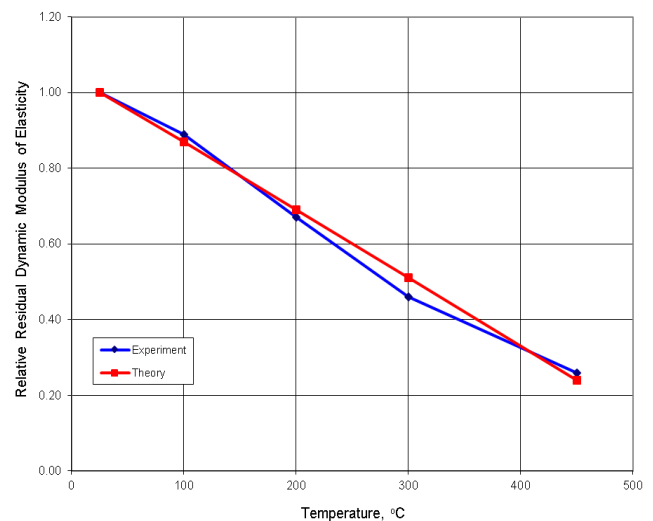


**Figure 9. Relative Residual Dynamic Modulus of Elasticity versus Temperature (Mixture III)**



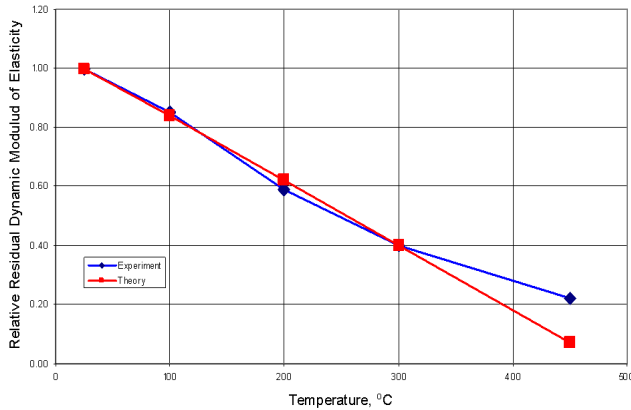


**Figure 10. Relative Residual Dynamic Modulus of Elasticity versus Temperature (Mixture IV)**

Strength, modulus of elasticity, and ultrasonic pulse velocity of concrete all decrease with increasing porosity [15]. Elevated temperature causes damage and increases porosity. This effect of temperature provides the physical background for estimating the mechanical properties of concrete at elevated temperature.

## Conclusion

The modulus-temperature relationships of industrial materials are always determined experimentally. As an alternative, a new analytical relationship between elastic modulus and temperature is presented. The resulting expression, Equation (15), is based on parabolic stress-strain dependence and the kinetic nature of strength of solids. Preliminary comparisons with existing experimental data provide promising results. These results indicate that the modulus of elasticity at different temperatures can be predicted by Equation (15) using well-known physical constants and the mechanical properties of each material only at room temperature (in accordance with existing test standards).

The theoretical E(T) model developed in this study can change the traditional experimental approach for obtaining one of the most important material properties, modulus of elasticity, at different temperatures. The presented model has the potential to eliminate a lot of time-consuming and costly material testing and to benefit material engineers and scientists greatly in analytical and design work. This E(T) model may significantly enhance and facilitate analysts in material engineering and manufacturing process simulations because the validity of the simulation results depends strongly on the inputs of the material properties. From the simulation, the temperature distribution is predicted, and this E(T) model will allow the theoretical prediction of E. It will allow designers to improve the performance and reliability

of parts by knowing how their properties will vary over different operating temperatures. For materials and locations where it is difficult to experimentally measure the modulus of elasticity, the E(T) model may provide a reliable and convenient way to predict modulus at different locations such as on the surface and inside the part.

## Acknowledgments

The author wishes to thank the Kettering University Department of Mechanical Engineering for providing partial funding for this research.

## Nomenclature

$E$	modulus of elasticity at instantaneous temperature, $T$
$E_0$	modulus of elasticity at reference temperature, $T_0$
$F$	force
$f_0'$	strength of concrete specimens at the reference temperature
$g$	anharmonic coefficient
$k$	Boltzmann's constant
$P$	thermal pressure
$r$	distance between atoms
$r_0$	the distance between atoms at equilibrium position
$T$	temperature
$T_0$	reference temperature
$U_0$	activation energy
$U$	potential energy
$W_a$	volume of an atom
$\alpha$	coefficient of linear thermal expansion
$\beta$	coefficient of linear elasticity
$\varepsilon$	strain
$\gamma$	structural sensitivity coefficient
$\sigma$	stress
$\sigma_r$	strength
$\dot{\sigma}_s$	stress rate
$\dot{\sigma}_0$	the approximation of stress rate as a result of Extrapolating the value of strength to zero
$\tau_0$	the period of interatomic vibration

---

## References

- [1] Bell, J. F. (1983). *Mechanics of Solids: The experimental foundations of solid mechanics*, Springer-Verlag, New York.
- [2] Regel, V. R., Slutzker A. I., & Tomashevsky E. E. (1974). *Kinetic Nature of Solids Strength*, Nauka: Moscow.
- [3] Frenkel, J. (1946). *Kinetic Theory of Liquids*, Dover Publications, Inc.
- [4] Layus L. A., Slutzker, A. I., Gofman I. V., & Gilarov, V. L. (2004). Correlation of the Characteristics of Reversible Thermal, and Force Deformations in Solid Bodies of Different Structures. *Phys. Solid States*, 46(6), 1115-1122.
- [5] Betekhtin, V. I., Kuksenko, V. S., Slutzker, A. I., & Shkolnik, I. E. (1994). Fracture Kinetics and the Dynamic Strength of Concrete. *Physics of the Solid State*, American Institute of Physics; 1416-1421.
- [6] Shkolnik, I. E. (1996). Evaluation of Dynamic Strength of Concrete from Results of Static Tests. *ASCE Journal of Engineering Mechanics*, 122(12), 1133-1138.
- [7] ASTM Standard E8 (2009). *Standard Test Methods for Tension Testing of Metallic Materials*, ASTM International, West Conshohocken, PA, DOI: 10.1520/E0008\_E0008M-09, www.astm.org
- [8] ASTM Standard E111 (2004). *Standard Test Method for Young's Modulus, Tangent Modulus, and Chord Modulus*, ASTM International, West Conshohocken, PA, DOI: 10.1520/E0111-04, www.astm.org
- [9] ASTM Standard D638 (2008). *Standard Test Method for Tensile Properties of Plastics*, ASTM International, West Conshohocken, PA, DOI: 10.1520/D0638-08, www.astm.org
- [10] Fabco Plastics (2007). Retrieved from [http://www.fabcoplastics.com/file\\_library/documents/1\\_FabcoEngineeringData.pdf](http://www.fabcoplastics.com/file_library/documents/1_FabcoEngineeringData.pdf)  
The Engineering Toolbox,  
<http://www.engineeringtoolbox.co>
- [11] *Database for Solder Properties with Emphasis on New Lead-free Solders*, Release 4.0, NIST.
- [12] Cheng, Y. W., & Siewert, T. A. (2003). Predicting of tensile Properties of the Bulk 96Sb-3.5Ag Lead-Free Solder. *Journal of Electronic Materials*, 32(6), 535-540.
- [13] Shkolnik, I., Palmer, M., Dong, Y., & Cameron, T. (2007). The Relationship between Elastic Modulus of Lead-Free Solders and Temperature. *Proceedings of ASNT Fall Conference and Quality Testing Show*, Las Vegas, NV, November 12-16, 244-246.
- [14] Syed, A. (2004). Accumulated Creep Strain and Energy Density Based Thermal Fatigue Life Prediction Models for SnAgCu Solder Joints. *54th ECTC Conference Proceedings*, 737-746.
- [15] Phan, L. T., & Carino, N. J. (2002). Effects of Test Conditions and Mixture Proportions on Behavior of High-Strength Concrete Exposed to High Temperatures. *ACI Materials Journal*, 54-66.
- [16] Shkolnik, I. E. (2005). Effect of Nonlinear Response of Concrete on Its Elastic Modulus and Strength. *Cement and Concrete Composites*, 27, 747-757.
- [17] ASTM Standard C469-02e1 (2002). *Standard Test Method for Static Modulus of Elasticity and Poisson's Ratio of Concrete in Compression*, ASTM International, West Conshohocken, PA, DOI: 10.1520/C0469-02E01, www.astm.org
- [18] ASTM Standard C215 (2008). *Standard Test Method for Fundamental Transverse, Longitudinal, and Torsional Frequencies of Concrete Specimens*, ASTM International, West Conshohocken, PA, DOI: 10.1520/C0215-08, www.astm.org

## Biography

**YAOMIN DONG** is an associate professor of mechanical engineering at Kettering University. He earned his MS and PhD (Mechanical Engineering) degrees from the University of Kentucky. Dr. Dong is currently teaching at the Kettering University. His interests include solid mechanics, computer-aided engineering, finite element analysis, and engineering materials. Dr. Dong may be reached at [ydongl@kettering.edu](mailto:ydongl@kettering.edu)

# PARAMETER ESTIMATION IN RATIO-DEPENDENT PREDATOR-PREY ECOLOGICAL SYSTEMS WITH BIAS DISTURBANCE

Dale B. McDonald, Midwestern State University

## Abstract

Determination of accurate parameter estimates in predator-prey dynamic systems was the primary focus of this treatment. It was assumed that a bias disturbance existed in the predator biomass time rate of change equation. This equation was sampled using the methods of response surface modeling, which serves as the mechanism in which “scattered data” of a type that would present from field measurements was collected. Once this was accomplished, ecological parameters were estimated that could describe ratio-dependent systems. Fundamental system behavior was exposed; parameter estimation was achieved despite an increasing bias disturbance that could be seen as the limiting case of uncertainty approaching some reasonable upper bound. The significance of this treatment is revealed when broad implications are considered. Field data that are relevant to predator-prey dynamic systems is almost certainly to appear in discrete form. That is, the analyst will receive scattered data from which conclusions must be made. It is imperative that parameter estimation techniques, given an underlying control (harvesting) algorithm, readily accept such data. Furthermore, a robust parameter estimation methodology must be pursued, which provides the analyst with the confidence that important information (parameters) may be discerned despite the reality that uncertainty (at levels increasing) exists within the predator-prey dynamic system. This treatment provides 1) a robust means to estimate parameters that is specifically made to assume that the input (data) is in scattered form and 2) illuminates the utility of this methodology by comparing estimated parameter values against true parameter values via an error analysis.

## Introduction

Predator-prey interactions are often described by ordinary differential equations (ODEs). Such dynamic systems provide for understanding, analysis, and prediction of important ecological phenomena. It is significant to note that while dynamic ODE models are used to understand such systems, field observations are most likely to present in scattered form. Data collected is the output of some ecological system at distinct moments in time.

Due to the discrete nature of expected observations, parameter estimation must be able to efficiently synthesize such data structures. Therefore, response surface models (RSMs) provide a pragmatic avenue for parameter estimation; RSMs accept scattered data and output continuous and differentiable models. These models will be used to determine accurate parameter estimates despite a bias disturbance in the fundamental predator-prey dynamics. As will be illustrated in what follows, of primary concern are estimates and estimation error for parameters that appear in the predator biomass ODE in ratio-dependent systems. It must be noted that the methodology/analyses presented are based on data sampled from the biomass time rate of change equation rather than data sampled from the field. This was intentional, due to the desire to develop analytical and numerical (modeling) techniques that will be receptive to data received from the field.

Several published studies are relevant to this current study. In a study by McDonald [1], the cubic radial basis function (RBF) was used to reconstruct predator dynamics from scattered data in the absence of a disturbance. It was shown that the combination of this RBF and an interpolation parameter  $c$  allowed for accurate estimation of parameters within the relevant ratio-dependent predator-prey system. In another study by McDonald [2], that notion was extended to specify a constructive means by which the analyst may be confident that the estimates are accurate. This was shown by demonstrating that sensitivity or, perhaps more accurately, insensitivity of developed models with respect to the interpolation parameter  $c$  is a useful benchmark for selecting appropriate estimates.

As a point of reference, McDonald et al. [3] provided information on the nature of the RBFs, and their construction, considered in the present treatment. Given the predator-prey dynamic system, including the bias disturbance, it will be demonstrated that RSM models, including function and gradient information, will be leveraged to provide accurate parameter estimates, given the uncertainty. This is significant in that the methodology specified in the literature may now be extended to account for this significant class of disturbances.

## Foundational Information

The present study considered a model that is a member of a ratio-dependent predator-prey dynamic system. More information regarding ratio-dependency and what is known as prey-dependent mathematical models may be found in other studies [4, 5].

## Predator-Prey Dynamic System Model

The ratio-dependent predator-prey system under consideration [6] is a Holling-Tanner model variant [7, 8] and may be described by the ODEs in Equation (1):

$$\dot{x}_1 = rx_1 \left(1 - \frac{x_1}{K}\right) - \frac{\beta x_1 x_2}{\alpha + x_1} - qux_1 \quad (1)$$

and

$$\dot{x}_2 = sx_2 \left(1 - \frac{x_2}{vx_1}\right)$$

In Equation (1), the prey biomass is  $x_1$  and predator biomass is  $x_2$ . Note that the parameter  $v$  expresses a relationship between predator and prey biomass at equilibrium. Intrinsic growth rate for the predator is  $s$ ;  $q$  is the catchability coefficient; the constant  $\alpha$  is the half-saturation level; and,  $\beta$  is the maximum harvesting rate. For the prey,  $r$  is the intrinsic growth rate and  $K$  is the carrying capacity [6]. During the parameter estimation process, a harvesting (control) algorithm [1] will be invoked. The algorithm developed in that treatment was termed instantaneous maximization of net economic revenue (IMNER). It was derived for predator-prey systems such as Equation (1) in an effort to specify harvesting effort (control  $u$ ) such that net economic revenue, as given in the study by Kar et al. [6], was instantaneously maximized. It was shown [1] that the IMNER algorithm produced sustainable, equilibrium (parameter) values of predator and prey. This is noteworthy, as IMNER accounted for accumulation of revenue, significant to both economic ventures in terms of net economic revenue and regulatory (often governmental) agencies in terms of total discounted net economic revenue [6]. The study by McDonald [1] gives the details of the IMNER algorithm (including the details regarding appropriate necessary conditions given by the Lagrangian). The algorithm is shown in Equation (2):

$$\begin{aligned} u &= u_{\min} \text{ if } \sigma > 0 \\ u &= u_{\max} \text{ if } \sigma < 0 \\ u &= u_s \text{ if } \sigma = 0 \end{aligned} \quad (2)$$

where,  $\sigma$  is defined in Equation (3):

$$\sigma = -(q(p - \tau)x_1 - C) \quad (3)$$

and the net economic revenue is given by Equation (4):

$$\text{Net Economic Revenue} = (q(p - \tau)x_1 - C) \quad (4)$$

where,  $p$  is the price per unit biomass of the prey,  $\tau$  is the rate of taxation and  $C$  is the cost of fishing per unit effort.

In effect, the IMNER algorithm selects a control law to instantaneously maximize net economic revenue at each instant in time. The reason to summarize the IMNER algorithm is as follows: parameter estimates from this study were developed for use in any dynamic system model so that the control law Equation (2) may be implemented. Therefore, RSM models built from the second equation of Equation (1) aid in the control (harvesting effort) of the ratio-dependent system. Once parameter estimates have been obtained (the subject of this current treatment), then harvesting algorithms such as IMNER may be appropriately implemented.

## Bias Dynamic System Formulation

As McDonald's study [2] indicated, the predator biomass time rate of change (PBTRC) is the right-hand side of the second equation of Equation (1) and restated as Equation (5). To demonstrate the utility of the proposed methodology, the PBTRC was sampled across a grid of points; however, suppose that the actual system is in the form of Equation (1), yet due to measurement or other error, the scattered data were taken from Equation (5):

$$\dot{x}_2 = F(x) = sx_2 \left(1 - \frac{x_2}{vx_1}\right) + \eta \quad (5)$$

where,  $\eta$  is a bias (constant) disturbance, whose magnitude is varied in the forthcoming analysis.

It is important to explicitly state the reasons for adding the bias disturbance,  $\eta$ . First, even without perfect knowledge of the PBTRC, the proposed methodology produces accurate parameter estimates. Secondly, assuming a normal distribution, many species reproduce, thrive, and decline at an established rate, but outliers (say, at two standard deviations) do exist. The methodology here, with an increased or decreased predator biomass time rate of change (positive or negative  $\eta$ ), could represent the behavior of such outliers. Now, easily calculated is the gradient of Equation (5), where Equations (5) and (6) are equivalent to that found in McDonald's study [2] but contain the bias disturbance,  $\eta$ .

$$\frac{\partial(\dot{x}_2)}{\partial x} = \frac{\partial F}{\partial x} = \left[ \frac{sx_2^2}{vx_1^2}, s - \frac{2sx_2}{vx_1} \right] \quad (6)$$

## Response Surface Models

This treatment, both due to precedent and consistency, utilizes the so-called cubic radial basis function. For detailed information on this and other radial basis functions, refer to the study by McDonald et al. [3]. Paying particular attention to the bias disturbance,  $\eta$ , the intent was to construct RSMs by sampling  $F(x)$ . Within many RSMs, the specification of parameter  $c$  is somewhat of an open question and free to be specified, in some manner, by the analyst. The results of studies by McDonald [1, 2] guide the choice of both the particular radial basis function and the value of the interpolation parameter  $c$ .

## Biomass Equilibrium State Allowed

The (bias) altered system given by Equation (5) was considered over biomass (state) levels of  $F(x)$  sampled over  $x_1 = 1, 1.1, \dots, 3$ , and  $x_2 = 5, 5.1, \dots, 7$ . Note that over this sampled parameter space,  $x_2 = vx_1$  was allowed with  $v = 5$ . Also, let  $q = 0.01$ ,  $s = 1.2$ ,  $\alpha = 10$ ,  $K = 200$ ,  $\beta = 0.1$ , and  $r = 1.5$ . Considering Equations (5) and (6), RSMs were constructed to determine the effect of the bias disturbance,  $\eta$ , upon accuracy of parameter estimates. There may be situations where physical implications or other insights provide reasonable bounds on a bias disturbance. This work is especially valuable in that case. The focus was upon the cubic radial basis function [2, 3] shown in Equation (7):

$$\phi(r) = (r + c)^3 \quad (7)$$

From the RSM created via this RBF, Equation (7), evaluated function and gradient values were used to estimate and quantify error for parameter estimates of  $s$  and  $v$ . To begin, let the true parameter values be given as in the discussion that began this section. Given the methodology outlined in the study by McDonald et al. [3] and the grid of points over which  $F(x)$  is sampled as previously mentioned, a response surface model  $f(x)$  via numerical simulation was created. Then the gradient vector of the model  $f(x)$  evaluated at prey biomass levels  $x_1 = 1.513$  and predator biomass levels  $x_2 = 5.513$  was used to calculate estimates. Parameter estimation in the absence of the bias disturbance was reported in the study by McDonald [2]. A fundamental point addressed presently is to discern if biomass equilibrium is required to generate useful estimates.

Assume  $\eta = 0$ . In this case, the RSM reproduces the results from McDonald [2] for the gradient vector. Let  $x_1 =$

1.513 and  $x_2 = 5.513$  and utilize the cubic radial basis function with the interpolation parameter  $c = 1.25$ . From Equation (8), the gradient yields

$$\frac{\partial F}{\partial x} = [3.18612 \quad -.55216] \quad (8)$$

Now let  $\eta = 0.5$  in appropriate units, as given in Equation (9):

$$\frac{\partial F}{\partial x} = [3.18582 \quad -.55245] \quad (9)$$

Next let  $\eta = 5.0$  in appropriate units, as given in Equation (10):

$$\frac{\partial F}{\partial x} = [3.18317 \quad -.55511] \quad (10)$$

Finally, let  $\eta = 50.0$  in appropriate, as given in Equation (11):

$$\frac{\partial F}{\partial x} = [3.15667 \quad -.58161] \quad (11)$$

Equations (9)-(11) contain the gradient evaluated at three different levels of bias. With  $\eta = 0.5$  considering Equations (6) and (11), see Equation (12):

$$\left[ \frac{sx_2^2}{vx_1^2} \quad s - \frac{2sx_2}{vx_1} \right] = [3.18582 \quad -.55245] \quad (12)$$

Then solving for  $s$  and  $v$  with the biomass levels specified, and based upon the gradient of the RSM, only yields the values shown in Equation (13):

$$\begin{bmatrix} s = 1.1962 \\ v = 4.9852 \end{bmatrix} \quad (13)$$

with  $\eta = 5.0$  and Equation (14),

$$\left[ \frac{sx_2^2}{vx_1^2} \quad s - \frac{2sx_2}{vx_1} \right] = [3.18317 \quad -.55511] \quad (14)$$

Then solving for  $s$  and  $v$  with the biomass levels specified, and based upon the gradient of the RSM, only yields the values shown in Equation (15):

$$\begin{bmatrix} s = 1.1921 \\ v = 4.9722 \end{bmatrix} \quad (15)$$

with  $\eta = 50.0$  and Equation (16),

$$\left[ \frac{sx_2^2}{vx_1^2} \quad s - \frac{2sx_2}{vx_1} \right] = [3.15677 \quad -.58161] \quad (16)$$



Equation (17) gives  $s$  and  $v$  with the biomass levels specified and, based upon the gradient of the RSM, yields the values shown:

$$\begin{bmatrix} s = 1.1511 \\ v = 4.8413 \end{bmatrix} \quad (17)$$

Based upon the gradient, Equations (18) and (19) give the error in  $s$  and  $v$  with  $\eta = 0.5$ :

$$Error \%s = \frac{(1.2 - 1.1962)}{1.2} \times 100 = 0.317\% \quad (18)$$

$$Error \%v = \frac{(5 - 4.9852)}{5} \times 100 = 0.296\% \quad (19)$$

Based upon the gradient, Equations (20) and (21) give the error in  $s$  and  $v$  with  $\eta = 5.0$ :

$$Error \%s = \frac{(1.2 - 1.1921)}{1.2} \times 100 = 0.653\% \quad (20)$$

$$Error \%v = \frac{(5 - 4.9722)}{5} \times 100 = 0.556\% \quad (21)$$

Based upon the gradient, Equations (22) and (23) give the greatest error in  $s$  and  $v$  with  $\eta = 50.0$ :

$$Error \%s = \frac{(1.2 - 1.1511)}{1.2} \times 100 = 4.075\% \quad (22)$$

$$Error \%v = \frac{(5 - 4.8413)}{5} \times 100 = 3.174\% \quad (23)$$

Equations (12-17) contain the parameter estimates at varying levels of bias, while Equations (18-23) display the error estimates.

## Biomass Equilibrium State Not Allowed

It is necessary to consider how the methodology performs if the RSM does not sample over the biomass equilibrium state  $x_1 = vx_2$  with  $v = 5$ . The previously mentioned results would still be valid, despite the outcome, but this restriction speaks to the robustness of using RSMs to estimate ecological parameters. Now  $F(x)$  was sampled over  $x_1 = 1, 1.05, 1.1, \dots, 3$  and  $x_2 = 1, 1.1, \dots, 3$ . For comparison purposes given these restrictions, the gradient vector of the model  $f(x)$  evaluated at prey biomass levels  $x_1 = 1.513$  and predator biomass levels  $x_2 = 2.513$  is reported. With  $\eta = 0.5$  and Equations (24) and (25):

$$\frac{\partial F}{\partial x} = [.65948 \quad .39977] \quad (24)$$

$$\begin{bmatrix} \frac{sx_2^2}{vx_1^2} & s - \frac{2sx_2}{vx_1} \end{bmatrix} = [.65948 \quad .39977] \quad (25)$$

Then solving for  $s$  and  $v$  with the biomass levels specified, and based upon the gradient of the RSM, yields the values shown in Equation (26):

$$\begin{bmatrix} s = 1.1939 \\ v = 4.9942 \end{bmatrix} \quad (26)$$

with  $\eta = 5.0$  and considering Equation (6),

$$\frac{\partial F}{\partial x} = [.65683 \quad .39709] \quad (27)$$

$$\begin{bmatrix} \frac{sx_2^2}{vx_1^2} & s - \frac{2sx_2}{vx_1} \end{bmatrix} = [.65683 \quad .39709] \quad (28)$$

Then solving for  $s$  and  $v$  with the biomass levels specified, and based upon the gradient of the RSM, yields the values in (29):

$$\begin{bmatrix} s = 1.1880 \\ v = 4.9897 \end{bmatrix} \quad (29)$$

with  $\eta = 50$  and Equations (30) and (31),

$$\frac{\partial F}{\partial x} = [.63035 \quad .37024] \quad (30)$$

$$\begin{bmatrix} \frac{sx_2^2}{vx_1^2} & s - \frac{2sx_2}{vx_1} \end{bmatrix} = [.63035 \quad .37024] \quad (31)$$

Then solving for  $s$  and  $v$  with the biomass levels specified, and based upon the gradient of the RSM, yields the values shown in Equation (32):

$$\begin{bmatrix} s = 1.1293 \\ v = 4.9422 \end{bmatrix} \quad (32)$$

Equations (24-32) provide parameter estimates for varying levels of disturbance from which percent error calculations may be generated. Based upon the gradient, Equations (33) and (34) give the error in  $s$  and  $v$  with  $\eta = 0.5$ :

$$Error \%s = \frac{(1.2 - 1.1939)}{1.2} \times 100 = 0.5\% \quad (33)$$

$$Error \%v = \frac{(5 - 4.9942)}{5} \times 100 = 0.116\% \quad (34)$$

Based upon the gradient, Equations (35) and (36) give the error in  $s$  and  $v$  with  $\eta = 5.0$ :

$$Error \%s = \frac{(1.2 - 1.1880)}{1.2} \times 100 = 1.0\% \quad (35)$$

$$Error \%v = \frac{(5 - 4.9897)}{5} \times 100 = 0.206\% \quad (36)$$

Based upon the gradient, Equations (37) and (38) give the greatest error in  $s$  and  $v$  is found with  $\eta = 50.0$ :

$$Error \%s = \frac{(1.2 - 1.1293)}{1.2} \times 100 = 0.589\% \quad (37)$$

$$Error \%v = \frac{(5 - 4.9422)}{5} \times 100 = 1.156\% \quad (38)$$

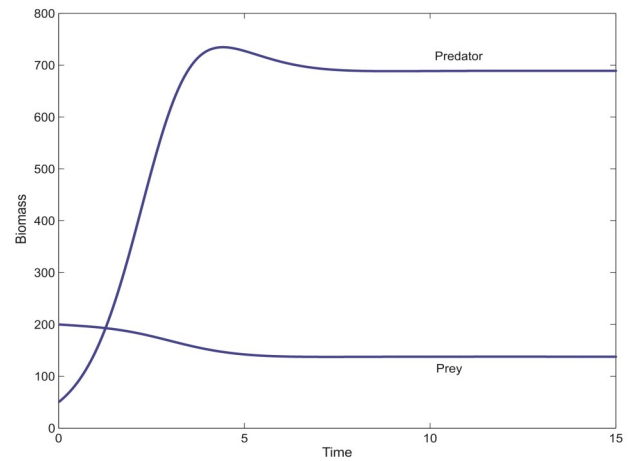
Equations (33-38) show that the RSM methodology is quite robust to bias disturbance in the PBTRC.

## Discussion

It is necessary at this point to further discuss why a (constant) bias disturbance was applied to Equation (5). First, it is common in situations where physical measurements are taken that an instrument or methodology used to gather data inherently contain uncertainty. Secondly, RSM methods discerned parameter estimates across several different magnitudes of uncertainty. Consider a time-varying disturbance that would, say, evolve subject to some physically reasonable upper and lower limits. In this case, the methodology would have generated data points where some could have higher levels of uncertainty (near the bound) and some nearer in magnitude to zero, for example.

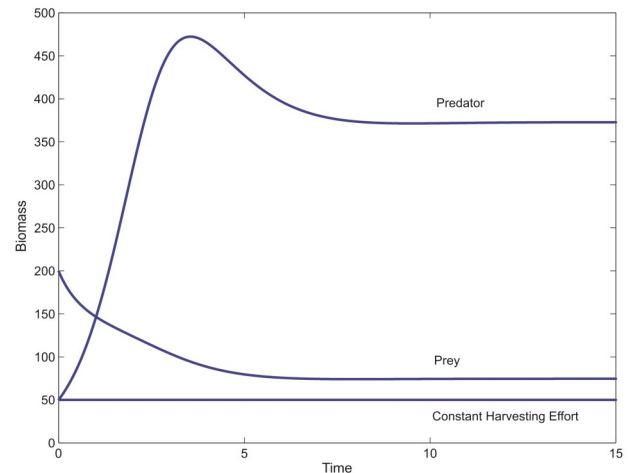
The purpose was, in effect, to assume a worst-case level of disturbance in terms of magnitude (at an upper limit) and then compare parameter estimates at this level of uncertainty (or bound on uncertainty) increased. Had a time-varying disturbance been present, it would have had a greater effect (again depending on the bound) as to if equilibrium populations of predator and prey would be possible or if the predator and prey biomass levels would oscillate about such equilibrium points but vary with time, as driven by the time-varying disturbance.

Figure 1 illustrates system behavior, Equation (1), without bias and without harvesting pressure. This creates a baseline to observe how the manner by which not only the bias but also harvest affects the time evolution of predator and prey.



**Figure 1. System Behavior: No Harvesting Effort (no bias)**

In Figure 2, a constant, nonzero harvesting effort,  $u = 50$  is applied to the system. This was intended, in a small way, to demonstrate how interconnected a control law once implemented may affect a particular system. In Figure 3, the behavior of the system, Equation (1), without bias disturbance and subject to the IMNER algorithm is displayed. The behavior of the system without bias disturbance compared to that where the disturbance  $\eta = 0.5$  was nearly identical and does not supply a useful visual representation.



**Figure 2. System Behavior: Constant Harvesting Effort (no bias)**

In Figure 4, the behavior of the system with bias disturbance  $\eta = 5.0$  is presented. In Figure 5, the behavior of the system with bias disturbance  $\eta = 50.0$  is presented. The biomass and harvesting efforts denoted by the solid line represent the system without bias, where the dashed line

considers the effect of the bias upon the evolution of the system over time. These figures in combination with the percent error estimates reveal that the fundamental goal of parameter estimation was achieved. Of course, as  $\eta$  increases, the estimation is less accurate. The biomass equilibrium clearly changes, however, for a relatively large change in magnitude disturbance  $\eta = 0.5, 5.0,$  and  $50.0$  in the predator biomass time rate of change, the percentage error is quite small and the parameter estimates given by Equations (13, 15, 17, 26, 29, and 32) are reasonable.

This is especially poignant in that it is incredibly difficult to estimate levels exactly. The key is that parameters that affect estimates globally by the mathematical model are quite accurate. Despite small to large disturbances in the predator biomass time rate of change, critical relationships such as the predator intrinsic growth rate and the relationship between predator and prey biomass at equilibrium may be illuminated.

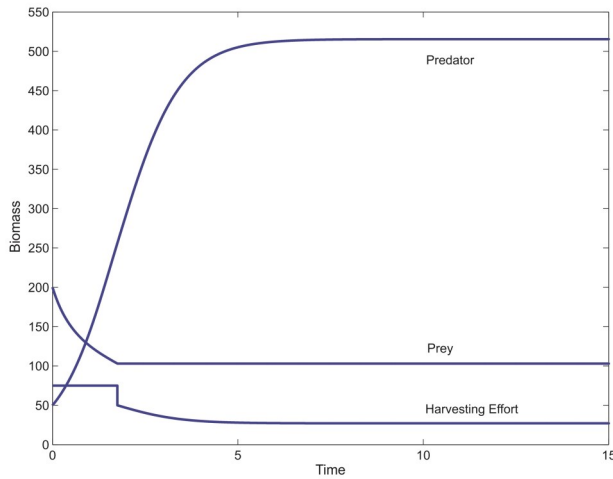


**Figure 3. System Behavior with the IMNER Harvesting (control) Effort (no bias)**

A comparison of the parameter estimates when the equilibrium condition is allowed and not allowed is presented. Considering Equations (13, 15, and 17) to Equations (26, 29, and 32) for the predator intrinsic growth rate, differences are shown in Equation (39):

$$\begin{aligned} |s_{13} - s_{26}| &= |1.1962 - 1.1939| = 0.0023 \\ |s_{15} - s_{29}| &= |1.1921 - 1.1880| = 0.0041 \\ |s_{17} - s_{29}| &= |1.1511 - 1.1293| = 0.0218 \end{aligned} \quad (39)$$

and for the steady-state equilibrium parameter,  $v$ , see Equation (40):

$$\begin{aligned} |v_{13} - v_{25}| &= |4.9852 - 4.9942| = 0.0090 \\ |v_{15} - v_{27}| &= |4.9722 - 4.9897| = 0.0175 \\ |v_{17} - v_{29}| &= |4.8413 - 4.9422| = 0.1009 \end{aligned} \quad (40)$$

Equations (39) and (40) further support this methodology as a robust means to estimate parameters.

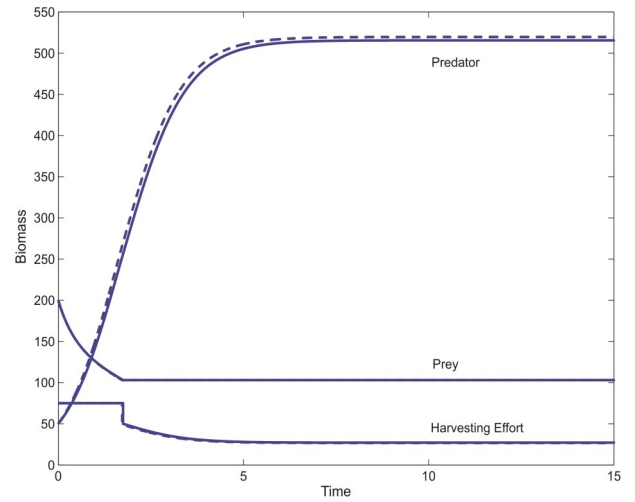


**Figure 4. System Behavior with IMNER Harvesting Effort (bias = 5.0)**

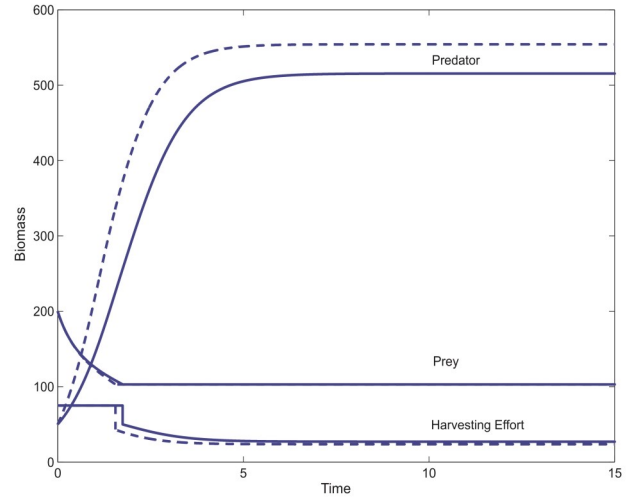


**Figure 5. System Behavior with IMNER Harvesting Effort (bias = 50.0)**

---

## Conclusions

Parameter estimation aided by the construction of RSMs yields accurate parameter estimates for ecological systems. Note that the sampled parameter space of  $F(x)$  allowed for biomass states where  $x_2 = vx_1$ ; this condition spawned the idea that while such a disturbance may certainly affect biomass levels, some fundamental information must remain the same. It was felt that the results demonstrate the utility of the developed process. These estimates presented along with (at times) percentage error or error values justify the estimation properties of the methodology. Figures 1-5 were meant to illustrate the manner in which such a predator-prey system (biomass levels and temporal behavior) will vary given the imperfect knowledge that is ubiquitous in such complex systems. It is reasonable that fundamental characteristics of populations have been well estimated (such as  $s$  and  $v$ ). What is unique and new is that uncertainty as to exact biomass levels is not a limiting factor.

## Acknowledgments

The author wishes to acknowledge Professor Michael Shipley, Department of Biology, Midwestern State University, for his constructive comments and suggestions upon reviewing this manuscript.

## References

- [1] McDonald, D. B. (2013). Locally Precise Response Surface Models for the Generalization of Controlled Dynamic Systems and Associated Performance Measures. *2013 ASME International Mechanical Engineering Congress and Exposition*, 4,(151-160). San Diego, CA, USA.
- [2] McDonald, D. (2014). Sensitivity Characteristics of Response Surface Models for Estimation of Ecological Parameters in Ratio-Dependent Predator-Prey Systems. *American International Journal of Contemporary Research*, 4(6), 1-7.
- [3] McDonald, D., Grantham, W., Tabor, W., & Murphy, M. (2007). Global and Local Optimization Using Radial Basis Function Response Surface Models. *Applied Mathematical Modelling*, 31(10), 2095-2110.
- [4] Das, T., Mukherjee, R., & Chaudhuri, K. (2009). Bioeconomic Harvesting of a Predator-Prey System. *Journal of Biological Dynamics*, 3(5), 447-462.
- [5] McDonald, D. (2012). Instantaneous Optimal Control of a Predator-Prey Natural Resource with a Prey-Dependent Functional Response. *ASME Early Career Technical Journal*, 11, 105-111.
- [6] Kar, T., Pahari, U., & Chaudhuri, K. (2004). Management of a Prey-Predator Fishery Based on Continuous Fishing Effort. *Journal of Biological Systems*, 12(3), 301-313.
- [7] Sun, G., Sarwardi, S., Pal, P., & Rahman, M. (2010). The Spatial Patterns through Diffusion-Driven Instability in Modified Leslie-Gower and Holling-Type II Predator-Prey Model. *Journal of Biological Systems*, 18(3), 593-603.
- [8] Froda, S., & Zahedi, A. (2009). The Spatial Patterns Simple Testing Procedures for the Holling Type II Model. *Theoretical Ecology*, 2, 149-160.

## Biography

**DALE B. MCDONALD** is an associate professor of mechanical engineering within the McCoy School of Engineering at Midwestern State University. He earned his BS, MS, and PhD degrees from Washington State University. Dr. McDonald's interests include the control of ecological systems, the radiographic sciences, optimal sedation, and collaborative art and STEM-inspired ceramics. Dr. McDonald may be reached at [dale.mcdonald@mwsu.edu](mailto:dale.mcdonald@mwsu.edu)

# A HEURISTIC STRATEGY FOR THE CONTROL OF VIBRATION DEVELOPED IN AUTOMATIC BAR FEEDERS FOR TURNING OPERATIONS USING MAGNETORHEOLOGICAL FLUID

Kevin M. Hubbard, Missouri State University; Martin P. Jones, Missouri State University; Richard N. Callahan, Missouri State University

## Abstract

Magnetorheological fluids (MR) are employed in automotive, aerospace, medical, defense, and seismic damping applications. In this paper, the authors present a heuristic method for the control of vibration using MR fluid in bar feeder/turning center operations. Two types of feedback-based, closed-loop control algorithms were evaluated: traditional proportional-integral-derivative (PID) control and a heuristic control algorithm employing experimentally determined optimal magnetic field settings. A series of tests were conducted and data sets were collected at frequencies centered about each predicted natural frequency up to 5000 rpm. The average vibrational amplitude was computed by finding the local maxima and minima for each data set and establishing the optimal amperage level for the electromagnets. The data indicate that the heuristic algorithm exhibits superior performance in terms of reduced vibrational amplitudes when compared with a traditional PID control algorithm.

## Introduction

Magnetorheological (MR) fluid typically consists of a base fluid, micro-sized iron or steel particles, and a surfactant that facilitates the retention of these particles in suspension [1]. MR fluids are employed in automotive, aerospace, medical, optical, military/defense, and seismic damping applications. For example, MR fluid-based vibration dampers are incorporated in the General Motors Corvette active suspension, Boeing F-18 stability augmentation system control actuators, and Maytag washing machine vibration dampers [2]. Bar feeders are employed in industrial turning operations to increase the level of efficiency of the manufacturing process [3]. Bar feeders may be loaded with one or more pieces of bar stock to facilitate turning operations. The use of a bar feeder eliminates the need for an operator to load individual pieces of bar stock or unload the remnants from the turning centers. Using a bar feeder, continuous machining may be achieved. Bar feeders typically handle round, square, or hexagonal bar stock as long as 12 feet,

which is the standard length for U.S. manufacturing or the standard three meters in metric nations.

In industrial turning operations that employ bar feeders, vibration may occur in the bar stock being fed to the operation. This vibration may occur as a result of one or more of three causative factors: bar stock runout, off-axis center of mass due to variations in density along the axis of the bar stock, forced vibration induced by the turning center spindle, or deteriorating process conditions [4]. Traditional damping methods for vibration control include the use of feed tubes that enclose the bar stock (filled with pressurized oil) or guide channels that clamp and support the bar stock at discrete points along the length of the bar. Both of these traditional vibration damping methods are passive rather than active. If a large variety of bar stock sizes is to be employed in the turning operations supported by the bar feeder, a large capital investment must be made in order to possess the correct guide channels.

Detrimental consequences arising from vibrational effects developed in the bar stock include

- Degradation of workpart tolerances and process capability
- Development of chatter
- Degradation of workpart surface roughness and surface integrity
- Reduced cutting tool life
- Reduced productivity
- Reduced machine tool life
- Increased cost of production

The use of MR fluid in bar feeder applications for vibration damping has two advantages. Surrounding the bar stock with MR fluid allows the user to run smaller bar stock in larger guide channels, thereby reducing changeover time and dramatically decreasing the capital investment associated with the purchase of multiple guide channel sets. In this paper, the authors present a heuristic method for the control of vibration using MR fluid in bar feeder/turning center operations. This method is efficient and performs as well as, or is superior to, traditional control methods.



# Magnetorheological Fluid

MR fluids may be employed in either valve mode or direct shear mode. In valve mode, the fluid flows through an orifice. Figure 1 depicts valve mode schematically.

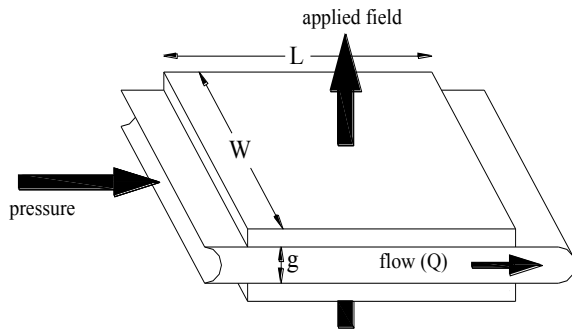


Figure 1. Valve Mode

In direct shear mode, the fluid is placed in dynamic shear between two surfaces. Figure 2 depicts direct shear mode schematically.

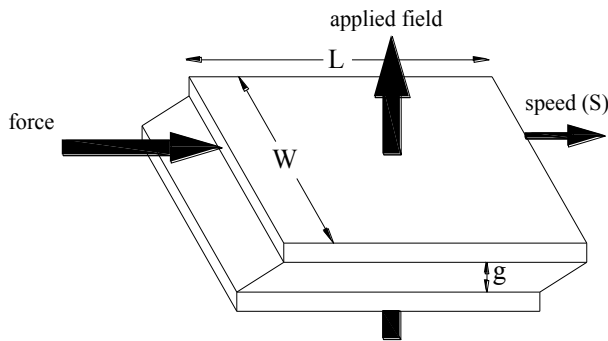


Figure 2. Direct Shear Mode

For the case of the MR fluid not being exposed to a magnetic field, Figure 3 shows that its characteristics are essentially those of the base fluid. When the fluid is exposed to a magnetic field, the micro-sized magnetic particles align with the lines of magnetic flux. Increasing magnetic field strength results in an increasing level of particle alignment [5]. As alignment becomes more pronounced, Figure 4 depicts the interaction between the induced dipoles causing the particles to form columnar structures, which are parallel to the applied magnetic field.

The viscous characteristics of an MR fluid are dependent upon the columnar structures that restrict motion of the fluid [6]. MR fluids exhibit Newtonian-like behavior in the absence of a magnetic field. Typically, an MR fluid under the influence of a magnetic field may be represented as a Bing-

ham plastic having variable yield strength. Equation (1) shows how the flow of an MR fluid exposed to a magnetic field may be characterized using Bingham's equations [7]:

$$\tau = \tau_y(H) + \eta\dot{\gamma}, \tau \geq \tau_y \tag{1}$$

where,

- $\tau$  = Shear stress
- $\tau_y$  = Field dependent yield stress
- $H$  = Magnetic field intensity
- $\eta$  = Plastic viscosity of the fluid
- $\dot{\gamma}$  = Fluid shear strain rate

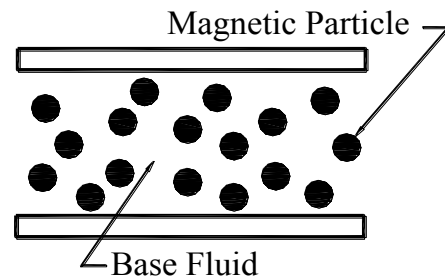


Figure 3. MR Fluid with No Magnetic Field Applied

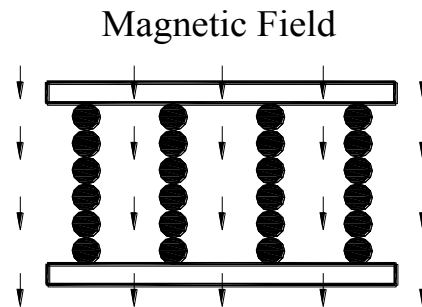


Figure 4. MR Fluid with Magnetic Field Applied

If the stress experienced by the fluid is below yield stress, at strains on the order of  $10^{-3}$  inch/inch, the fluid behaves viscoelastically [8], as in Equation (2):

$$\tau = G\gamma, \tau < \tau_y \tag{2}$$

where,

- $G$  = Complex material modulus
- $\gamma$  = Fluid shear strain

The complex modulus is also field dependent [9]. As particle alignment increases, the fluid's field dependent yield strength and dynamic viscosity increase. In effect, as magnetic field strength increases, the fluid becomes more stiff [8]. In direct shear mode, the fluid resides between two plates or curvilinear surfaces that are in relative motion with respect to one another. As this relative motion occurs, the

MR fluid experiences shear. By varying the magnetic field strength, the field dependent yield strength and dynamic viscosity of the fluid can be varied. As a result, the non-conservative forces present in the system can be varied as well. The response time of an effective MR fluid is typically less than  $10^{-3}$  seconds. For a shear rate of  $26 \text{ s}^{-1}$ , typical fluid shear stresses range from 110 Pa at a flux density of 0.011 T to 18 kPa at a flux density of approximately 10 T [8]. The constant of proportionality,  $m$ , is approximately 1.75 Pascals/Tesla for a given shear rate [8].

## Vibration in Industrial Turning Applications

In an industrial turning operation where a bar feeder is employed, vibration may occur as a result of bar stock runout, off-axis center of mass due to variations of density along the axis of the bar stock, forced vibration induced by the spindle speed, or deteriorating process conditions [4]. Vibration is severe when the bar is subjected to a forcing function at or near one of its natural frequencies. Equation (3) predicts the natural frequencies of a rotating bar with a clamped support at the turning center chuck and a simple support at the bar feeder pusher (subject to a forced vibration) [10]:

$$\omega_r = \frac{\pi^2 \left( r + \frac{1}{4} \right)^2}{L^2} \left[ \frac{EI}{m} \right]^{\frac{1}{2}} \quad (3)$$

where,

- $E$  = Young's modulus of the bar material
- $I$  = Second moment of area of the bar's cross section
- $m$  = Mass per unit length of the bar material
- $L$  = Length of the bar
- $r$  = Mode number (1, 2, 3 . . .)
- $\omega_r$  = Natural frequency (rad/s) for mode number  $r$

If  $E$ ,  $I$ , and  $m$  (the material and diameter of the bar) are held constant and  $L$  varies with time, then the natural frequencies of the bar also vary with time. This is the case in a production situation since, as workparts are parted from the bar stock, the bar advances such that its unsupported length (i.e., the length projecting from the turning center chuck into the bar feeder) changes with time. Since the natural frequencies of the bar stock vary with time, frequent adjustment of the magnetic field applied to the MR fluid-based vibration damping system is necessary, either manually or by an automated control algorithm. It is worthy of note that in this type of vibration damping application, a magnetic field that is too strong may produce results inferior to those arising from the application of a magnetic field that is too weak.

## Control Algorithm Development and Evaluation

In this study, the authors evaluated two types of feedback-based, closed-loop control algorithms: traditional proportional-integral-derivative (PID) control and a heuristic control algorithm employing experimentally determined optimal magnetic field settings as the initial value for a Newton-Raphson style search for the optimum setting under any given set of machining conditions. An FMB Turbo 10-65 hydrostatic style bar feeder was used as the test bed for this research (see Figure 5).



Figure 5. FMB Turbo 10-65 Hydrostatic Bar Feeder

The guide channel of the bar feeder was modified to receive five pairs of electromagnets, placed 18 inches apart on center (see Figure 6). Figure 7 depicts a schematic of the guide channel and electromagnet pairs. A resistor array allowed the current supplied to the electromagnets to vary in 37 discrete increments, resulting in magnetic flux densities ranging from zero to full scale, as shown in the Appendix. A piezoelectric accelerometer sensed the frequency and amplitude of the vibration developed in the bar stock. For control algorithm development, a 12-foot-long, 0.500-inch-diameter 6061-T6 aluminum bar was employed. This alloy possesses a Young's modulus of 68.9 GPa and a density of  $2700 \text{ kg/m}^3$ , which results in a mass per unit length of  $0.342 \text{ kg/m}$ .

Figure 8 depicts the block diagram of the physical system in Figure 6. Here,  $S(s)$  denotes the system set point,  $G_c(s)$  denotes the controller transfer function,  $G(s)$  denotes the physical system transfer function, and  $R(s)$  denotes system response.



Figure 6. Modified Guide Channel and Electromagnets

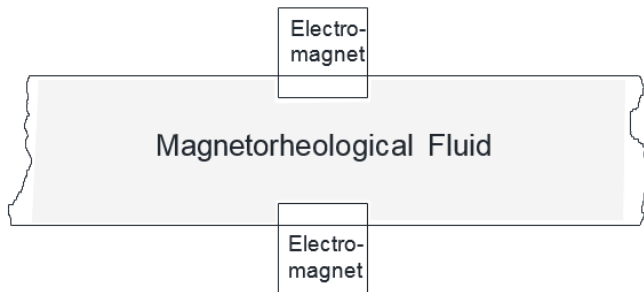


Figure 7. Guide Channel/Electromagnet Schematic

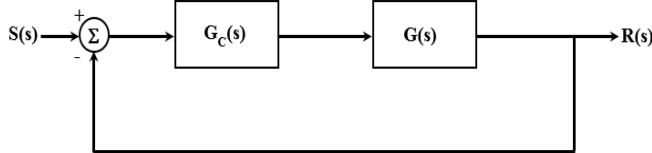


Figure 8. System Block Diagram

Equation (3) was used to predict the natural frequencies of the 6061-T6 aluminum bar stock. Table 1 details calculation results.

Table 1. Predicted Natural Frequencies for Aluminum 6061-T6, 0.5 Inch Diameter Round Bar

Mode #(r)	1	2	3	4	5	6
$\omega_r$ (rad/s)	18.5	59.9	125	214	326	462
$\omega_r$ (rev/min)	177	572	1190	2040	3110	4410

A series of tests were conducted and data sets collected at frequencies centered about each predicted natural frequency up to 5000 rpm. Spindle speed range for each natural frequency was set at 25% above and below the predicted natu-

ral frequencies. The frequency step size of each test was set at five percent of the difference of the upper/lower boundaries, but not to exceed 50 rpm. For example, for the natural frequency predicted at 177 rpm, data were collected at spindle speeds of 140, 150, 160, 170, 180, 190, 200, 210, 220, and 230 rpm to ensure a sufficient number of data sets to establish the actual natural frequencies of the test specimen. Including replications, 147 data sets were collected. Figure 9 illustrates a typical data set.

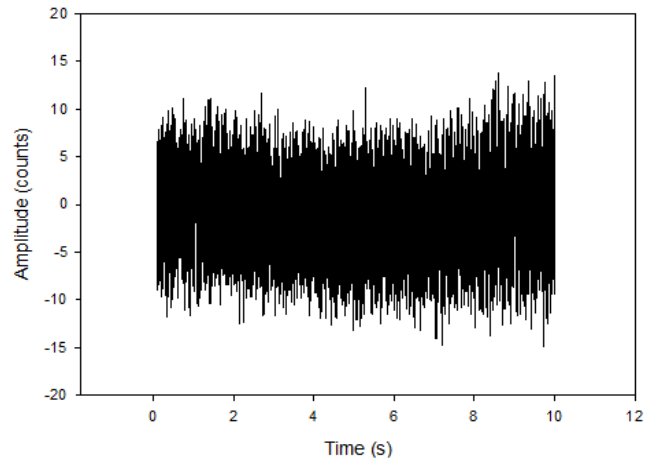


Figure 9. Typical Data Set

Figure 10 depicts a fast fourier transform (FFT) of data collected at a spindle speed of 1260 rpm. The results depicted in this figure approximately match the results delineated in Table 1. The average amplitude was computed by finding the local maxima and minima for each data set. Inflection points were disregarded and only local maxima and minima were evaluated. Figure 11 depicts the local maxima and minima in a representative sub-set of raw data, twelve data points numbered  $i = 1, i = 2, \dots, i = 12$ , and seven local maxima/minima numbered  $j = 1, j = 2, \dots, j = 7$ . Note that in Figure 11 the values are non-integer, due to a noise filtering algorithm to remove ambient electromagnetic noise from the signal. For the data depicted in Figure 11,  $C_{j=1}$  occurs at  $i=2$ ,  $C_{j=2}$  occurs at  $i=4$ ,  $C_{j=3}$  occurs at  $i=6$ , etc. Equation (4) was employed to calculate the amplitude between the local maxima and minima:

$$A_j = |C_{j+1} - C_j| \quad (4)$$

where,

$C_i$  = The value, in counts (bit resolution), of data point number  $i$ , collected at time  $t_i$

$C_j$  = The value, in counts (bit resolution), of local maximum or minimum number  $j$

$A_j$  = "Amplitude", in counts (bit resolution), between  $C_j$  and  $C_{j+1}$

Equation (5) yields the average amplitude, A:

$$A = \frac{\sum_{j=1}^n A_j}{n} \quad (5)$$

where, n is the number of local maxima/minima found.

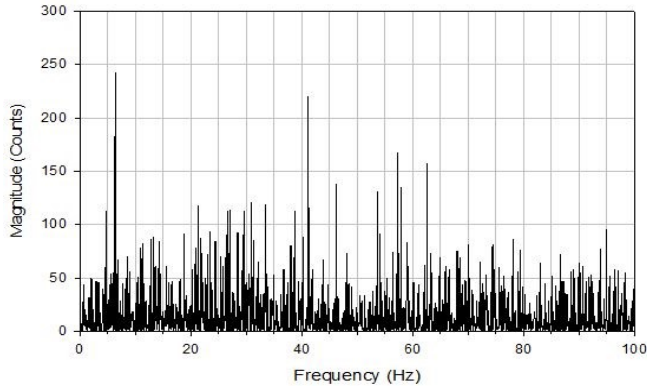


Figure 10. FFT of Data at 1260 rpm Spindle Speed

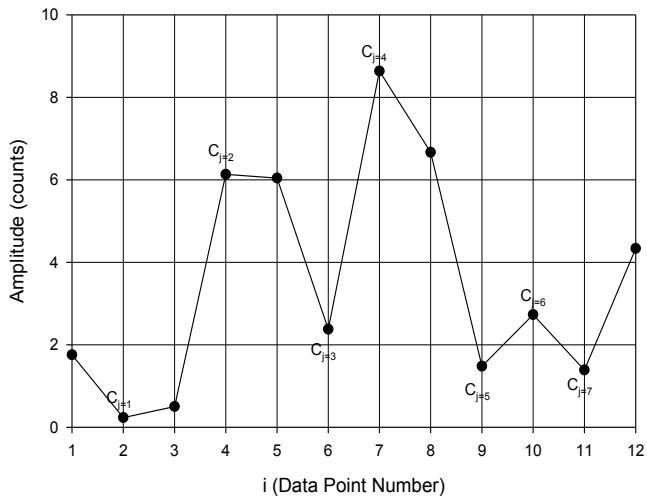


Figure 11. Data Set Representative Local Maxima-Minima

The modified root mean square (RMS) amplitude, R, was employed in all analyses, since it "amplifies" differences in vibrational amplitude between tests conducted under varying conditions, making these differences more easily discernable. In Equation (6), R is expressed in counts:

$$R = \left[ \frac{\sum_{j=1}^n A_j^2}{n} \right]^{\frac{1}{2}} \quad (6)$$

A series of tests were performed, three times each, to establish an optimal amperage level or magnet setting for the electromagnets at spindle speeds ranging from 100 rpm to 5000 rpm at 100 rpm intervals. A look-up table was constructed, consisting of paired spindle speed/magnet setting data. Control software was also developed that used data from this look-up table as the initial value for a Newton-Raphson style search for the optimal setting under any given set of operating conditions. Magnetic flux density was held constant in each test. Magnetic flux density was varied from test to test. The test order (magnetic flux density) was randomized using a random number generator for each test. Figure 12 depicts modified RMS amplitudes versus spindle speeds for three instances of a test run at 24% of full-scale magnetic flux density.

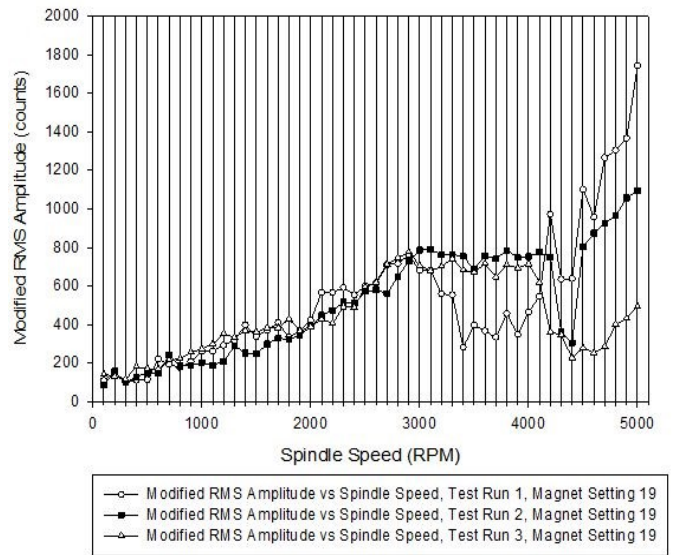


Figure 12. Modified RMS Amplitude versus Spindle Speed, 24% Full-Scale Magnetic Flux Density

A two-sample t-test was performed to compare each of the three test results at each magnetic flux density setting to the others (i.e., test 1 versus test 2, test 2 versus test 3, and test 1 versus test 3). Table 2 shows the results from three tests performed at 3%, 24%, and 95% of full-scale flux density.

Table 2. Two-Sample T-Test Results for Tests 1, 2, and 3

Magnetic Flux Density (percent of full scale)	p value (Test 1 vs. Test 2)	p value (Test 2 vs. Test 3)	p value (Test 1 vs. Test 3)
3	0.815	0.151	0.137
24	0.645	0.001	0.020
95	0.202	0.002	0.037

In most cases, results from the third test differed significantly from those of the first two test instances, as evidenced by p values less than 0.05, perhaps attributable to the in-use temperature change of the MR fluid. The rise in temperature has an effect on the viscosity of the base fluid, ultimately affecting the performance of the MR fluid. In subsequent versions of the MR fluid-based vibration damping system, the fluid will continuously recirculate, thereby, maintaining a constant fluid temperature. Averaging the results of each set of three tests established a single value to quantify each set. Figure 13 shows the magnetic flux density setting resulting in the minimum modified average RMS amplitude that was determined for each spindle speed.

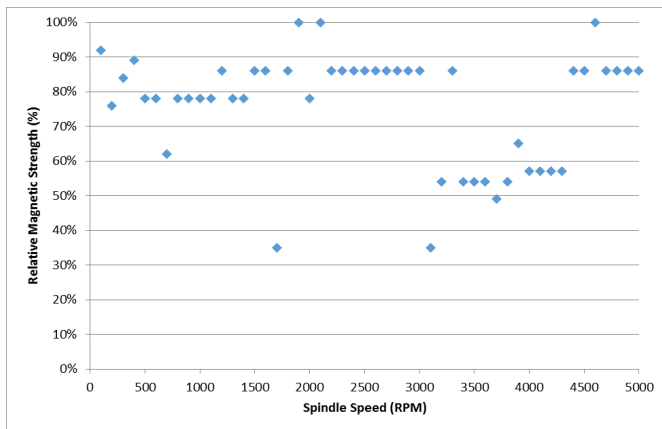


**Figure 13. Spindle Speeds and Corresponding Optimum Magnetic Flux Density**

Control software was developed that employed a Newton-Raphson style search algorithm starting at the value contained in the look-up table. Since the look-up table is employed as an initial magnetic flux density value, the Newton-Raphson technique is nearly assured to converge on the optimal magnet setting [11]. Beginning with the initial value of magnetic flux density from the look-up table, the software varies the magnet setting by a step size defined by the user. Smaller step sizes result in longer times to convergence and more accurate final values, while larger step sizes result in shorter convergence times but less accurate final values. With each new magnet setting, vibration amplitude data are collected and the modified RMS amplitude is calculated in near real time.

If the new modified RMS amplitude is less than the previous modified RMS amplitude by an amount greater than or equal to the user-defined threshold, then the new magnet setting is more effective than the previous magnet setting. This magnet setting variation is bi-directional. In other words, if the look-up table specifies a magnet setting of 73% of full scale for some spindle speed, and the user defines a step size of 8% of full scale, then new magnet set-

tings of 65% and 81% of full scale are evaluated. A series of user-defined iterations evaluate optimal magnet setting. The software allows the user flexibility in choosing the tradeoff between speed of convergence and accuracy of the final magnetic flux density setting. If the difference in modified RMS amplitude values from iteration to iteration is less than the threshold value, then the new current magnet setting is optimal.

A traditional proportional-integral (PI) control algorithm was also implemented and tuned using direct synthesis [12]. Since different working conditions, which arise normally in situations with bar feeders, result in different optimal values of the control algorithm constants [13], the control software included a self-tuning routine that embodied the traditional PI control algorithm. Testing indicated that the integral term of the control algorithm was, at best, superfluous. As a result, a proportional control algorithm (P-only) was implemented, while the self-tuning routine was retained in the control software. A series of tests were conducted at the frequencies surrounding those delineated in Table 1 to determine which control approach (heuristic control algorithm versus P-only control algorithm) proved to be most effective in each case. The control algorithm that proved to be most effective in terms of smaller modified RMS amplitude values was the heuristic control algorithm. Figures 14 and 15 depict representative results arising from the use of each control algorithm. Note that 402 counts (see Figure 14) corresponds to an acceleration of  $1.201 \text{ m/s}^2$ , while 422 counts (see Figure 15) corresponds to an acceleration of  $1.262 \text{ m/s}^2$ .

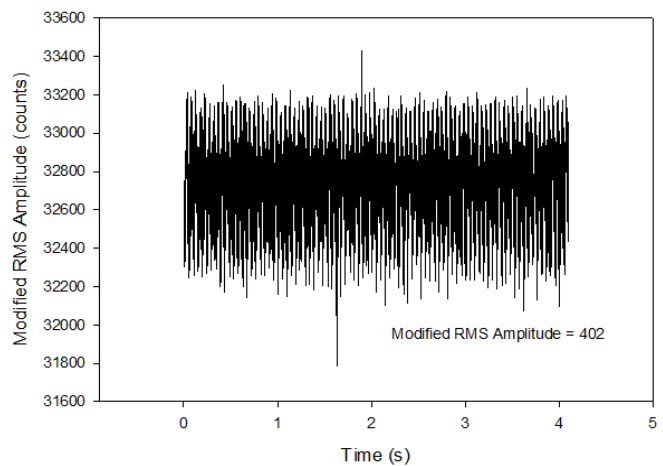


**Figure 14. Heuristic Control Algorithm Results, 1260 RPM**

The P-only control algorithm responded much more quickly than the heuristic algorithm. The heuristic control algorithm responded as much as three times more slowly, based on results collected from three iterations per test at each of the previously delineated spindle speeds. There is a



trade-off in the selection of control algorithm: smaller modified RMS amplitude or a faster response time. Typically, in a constant spindle speed industrial turning situation, extremely small response times are not required. When this is the case, the use of the heuristic control algorithm is indicated.

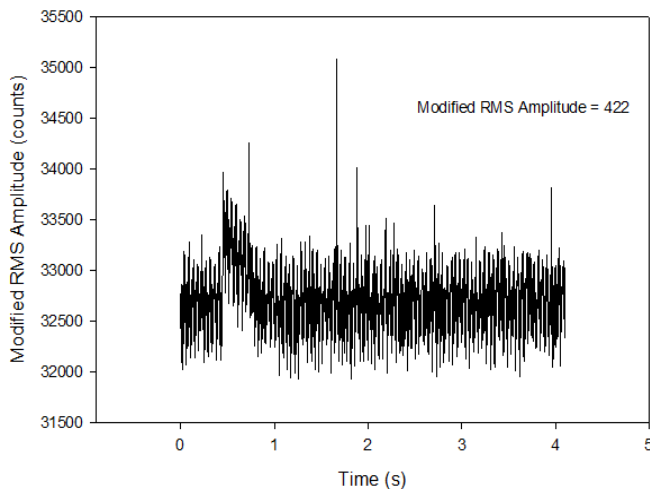


Figure 15. P-Only Control Algorithm Results, 1260 RPM

## Conclusion

In this paper, the authors present the development of a heuristic control algorithm employing experimentally determined magnetic flux density settings as the initial values for a Newton-Raphson style search method. This heuristic algorithm exhibits superior performance in terms of reduced vibrational amplitudes when compared with a traditional proportional-only (P-only) control algorithm. This was exhibited by nearly a five percent reduction of the modified RMS amplitude when the heuristic algorithm was applied compared to the P-only algorithm. The traditional P-only control algorithm exhibited a more rapid response (by up to three times) than the heuristic method. As a result, the P-only algorithm proved to be more efficient than the heuristic algorithm. However, in typical turning applications at constant spindle speeds, this fast response is typically not required. In cases where extremely fast responses are not necessary, the use of the heuristic method is indicated.

Further research is warranted with respect to the effects of bar stock diameter, bar stock length, and bar stock material: testing the various length/diameter/material combinations and testing the effects of each algorithm on the vibrational performance of the system should be investigated. It is possible that, under some combinations, the heuristic algorithm would have a much higher reduction of RMS amplitude than the traditional P-only algorithm. In addition, the effects

of in-use MR fluid heating should be evaluated or, alternatively, the fluid should be maintained at a near-constant temperature. To this end, the study of the effect of lowering the fluid's working temperature might yield more superior performance of the heuristic algorithm compared to that of the P-only algorithm.

## References

- [1] Kciuk, M., & Turczyn, R. (2006). Properties and Applications of Magnetorheological Fluids. *Journal of Achievements in Materials and Manufacturing Engineering*, 18(1-2), 127-130.
- [2] Carlson, J. D. (2005). MR Fluids and Devices in the Real World. *International Journal of Modern Physics B*, 19(7-9), 1463-1470.
- [3] Koepfler, C. (2006). Bar Feeder Considerations for High-Speed, Lights-Out Machining. Retrieved from <http://www.productionmachining.com/articles/bar-feed-considerations-for-high-speed-lights-out-machining>
- [4] Lee, S. S., (2010). Tool Condition Monitoring System in Turning Operation Utilizing Wavelet Signal Processing and Multi-Learning ANNs Algorithm Methodology. *International Journal of Engineering Research and Innovation*, 2(1), 49-55.
- [5] Wang, D. H., & Liao, W. H. (2011). Magnetorheological Fluid Dampers: A Review of Parametric Modelling. *Smart Materials and Structures*, 20(2), 1-34.
- [6] Klingenberg, D. J. (2001). Magnetorheology: Applications and Challenges. *American Institute of Chemical Engineers Journal*, 47(2), 246-249.
- [7] Cho, M. S., Choi, H. J., & Jhon, M. S. (2005). Shear stress analysis of a semiconducting polymer based electrorheological fluid system. *Polymer*, 46(25), 11484-11488.
- [8] Jolly, M. R., J. W. Bender, & J. D. Carlson. (1999). Properties and Applications of Commercial Magnetorheological Fluids. *Journal of Intelligent Material Systems and Structures*, 10(1), 5-13.
- [9] Yanyo, L. C. (2004). Magnetorheological (MR) Fluid for Automotive Damping Systems. *Proceedings IIR Suspension and Damping Conference*, Germany.
- [10] Rao, S. S. (2007). *Vibration of Continuous Systems*. Hoboken, NJ: John Wiley & Sons, Inc.
- [11] Genta, G. (2005). *Dynamics of Rotating Systems*. New York, NY: Springer Science+Business Media, Inc.
- [12] Erickson K. T., & Hedrick, J. L. (1999). *Plant-Wide Process Control* (Vol. 4). Hoboken, NJ: John Wiley & Sons, Inc.
- [13] Tzouanas, C., & Tzouanas, V. (2014). Optimal Tun-

ing of PI Controllers Subject to Process Constraints: Experimental Evaluation. *International Journal of Modern Engineering*, 14(2), 15-20.

## Biographies

**KEVIN M. HUBBARD** is an assistant professor of technology and construction management at Missouri State University. He earned his BS degree (Aerospace Engineering, 1991) from University of Missouri–Rolla, MS (Engineering Management, 1993) from University of Missouri–Rolla, and PhD from University of Missouri–Rolla (Engineering Management, 1996). Dr. Hubbard is currently teaching at Missouri State University. His interests are in automation and device control, manufacturing systems, device design, and process optimization. Dr. Hubbard may be reached at [KHubbard@MissouriState.edu](mailto:KHubbard@MissouriState.edu)

**MARTIN P. JONES** is an associate professor of technology and construction management at Missouri State University. He earned his BS degree (Physics, 1981) from University of Maryland Baltimore County, MS (Materials Science & Engineering, 1984) from the Johns Hopkins University, and PhD (Materials Science & Engineering, 1987) from the Johns Hopkins University. Dr. Jones is currently teaching at Missouri State University. His interests are in scanner technology, nondestructive evaluation, manufacturing processes, and quality assurance. Dr. Jones may be reached at [MartinJones@MissouriState.edu](mailto:MartinJones@MissouriState.edu)

**RICHARD N. CALLAHAN** is department head and a professor of technology and construction management at Missouri State University. He earned his BS degree (Engineering Management, 1988) from University of Missouri - Rolla, MS (Engineering Management, 1992) from University of Missouri - Rolla, and PhD (Engineering Management, 1999) from University of Missouri - Rolla. Dr. Callahan is currently teaching at Missouri State University. His interests are in project management, process optimization, and manufacturing systems. Dr. Callahan may be reached at [NealCallahan@MissouriState.edu](mailto:NealCallahan@MissouriState.edu)

## Appendix

Future researchers may want to duplicate the tests described within this article. To facilitate this, Table 3 lists the magnetic flux densities employed.

**Table 3. Magnetic Flux Densities**

Amps	B <sub>M</sub> (T)	Increment
0.075	0.041400	3.75%
0.137	0.075624	6.85%
0.191	0.105432	9.55%
0.244	0.134688	12.20%
0.333	0.183816	16.65%
0.371	0.204792	18.55%
0.402	0.221904	20.10%
0.469	0.258388	23.45%
0.527	0.290904	26.35%
0.578	0.319056	28.90%
0.619	0.341688	30.95%
0.659	0.363768	32.95%
0.712	0.393024	35.60%
0.755	0.416760	37.75%
0.794	0.438288	39.70%
0.840	0.463680	42.00%
0.883	0.487416	44.15%
0.922	0.508944	46.10%
0.962	0.531024	48.10%
1.000	0.552000	50.00%
1.035	0.571320	51.75%
1.071	0.591192	53.55%
1.105	0.609960	55.25%
1.140	0.628000	57.00%
1.174	0.648048	58.70%
1.203	0.664056	60.15%
1.237	0.682824	61.85%
1.268	0.699936	63.40%
1.299	0.717048	64.95%
1.328	0.733056	66.40%
1.375	0.759000	68.75%
1.467	0.809784	73.35%
1.571	0.867192	78.55%
1.673	0.923496	83.65%
1.811	0.999672	90.55%
1.975	1.090200	98.75%
2.000	1.104	100%

# INSTRUCTIONS FOR AUTHORS: MANUSCRIPT SUBMISSION REQUIREMENTS


The INTERNATIONAL JOURNAL OF MODERN ENGINEERING is an online/print publication. Articles appearing in IJME are centered around engineering-related research. All submissions to this journal, including manuscripts, peer-reviews of submitted documents, requests for editing changes, as well as notification of acceptance or rejection, will be handled electronically.

All manuscript submissions must be prepared in Microsoft Word (.doc or .docx) and contain all figures, images and/or pictures embedded where you want them and appropriately captioned. It is highly recommended that you print, in color, all images in your manuscript in order to determine their quality; the journal editors will be doing the same during the editorial review of your manuscript. If your manuscript is accepted for publication, you will receive instructions regarding all required revisions and the submission of higher-quality images. If you are able to provide such images, it's possible that you will be asked to remove them from the manuscript.

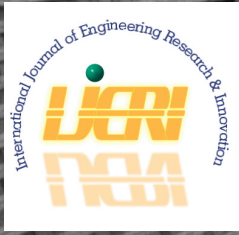
Tables must be created directly in Word, not imported as pictures, and be enclosed on all sides. If you have graphs or charts, they should also be created directly in Word, if possible. If that is not possible, the editor will discuss further options with you. Please be conscientious of the quality of your images and remember that all online and print copies of issues of IJME are in color.

The editorial staff of the International Journal of Modern Engineering reserves the right to format and edit any submitted document in order to meet publication standards of the journal. Included here is a summary of the formatting instructions. You should, however, review the "[sample Word document](#)" included on our website ([http://ijme.us/formatting\\_guidelines](http://ijme.us/formatting_guidelines)) for a detailed analysis of how to correctly format your manuscript.

The references included in the References section of your manuscript must follow APA-formatting guidelines. In order to help you, the sample Word document also includes numerous examples of how to format a variety of sources. If you have a reference source for which you are not able to find the correct APA format, contact me for help anytime ([philipw@bgsu.edu](mailto:philipw@bgsu.edu)). Keep in mind that an incorrectly formatted manuscript will be returned to you, a delay that may cause it to be moved to a subsequent issue of the journal.

1. Word document page setup: Top = 1", Bottom = 1", Left = 1.25", Right = 1.25". This is the default setting for Microsoft Word.
2. Page breaks, tabs, and indents: Do not use page breaks or tabs. Do not use spaces for paragraph indents; use the scroll markers, as shown here. 
3. Paper title: Centered at the top of the first page with a 22-point Times New Roman (Bold), Small-Caps font.
4. Body fonts: Use 10-point Times New Roman (TNR) for body text throughout (1/8" paragraph indentation); 9-point TNR for author names/affiliations under the paper title; 16-point TNR for major section titles; 14-point TNR for minor section titles; 9-point TNR BOLD for caption titles; other font sizes may be noted in the sample Word document.
5. Images: All images should be included in the body of the document. It's ok for images or tables to be centered on the page, and not confined to the 2-column format, if necessary. Irrespective of how Word moves any given image/table, be certain that all captions are located in the document where the images/tables should ultimately be placed. If you are required to submit additional high-quality images, they must be saved/sent as individual files (one image per file) and labeled using the following format, where the first portion of the title is your manuscript number:  
**M15-F-10 Figure 4**
6. In-text referencing: List and number each reference when referring to them in the body of the document (e.g., [1]). In-text references must be in numerical order and follow entries in the References section. Again, see the sample Word document on our website for specifics. Please do not use the End-Page Reference utility in Microsoft Word.
7. Tables and figures: Captions for tables must be above the table, while captions for figures are below; all captions are left-justified unless the table or figure is centered on the page, in which case the caption should also be centered.
8. Page limit: Manuscripts should not be more than 15 pages (single-spaced, 2-column format).
9. Page numbering: Do not use page numbers.





[www.ijeri.org](http://www.ijeri.org)

Print ISSN: 2152-4157  
Online ISSN: 2152-4165



[www.iajc.org](http://www.iajc.org)

# INTERNATIONAL JOURNAL OF ENGINEERING RESEARCH AND INNOVATION

## **ABOUT IJERI:**

- IJERI is the second official journal of the International Association of Journals and Conferences (IAJC).
- IJERI is a high-quality, independent journal steered by a distinguished board of directors and supported by an international review board representing many well-known universities, colleges, and corporations in the U.S. and abroad.
- IJERI has an impact factor of **1.58**, placing it among an elite group of most-cited engineering journals worldwide.

## **OTHER IAJC JOURNALS:**

- The International Journal of Modern Engineering (IJME)  
For more information visit [www.ijme.us](http://www.ijme.us)
- The Technology Interface International Journal (TIIJ)  
For more information visit [www.tiij.org](http://www.tiij.org)

## **IJERI SUBMISSIONS:**

- Manuscripts should be sent electronically to the manuscript editor, Dr. Philip Weinsier, at [philipw@bgsu.edu](mailto:philipw@bgsu.edu).

For submission guidelines visit  
[www.ijeri.org/submissions](http://www.ijeri.org/submissions)

## **TO JOIN THE REVIEW BOARD:**

- Contact the chair of the International Review Board, Dr. Philip Weinsier, at [philipw@bgsu.edu](mailto:philipw@bgsu.edu).

For more information visit  
[www.ijeri.org/editorial](http://www.ijeri.org/editorial)

## **INDEXING ORGANIZATIONS:**

- IJERI is currently indexed by 16 agencies. For a complete listing, please visit us at [www.ijeri.org](http://www.ijeri.org).

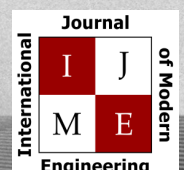
## **Contact us:**

**Mark Rajai, Ph.D.**

Editor-in-Chief  
California State University-Northridge  
College of Engineering and Computer Science  
Room: JD 4510  
Northridge, CA 91330  
Office: (818) 677-5003  
Email: [mrajai@csun.edu](mailto:mrajai@csun.edu)



[www.tiij.org](http://www.tiij.org)



[www.ijme.us](http://www.ijme.us)

# THE LEADING JOURNAL OF ENGINEERING, APPLIED SCIENCE AND TECHNOLOGY

**The latest impact factor (IF) calculation (Google Scholar method) for IJME of 3.0 moves  
it even higher in its march towards the top 10 engineering journals.**

**IJME IS THE OFFICAL AND FLAGSHIP JOURNAL OF THE  
INTERNATIONAL ASSOCIATION OF JOURNALS AND CONFERENCE (IAJC)**

[www.iajc.org](http://www.iajc.org)



The International Journal of Modern Engineering (IJME) is a highly-selective, peer-reviewed journal covering topics that appeal to a broad readership of various branches of engineering and related technologies. IJME is steered by the IAJC distinguished board of directors and is supported by an international review board consisting of prominent individuals representing many well-known universities, colleges, and corporations in the United States and abroad.

## **IJME Contact Information**

**General questions or inquiries about sponsorship of the journal should be directed to:**

**Mark Rajai, Ph.D.**

**Editor-in-Chief**

**Office: (818) 677-5003**

**Email: [editor@ijme.us](mailto:editor@ijme.us)**

**Department of Manufacturing Systems Engineering & Management**

**California State University-Northridge**

**1811 Nordhoff St.**

**Northridge, CA 91330**